

Final Technical Report

to

The Strategic Environmental Research and Development Program

Waste Forms Based on Separations Media (DOE 360-94)

Principal Investigators:

Dr. M. Lou Balmer and Dr. Bruce Bunker
Pacific Northwest National Laboratory
Battelle Blvd. MSIN K2-44
P.O. Box 999
Richland, WA 99352

and

Dr. Delbert E. Day
Ceramic Engineering Department and
Graduate Center for Materials Research
University of Missouri-Rolla
Rolla, MO 65401

30 January, 1997

DISTRIBUTION STATEMENT A
Approved for Public Release
Distribution Unlimited

REPORT DOCUMENTATION PAGE

Form Approved
OMB No. 074-0188

Public reporting burden for this collection of information is estimated to average 1 hour per response, including the time for reviewing instructions, searching existing data sources, gathering and maintaining the data needed, and completing and reviewing this collection of information. Send comments regarding this burden estimate or any other aspect of this collection of information, including suggestions for reducing this burden to Washington Headquarters Services, Directorate for Information Operations and Reports, 1215 Jefferson Davis Highway, Suite 1204, Arlington, VA 22202-4302, and to the Office of Management and Budget, Paperwork Reduction Project (0704-0188), Washington, DC 20503			
1. AGENCY USE ONLY (Leave blank)	2. REPORT DATE	3. REPORT TYPE AND DATES COVERED	
January 30, 1997 Final Technical Report			
4. TITLE AND SUBTITLE Final Technical Report to The Strategic Environmental Research and Development Program, Waste Forms Based on Separations Media (DOE 360-94)		5. FUNDING NUMBERS N/A	
6. AUTHOR(S) M. Lou Balmer, Bruce Bunker, Delbert E. Day, Principal Investigators			
7. PERFORMING ORGANIZATION NAME(S) AND ADDRESS(ES) Pacific Northwest National Laboratory Battelle Blvd. MSIN K2-44 P.O. Box 999 Richland, WA 99352		8. PERFORMING ORGANIZATION REPORT NUMBER N/A Ceramic Engineering Department and Graduate Center for Materials Research University of Missouri-Rolla Rolla, MO 65401	
9. SPONSORING / MONITORING AGENCY NAME(S) AND ADDRESS(ES) SERDP 901 North Stuart St. Suite 303 Arlington, VA 22203		10. SPONSORING / MONITORING AGENCY REPORT NUMBER N/A	
11. SUPPLEMENTARY NOTES The United States Government has a royalty-free license throughout the world in all copyrightable material contained herein. All other rights are reserved by the copyright owner.			
12a. DISTRIBUTION / AVAILABILITY STATEMENT Approved for public release: distribution is unlimited.		12b. DISTRIBUTION CODE A	
13. ABSTRACT (Maximum 200 Words)			
14. SUBJECT TERMS SERDP; SERDP Collection			15. NUMBER OF PAGES 194
			16. PRICE CODE N/A
17. SECURITY CLASSIFICATION OF REPORT unclass.	18. SECURITY CLASSIFICATION OF THIS PAGE unclass.	19. SECURITY CLASSIFICATION OF ABSTRACT unclass.	20. LIMITATION OF ABSTRACT UL

NSN 7540-01-280-5500

Standard Form 298 (Rev. 2-89)
Prescribed by ANSI Std. Z39-18
298-102

DTIC QUALITY INSPECTED 4

19990521 132

TABLE OF CONTENTS

Summary	I
Chapter 1: EVALUATION OF CESIUM SILICOTITANATES AS AN ALTERNATIVE WASTE FORM	1
Section 1a. The Structure and Properties of Two New Silicotitanate Zeolites	9
Section 1b. Neutron and X-Ray Diffraction Study of the Crystal Structure of $CsTiSi_2O_{6.5}$	16
Section 1c. The Crystal Structure of $CsTiSi_6O_{15}$	34
Section 1d. Experimental and Calculated X-Ray Powder Diffraction Data for Cesium Titanium Silicate $CsTiSi_2O_{6.5}$: A New Zeolite	81
Chapter 2: IMMOBILIZATION OF HIGH-LEVEL RADIOACTIVE SLUDGES IN IRON PHOSPHATE GLASS	102

Summary

Waste Forms Based on Separations Media (DOE 360-94)

Millions of gallons of radioactive wastes contained in tanks at U.S. Department of Energy's (DOE's) Hanford site require immobilization in stable waste forms. Unfortunately, many waste feeds produced during tank waste processing are either insoluble or incompatible with the baseline borosilicate glass host that is currently proposed for containment of Hanford waste. Two feeds that represent significant challenges to borosilicate glass are phosphate-rich tank sludges and silicotitanate ion exchangers (< 1 wt% of each insoluble component is allowed in the baseline glass). If high levels of waste dilution are required to stabilize these wastes, the resulting volume of high level borosilicate waste glass can be up to 100 times greater than that of the waste feed, thus increasing disposal costs by tens of billions of dollars.

Researchers at PNNL examined the feasibility of alternative glass or ceramic waste forms for containment of TiO_2 -rich and phosphate-rich wastes. Tailoring of waste form compositions to specific waste feeds rather than attempting to tailor waste feeds for accommodation by a single waste form will minimize the volume of expensive HLW. For TiO_2 -rich ion exchanger waste, the high temperature phase selection and properties for three key constituents of silicotitanate ion exchangers: Cs_2O , SiO_2 , and TiO_2 was determined. This work has mapped out large portions of the phase diagram (Figure 1) and has shown that several glass and ceramic compositions have durabilities comparable to borosilicate glass. While TiO_2 may have limited solubility in borosilicate glass, silicate glasses that do not contain boron can incorporate up to 30 wt% TiO_2 . Two new Cs -silicotitanate zeolites with unique crystal structures that encapsulate the Cs in covalently bonded molecular cages have been discovered. Both these zeolites, as well as several other glass and ceramic compositions examined in the Cs_2O - TiO_2 - SiO_2 , system have high durabilities and would serve as viable waste forms for containment of Cs sorbed onto silicotitanate ion exchangers.

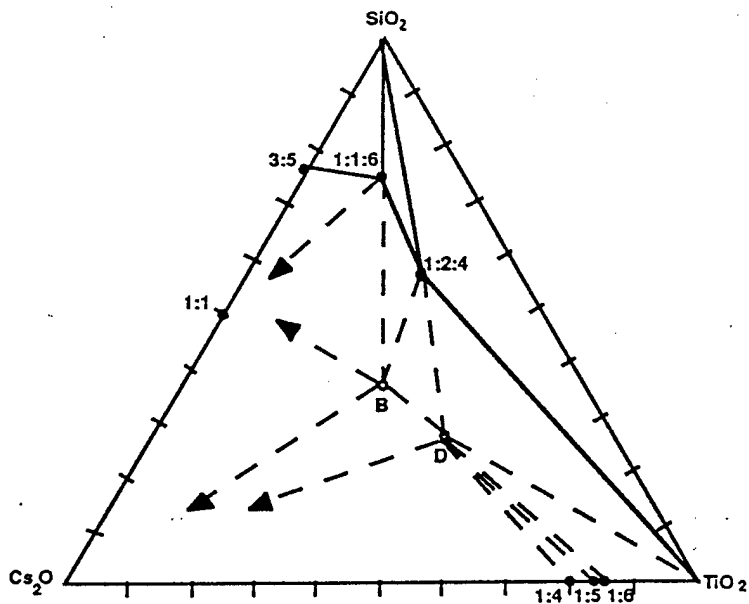


Figure 1: Ternary phase diagram for the system Cs_2O - TiO_2 - SiO_2 . Two new phases, $CsTiSi_2O_{6.5}$ and $Cs_2TiSi_6O_{15}$ were discovered and characterized. Two or more additional phases with approximate composition (B and D) have been identified.

Iron phosphate glass has been identified as an alternative host for phosphate and iron-rich tank waste and for CsCl and SrF₂ capsule waste. These glasses contain up to 50 times more phosphate and four times more iron than borosilicate glass. The glasses can incorporate high concentrations (20-40 wt%) of alkali metal ions such as Na⁺ and still retain durabilities (resistance to attack by water) that are comparable to or better than that of standard borosilicate waste glass. The glasses are formed using prevalent sludge components, thus minimizing frit additions and waste volumes. Iron phosphate glasses have also been shown to dissolve 30 wt% CsCl or SrF₂ while maintaining exceptional durabilities (20 to 50 times better than borosilicate glass). The potential for iron phosphate glasses to provide exceptional chemical durability at substantially higher waste loadings makes these new glasses attractive candidates as hosts for disposal of phosphate-rich sludges.

Chapter 1

**EVALUATION OF CESIUM SILICOTITANATES
AS AN ALTERNATIVE WASTE FORM**

EVALUATION OF CESIUM SILICOTITANATES AS AN ALTERNATIVE WASTE FORM

YALI SU, M. LOU BALMER, and BRUCE C. BUNKER
Pacific Northwest National Laboratory, Richland, WA 99352

ABSTRACT

Silicotitanate ion exchangers are potential materials for the removal of radioactive Cs and Sr from tank wastes. In this paper the viability of direct thermal conversion of Cs-loaded silicotitanates to an acceptable high level waste form has been examined. Results show that in aqueous solutions, the Cs leach rates of crystalline silicotitanates (heat treated at 800 °C) are 0.04, 0.18, 0.4 g/m²day for Cs loadings of 1, 5, and 20 wt%, respectively. Heating the Cs-loaded (up to 20 wt %) silicotitanates at or above 900 °C for 1 hour further reduces the Cs leach rates to approximately zero (beyond the 1 ppm detection limits). Moreover, Cs volatilization was found to be ≤ 0.8 wt% at temperatures as high as 1000 °C. These results suggest that thermally converted silicotitanate ion exchangers exhibit excellent chemical durability (comparable to or better than borosilicate glass) and thus, have great potential as an alternative waste form.

INTRODUCTION

Over the past 50 years, nuclear defense activities have produced over 100 million gallons of nuclear wastes that now require safe and permanent disposal¹. The current proposed disposal procedure is to remove Cs and Sr from the concentrated salt solutions with selective ion exchangers, then treat the solution as low-level waste (LLW). After separation from the salt solutions, the concentrated Cs and Sr are planned to be vitrified, then interim-stored or placed into long-term, geological storage as high level waste (HLW). To implement these procedures, one of the most important steps is to identify the ion exchange material. An acceptable ion exchanger not only must have high selectivity, and chemical, thermal and radiation stabilities, but also must be acceptable to the actual exchange processes, and be able to be converted into a stable waste form for disposal². For the past few years, a number of organic and inorganic ion exchange materials, including resorcinol-formaldehyde resin, aluminosilicate zeolites, zirconium phosphates, and crystalline silicotitanates (CSTs), have been developed and evaluated for the removal of Cs and Sr from the nuclear wastes²⁻⁵. Recently, studies show that CSTs fulfill many of these requirements² and thus, have the potential as ion exchangers for the removal of Cs from nuclear wastes.

The feasibility of converting CSTs into a HLW form is being evaluated. Currently, two options are being considered for processing the Cs-loaded exchangers: 1) elution and concentration, 2) dissolution in borosilicate waste glass melts. Since Cs is retained in CSTs even in acidic solution, this precludes the elution option. Thus, processing the Cs-loaded CSTs requires the direct use of the loaded exchanger as a feed to make the final waste form. In general, this is accomplished by "melt-dissolution" where the loaded exchanger is first mixed with glass frit and/or other radwaste oxides, then dissolved into borosilicate melts to form the HLW glass. For CSTs, this "melt-dissolution" process has been challenged because in current glass

formulations the maximum allowed TiO_2 concentration is only 1 wt%. Assuming ideal column operation can be achieved with the CST, dissolution of the CST into borosilicate glass would increase the total volume of HLW glass to 33% more than the baseline⁶. Researchers at PNNL have identified direct thermal conversion as another option for CST conversion to solid waste³. Different from the previous two options, this method directly converts the CSTs into solid waste forms by heating the Cs-loaded CSTs at high temperature with a minimum amount of other additives.

In this paper, we examine the feasibility of direct thermal conversion to produce an alternative waste form. A CST formulation, TAM-5 (synthesized by UOP, initially developed at Sandia and Texas A&M University), has been studied in terms of its Cs volatility during heat treatment and chemical durability after heat treatment. The results show that the thermally converted Cs-loaded silicotitanate ion exchangers have good potential to be an alternative waste form.

EXPERIMENTAL METHODS

TAM-5 ion exchangers were used as received. Four different Cs loadings, 1, 5, 10 and 20 wt% were examined. The Cs loadings (1 to 10 wt%) were accomplished by adding TAM-5 powder to a CsCl solution with the exact Cs concentration, then stirring the solution for 24 hours. Solutions were analyzed by atomic absorption spectrometry (AAS) to assure that all Cs was ion exchanged from solution. The 20 wt% Cs loading was prepared by first adding TAM-5 to a CsCl solution in which the Cs concentration was ten times higher than the Cs exchange capacity. The maximum Cs loading was determined to be 20 wt% by measuring the final Cs concentration in solutions. Cs loaded samples were rinsed with de-ionized water, centrifuged and dried in air. Thermogravimetric analysis (TGA) and differential thermal analysis (DTA) were performed at a rate of 10°C/min on the Cs-loaded samples to determine the temperatures at which decomposition, crystallization, and melting occurred. Heat treatments were performed in air at temperatures ranging from 500 to 1000°C at a rate of 5°C/min. The heat treated samples were analyzed for the volume fraction and structure of crystalline phases using x-ray diffraction (XRD).

The Cs leach rate was measured using the MCC-1 standard static leach test.⁷ The Cs-loaded powders were heat treated to 500 °C for one hour then pressed into a pellet. The resulting pellet was further heated at the test temperature for one hour. For the leach test, the heat treated pellet was suspended by a Teflon string in the 90 °C de-ionized water. The leachate solution was analyzed for Cs concentration using (AAS). The geometric surface area of the pellets was used for calculation of the leach rates. Cs volatility measurements were performed in two steps. The Cs-loaded pellet was first heat treated in an enclosed Pt crucible in the hot zone of a furnace. The top of the crucible was extended out from the hot zone and was cooled by convection to allow the volatile components to condense on the inside of the crucible. The volatile components were then collected by washing the crucible in a 0.2 M nitric acid solution. The amount of Cs in the volatile components in the nitric acid solution was determined by AAS.

RESULTS AND DISCUSSION

I. Cs Leach Rate

The leach rates of several Cs loaded TAM-5 samples heat treated at several different temperatures were measured at different time. The results are shown in Figure 1. After heating at 700°C for 1 hour and then leaving the pellet in the deionized water for 24 hours, the 1, 5 and

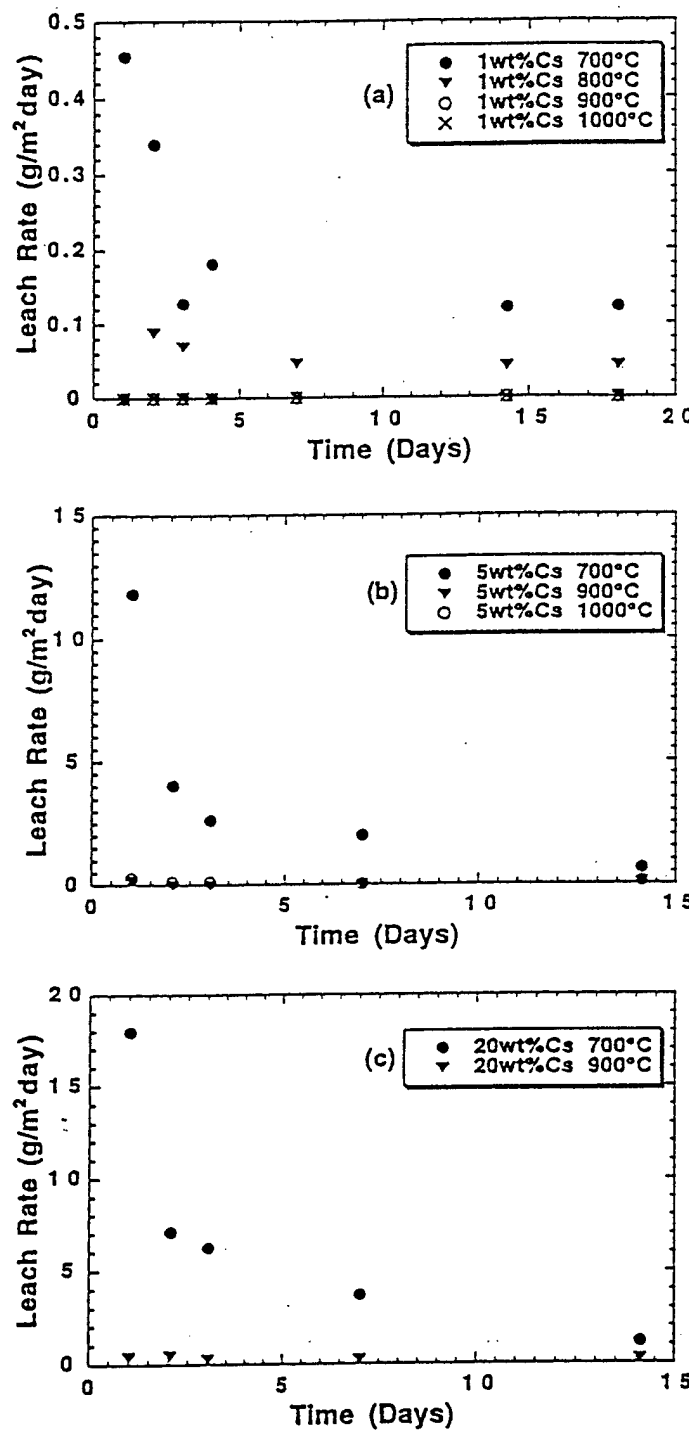


Figure 1. Leach rates measured at 90°C for (a) 1 wt%, (b) 5 wt%, and (c) 20 wt% Cs loaded TAM-5 samples treated at different temperatures.

20wt% Cs loaded samples exhibited high Cs leach rates of 0.45, 12, and 18 g/m²day, respectively. Since the Cs leach rate decays monotonically with time as shown in Fig.1, after 14 days the leach rates reduced from previous values to 0.12, 0.62, and 1.1 g/m²day, respectively. In contrast to these high leach rates, the Cs loaded samples exhibited very low leach rates after heating at higher temperatures. For example, after heating at 800°C for one hour the leach rates of 1, 5, and 20wt% Cs loaded samples became 0.04, 0.18, 0.4 g/m²day, respectively. Thus, increase of the treatment temperature from 700 °C to 800 °C reduces the leach rate by more than an order of magnitude. Increase of temperature to 900°C or higher further reduces the leach rates to approximately zero (beyond the AAS detection limits). These results show that durability highly depends on both the Cs loading and the thermal history. The phase(s) which is (are) responsible for locking in Cs will be discussed in following sections.

II. TGA/DTA results

In addition to the Cs leach rates, melting, crystallization, and weight loss were studied using TGA/DTA to evaluate the phases responsible for the low Cs leach rates. Results showed that samples with different Cs loadings (1 to 10wt%) exhibited similar TGA/DTA patterns, suggesting that different Cs loading did not alter the phase distribution. Figure 2 shows typical

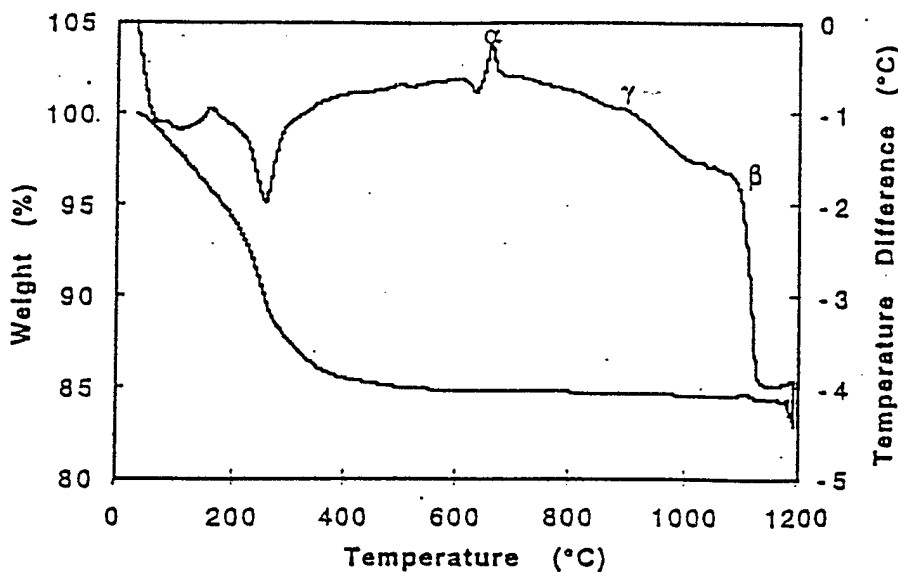


Figure 2. TGA/DTA results at a heating rate of 10°C/min for 1wt% Cs loaded TAM-5 sample.

TGA/DTA curves of a TAM-5 sample loaded with 1 wt% of Cs. In the DTA curve, an exothermic or endothermic peak without a corresponding weight loss corresponds to the change or formation of a crystalline phase or to a melting event. The exothermic events at 650°C and 850°C (labeled α and γ respectively on Figure 2) represent the formation of a crystalline phase while the endothermic event at 1100 °C labeled β is where melting occurred. Around 250°C, the TGA curve exhibits the highest weight loss rate, suggesting decomposition occurred in that temperature region. The formation of a new crystalline phase at 850°C (labeled γ) corresponds

to the significant change in Cs leach rates between 700°C and 900°C. The 20wt% Cs loaded sample exhibits a somewhat different TGA/DTA pattern. In addition to the shifts of endothermic and exothermic peaks in the low temperature region, melting occurs at 1000°C, suggesting that the 20wt% Cs loaded sample has a different phase composition, as will be further discussed in the next section.

III. Phase Evaluation

Cs-Loaded TAM-5 samples have five components, Cs_2O , Na_2O , SiO_2 , TiO_2 , and a proprietary component. The phase composition of the heat-treated, Cs-loaded TAM-5 samples was analyzed using XRD. Volume percentage of the total crystalline phases was calculated by comparing the total diffracted intensity with the integrated background. Weight percentage of each crystalline phase was determined by the ratio of the 100% peak height to the total diffracted intensity. The crystalline phase, volume fraction and weight percentage of different phases of the heat treated Cs-TAM-5 samples are summarized in Table I.

The phases labeled A-F are new, unknown single phases or mixtures of phases that could not be matched with any existing compounds in the Powder Diffraction File (PDF) database. The phases labeled X and Y are known sodium and sodium titanium-containing phases that also contain a proprietary component. Although phase identification is incomplete, relationships between the phase evolution with temperature and the corresponding leach rates can be identified. As was shown in Section I, the Cs leach rate decreases by more than an order of magnitude between 700 and 900 °C. This temperature range corresponds to the disappearance of phase B and the formation of Phase C, (proprietary phase X remains approximately constant). From this result, it appears that phase C is responsible for binding the Cs and reducing the leach rate. For 20 wt% Cs loadings, additional phase E which does not appear to affect the leach rate, is observed from 700 –900°C. The composition-temperature-phase relationships for the $\text{Cs}_2\text{O}-\text{TiO}_2-\text{SiO}_2$ are currently under investigation and are expected to provide some insights into the phase selection and high durability of heat treated Cs-TAM-5.

IV. Cs Volatility

The Cs weight loss (volatility) of the Cs-TAM-5 was examined at different processing temperatures. Since volatility generally increases with loading, here we only discuss the volatility at the maximum Cs loading (20 wt%) condition. The Cs weight loss as a function of temperature is shown in Figure 3. The results suggest that the Cs losses are extremely low, only 0.6 to 0.8 wt% of the total Cs loading at the expected processing temperatures (800 to 1000 °C). This is comparable to Cs volatility from borosilicate glass for Cs loadings of 1.9 wt% at 900°C, which is well below the melting temperature of borosilicate glass⁸. Cs losses of borosilicate glass can be as high as 70 wt%⁹ at the typical processing temperature (1150°C).

V. Comparison of Leach Rates of Cs-TAM-5 with Borosilicate Glass

In order to show that Cs-TAM-5 has the potential to be an alternative waste form, it is important to compare the Cs leach rate of Cs-TAM-5 with those of the current baseline waste form-borosilicate glass. However, a direct comparison is difficult since Cs loadings in

Table I Phase Composition of Cs-exchanged TAM-5

Cs loading (wt%)	Heat Temperature (°C, 1 hour)	Crystal Vol. Fraction(%)	Weight percentage of Crystalline Phase
1	500	100	Phase A
1	700	100	70% X, 30% Phase B
1	800	100	70% X, 15% Phase B+C, Minor Y
1	900	80	75% X, 10% Phase C, 15% Y
1	1000	70	60% X, 35% Phase C+D, Minor Y
5	500	100	Phase A
5	700	100	70% X, 30% Phase B
5	800	100	70% X, 15% Phase B+C, Minor Y
5	900	80	75% X, 10% Phase C, 15% Y
5	1000	60	70% X, 15% Phase C+D, Minor Y, 5% Rutile
10	500	100	Phase A
10	700	100	70% X, 30% Phase B
10	800	100	70% X, 30% Phase B+C
10	900	55	75% X, 10% Phase C, 15% Y
10	1000	55	55% X, 10% Phase C+D, 35% Rutile
20	500	55	30% X, 70% Phase A
20	700	50	25% X, 75% Phase B+E
20	800	60	45% X, 55% Phase B+C+E
20	900	65	30% X, 55% Phase C+E, 15% Y
20	1000	45	55% X, 20% Phase F, 5% Y, 20% Rutile

Note: Phase A, B, C, D, E, and F are unidentified phases. X and Y are proprietary phases, X and Y phases contain no Cs.

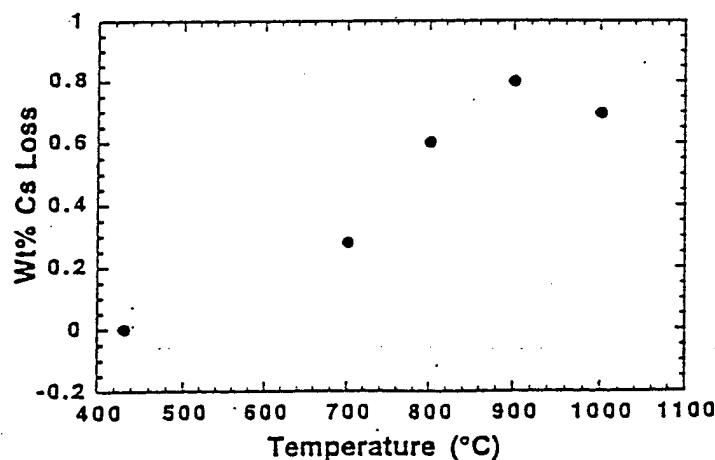


Figure 3. Weight percentage of Cs loss of a Cs-TAM-5 sample (20wt% Cs loading) as a function of treatment temperature.

borosilicate glass are typically much lower than those in Cs-loaded silicotitanates. But if we nonetheless compare the leach rates of borosilicate with those of Cs-TAM-5, we find that the leach rate of borosilicate glass is several times higher than those of the Cs-TAM-5. For example, the Cs leach rates of borosilicate glass simulant (R7T7, Cs₂O content of 1.42 wt% and an overall alkali content of 13.26 wt%) was 0.91 g/m²day after 1 day of leaching⁹. Under the similar Cs loading, the leach rate of the TAM-5 sample, however, is approximately zero (beyond the 1ppm AAS detection limits) after treated at 900 °C. If borosilicate was loaded with 20 wt% of Cs, the durability of the glasses would be greatly diminished. Furthermore, Rana and Douglas obtained a leach rate of 8 g/m²day (85 °C) for a silicate glass loaded with 15 mol% potassium¹⁰. Based on their results, a silicate glass with 20 wt% of Cs (11 mol%) would have a leach rate approximately 6 g/m² day, more than two orders of magnitude higher than that of the Cs-TAM-5 treated at 900 °C.

CONCLUSIONS

This study shows that "direct thermal conversion" is a viable processing method to transform Cs loaded silicotitanate ion exchangers into a durable final waste form. Cs-TAM-5 exhibits extremely low Cs leach rates after heat treatment from 800°C to 900°C. The heat treatment is a simple, one step process at temperatures well below the current optimal melting temperature for borosilicate glass. At the optimal processing temperature, the Cs volatility of Cs-TAM-5 is orders of magnitude lower than that of borosilicate glass at its processing temperature (1150°C). The "direct thermal conversion" method concentrates ion exchanger waste resulting in much lower waste volumes than the dissolution-into-borosilicate-melts method. These advantages suggest that direct thermal conversion of Cs-loaded silicotitanate ion exchangers represents a potential alternative to the dissolution of CSTs in borosilicate glass.

ACKNOWLEDGMENTS

The authors would like to thank Mr. D. McCready for performing XRD measurements. Support for this work was provided by the Strategic Environmental Research and Development Program (SERDP). Pacific Northwest National Laboratory is operated for the U. S. Department of Energy by Battelle Memorial Institute.

REFERENCES

1. D. F. Bickford, A. Applewhite-Ramsey, C. M. Jantzen, and K. G. Brown, *J. Am. Cer. Soc.* 73, pp. 2896-2902, 1990.
2. B. C. Bunker, "Evaluation of Inorganic Ion Exchangers for Removal of Cs from Tank Wastes", TWRSP-94-085, Pacific Northwest National Laboratory, Richalnd, WA, September, 1994.
3. M. L. Balmer, and B. C. Bunker, "Inorganic Ion Exchange Evaluation and Design-Silicotitanate Ion Exchange Waste Conversion", PNL-10460 UC-2070 Pacific Northwest National Laboratory, Richland, WA 99352 , March, 1995.
4. R. G. Dosch, N. E. Brown, H.P. Stephens, and R. G. Anthony, *Waste Management* 93, February 28-March 3, Tucson, Arizona, pp. 1751-1754.

5. E.A. Klavetter, N. E. Brown, D. E. Trudell, R. G. Anthony, D. Gu, and C. Thibaud-Erkey, Waste Management 94, February 28-March 3, Tucson, Arizona, pp. 709-719.
6. WHC Internal Memo, R. A. Kirkbride to D. J. Washenfelder, "Evaluation of the Impact of the Use of Crystalline Silicotitanate Ion Exchanger on High-level Waste Glass Production," 9457566, March, 1995.
7. D. M. Strachan, R. P. Turcotte, and B. O. Barnes, Nuclear Technology, 56, pp. 306-312, 1982.
8. W. J. Gray, Radioactive Waste Management, 12, pp. 147-169, 1980.
9. J. L. Nogues, E. Y. Vernaz, N. Jacquet-Francillon in The Scientific Bases for Nuclear Waste Management, Vol. 44 edited by C. M. Jantzen, J. A. Stone, and R. C. Ewing, (Materials Research Society, 1984).
10. M. A. Rana, and R. W. Douglas, Phys. and Chem. of Glasses, 2, pp. 179-195, 1961.

Section 1a

The Structure and Properties of Two New Silicotitanate Zeolites

THE STRUCTURE AND PROPERTIES OF TWO NEW SILICOTITANATE ZEOLITES

M.L. BALMER*, Y. SU*, I.E. GREY**, A. SANTORO***, R.S. ROTH***, Q. HUANG****,
N. HESS* AND B.C. BUNKER*

* Materials and Chemical Sciences Department, Pacific Northwest National Laboratory,
Richland, WA 99352 **CSIRO Division of Minerals, Melbourne, Australia *** Reactor
Division, National Institute of Standards and Technology, Gaithersburg, MD 20899

****University of Maryland, College Park, MD 20742

ABSTRACT

Two new zeolitic crystalline phases with stoichiometry, $CsTiSi_2O_{6.5}$ and $Cs_2TiSi_6O_{15}$, have been discovered. $CsTiSi_2O_{6.5}$ has a crystal structure isomorphous to the mineral pollucite, $CsAlSi_2O_6$, with Ti^{+4} replacing Al^{+3} . This replacement requires a mechanism for charge compensation. A combination of techniques including neutron diffraction, single crystal x-ray diffraction and x-ray absorption spectroscopy have revealed that eight extra oxygens are present per unit cell $CsTiSi_2O_{6.5}$ as compared to pollucite. As a result of the extra oxygen, the titanium coordination geometry is five-fold. Pentacoordinate titanium and tetrahedral silicon form a network structure with Cs residing in cages formed by the network. The crystal structure of $Cs_2TiSi_6O_{15}$ is unique, with titanium octahedra and silicon tetrahedra forming an open framework structure with the Cs residing in large cavities. The largest covalently bonded ring opening to the Cs cavities in both compounds are smaller than a Cs ion, revealing that the Cs ion has minimal mobility in the structure. Cesium leach rates for both compounds are lower than or comparable to borosilicate glass.

INTRODUCTION

Plans are in place to remove, process and permanently dispose of over 100 million gallons of nuclear waste that is temporarily stored in underground tanks at the Department of Energy's Hanford site. The baseline process includes separation of the solid and liquid components, removal of radioactive species such as Cs and Sr from the liquid waste, and disposal of the resulting high level waste by dissolution in a borosilicate melt to form high level waste (HLW) glass. A promising ion exchanger for separation of Cs and Sr from tank wastes is the crystalline silicotitanate (CST) developed at Sandia, Texas A&M and UOP.¹ However, TiO_2 present in CSTs is only scarcely soluble in borosilicate glass. Analysis of the process flow with the CST has shown that the total amount of HLW glass produced would increase by 33% as a result of CST dilution. If these high levels of dilution are required to stabilize these wastes, the resulting volume of high level borosilicate waste glass can increase disposal costs by billions of dollars. A significant reduction in waste form volume can be realized if loaded exchangers are thermally converted to a glass or ceramic waste form rather than diluted in borosilicate glass. Cs-loaded silicotitanate ion exchangers contain the basic ingredients needed to form a ceramic or glass at high temperature.

Researchers at PNNL are examining the feasibility of using alternative glass or ceramic waste forms with compositions similar to the starting loaded ion exchanger for containment of TiO_2 -rich wastes. It was found that several new, unidentified phases precipitate from Cs-loaded

heat treated CSTs.² Identification and characterization of all these phases is critical so that thermodynamics and geological evidence can be used to assess long term stability and compatibility with repository conditions. The loaded exchanger represents a complicated chemical mixture containing at least five components, Cs_2O , Na_2O , TiO_2 , SiO_2 , and a proprietary component. Although the phase selection in the $\text{Na}_2\text{O}-\text{TiO}_2-\text{SiO}_2$ system has been characterized, the $\text{Cs}_2\text{O}-\text{TiO}_2-\text{SiO}_2$ phase diagram and the more complicated four and five component systems have not been investigated. Work to date at PNNL has concentrated on identifying the high temperature phase selection and properties for three key constituents of silicotitanate ion exchange waste; Cs_2O , SiO_2 , and TiO_2 . As a result of $\text{Cs}_2\text{O}-\text{TiO}_2-\text{SiO}_2$ phase diagram work, two new compounds with zeolitic structures have been identified. The crystal structures, chemical durability and potential of these two new phases for long-term Cs containment are discussed.

EXPERIMENT

Powder samples of $\text{CsTiSi}_2\text{O}_{6.5}$ were prepared using a sol gel synthesis route. Tetra-isopropyl orthotitanate (TIOT) and tetraethyl orthosilicate (TEOS) were mixed in inert conditions then CsOH , water and ethanol were added dropwise. The hydrolyzed precursor was mixed for a minimum of 15 hours, then dried in air at room temperature. The amorphous, homogeneous precursor was heat treated in air at 800°C for at least one hour to form crystalline $\text{CsTiSi}_2\text{O}_{6.5}$. Crystalline $\text{Cs}_2\text{TiSi}_6\text{O}_{15}$ powder was made by melting sol gel precursor powders or mixtures of Cs_2CO_3 , TiO_2 and SiO_2 at 1200°C, quenching to room temperature, mixing with 40 wt% CsVO_3 flux, then heat treating to 790°C for a minimum of 50 hours. Several cycles of grinding and heat treatment were necessary to form a nominally phase pure compound. Residual, unreacted CsVO_3 flux was removed by washing three times in warm water at 90°C for 10 minutes followed by centrifuging to separate solids from the liquid. Despite long heat treatment times and several heating and grinding cycles, the final $\text{Cs}_2\text{TiSi}_6\text{O}_{15}$ powder contained approximately 10 wt% of unidentified crystalline impurity compounds.

Single crystals of $\text{CsTiSi}_2\text{O}_{6.5}$ and $\text{Cs}_2\text{TiSi}_6\text{O}_{15}$ were grown from a powdered sample of $\text{CsTiSi}_2\text{O}_{6.5}$ and CsVO_3 flux. The mixture of $\text{CsTiSi}_2\text{O}_{6.5}$ and CsVO_3 was placed in a Pt tube, sealed at both ends, then heat treated in a vertical tube furnace at the rate of 50°C/hr to 1100°C, held for one hour, then cooled to 650°C at a rate of 1°C/hr. After dissolving the CsVO_3 flux in warm water, a mixture of crystals including $\text{CsTiSi}_2\text{O}_{6.5}$, $\text{Cs}_2\text{TiSi}_6\text{O}_{15}$, rutile and cristobalite were retrieved.

The Cs leach rate was measured using the MCC-1 and the product consistency test method B (PCT) standard leach tests. For MCC-1, heat treated pellets were suspended on a teflon string in de-ionized water contained in a teflon container for the leach test. After the desired time at a constant temperature, a sample of the solution with a known volume was analyzed for the Cs content using atomic absorption spectrometry (AAS). For the PCT test, powder samples were placed in a teflon container in de-ionized water at 90°C for the desired period of time. The leachate solution was analyzed for Cs concentration using AAS.

X-ray single crystal and powder diffraction experiments were performed to elucidate the crystal structure of $\text{CsTiSi}_2\text{O}_{6.5}$ and $\text{Cs}_2\text{TiSi}_6\text{O}_{15}$. Additionally, neutron diffraction experiments were performed on $\text{CsTiSi}_2\text{O}_{6.5}$ in order to determine the location of oxygen positions in excess

of those predicted by the pollucite crystal structure. Details of the data collection and refinement procedures for neutron powder, single crystal, and powder diffraction are published elsewhere.^{3,4}

RESULTS AND DISCUSSION

Structure of $\text{CsTiSi}_2\text{O}_{6.5}$

Powder x-ray diffraction studies show that $\text{CsTiSi}_2\text{O}_{6.5}$ is a derivative of the cesium aluminosilicate pollucite, $\text{CsAlSi}_2\text{O}_6$, with titanium replacing aluminum. The compound crystallizes with the symmetry of space group $\text{Ia}3\text{d}$ and a lattice parameter $a=13.8425$.^{3,4} Titanium and silicon are disordered on the 48g sites of the cubic space group similar to Si and Al in pollucite. The substitution of Ti^{+4} for Al^{+3} in pollucite requires a mechanism for charge compensation, such as the presence of tri-valent titanium cations, or the incorporation of oxygen in excess of six atoms per formula unit. The presence of Ti^{+3} (resulting in stoichiometry $\text{CsTiSi}_2\text{O}_6$) is unlikely since the compound is synthesized in air at 800°C , and Ti^{+3} usually only occurs under highly reducing conditions. It is also worth noting that the samples have a white color, typical of Ti^{4+} compounds. In addition, x-ray photoelectron spectroscopy and Ti x-ray absorption near edge structure (XANES) studies on $\text{CsTiSi}_2\text{O}_{6.5}$ show that Ti is primarily in the Ti^{+4} valence state.^{4,5} Evidence of the incorporation of excess oxygen as a charge compensation mechanism could be seen by Ti XANES and Raman spectroscopy which show that Ti is in five fold coordination environment.⁵

Because x-ray diffraction is relatively insensitive to small changes in oxygen composition, neutron diffraction measurements were made using the high resolution powder diffractometer at the National Institute of Standards and Technology reactor to confirm the presence of excess oxygen and to determine their positions. These experiments revealed the presence of eight additional oxygens per unit cell of silicotitanate pollucite ($Z=16$).⁴ The "extra" oxygens are distributed randomly over two partially occupied general sites designated O(2) and O(3). On average the O(2) site is occupied by 0.06 atoms and the O(3) site is occupied by 0.023 atoms. As a consequence of the presence of "extra" oxygen, the average coordination of the central Cs cation becomes thirteen-fold, rather than twelve-fold as in $\text{CsAlSi}_2\text{O}_6$ pollucite. In addition, when one of the 'extra' sites is occupied by an oxygen, the coordination of the neighboring tetrahedral cations becomes five-fold. In the case where an excess oxygen coordinates a tetrahedral site, it is assumed that the neighboring tetrahedra are occupied by titanium, rather than silicon, based on ionic radii considerations and on experimental XANES results that show $\text{Ti}(5)$. Although no ordering on Ti on the 48g site could be detected by single crystal x-ray or neutron diffraction, it is suspected based on stoichiometry (Ti:excess oxygen is 2:1) and on the fact that no $\text{Ti}(4)$ could be conclusively identified by XANES or Raman spectroscopy, that randomly distributed pairs of Ti ions share the excess oxygens. The crystal structure of $\text{CsTiSi}_2\text{O}_{6.5}$ viewed along [111] is shown in Figure 1a, and Figure 1b shows one of the excess O(2) oxygen positions and bond distances with respect to neighboring Ti/Si and Cs. The network structure consists of interconnected rings containing four and six polyhedra. The Cs resides in cages that are bound by two six-rings and that form channels along the non-intersecting three-fold symmetry axis and are joined together in the $\langle 110 \rangle$ directions.

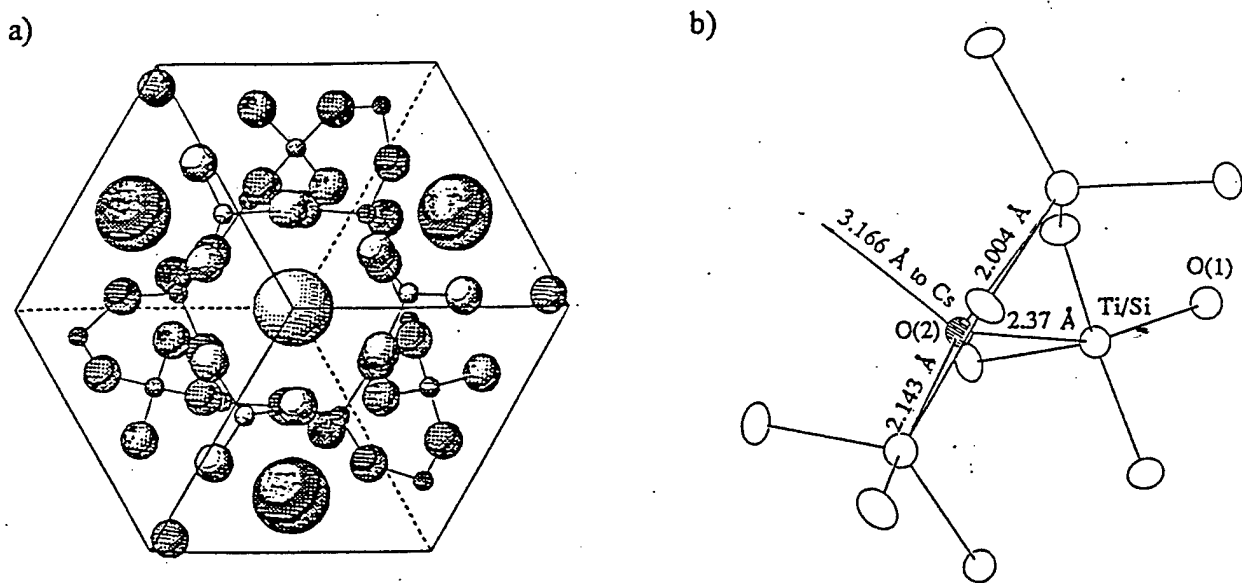


Figure 1. a.) View down the $\langle 111 \rangle$ of the Cs cages in $\text{CsTiSi}_2\text{O}_{6.5}$. Cs cages are formed by rings of four and six Si/Ti polyhedra and Cs ions are coordinated by 13 oxygen ions. b.) Local view of the coordination environment around a tetrahedral site with an O(2) site filled.

Structure of $\text{Cs}_2\text{TiSi}_6\text{O}_{15}$

The compound $\text{Cs}_2\text{TiSi}_6\text{O}_{15}$ has a new crystal structure, unrelated to any known compounds. $\text{Cs}_2\text{TiSi}_6\text{O}_{15}$ crystallizes with monoclinic symmetry and space group $\text{C}2/\text{c}$, with $a = 13.386 \text{ \AA}$, $b = 7.423 \text{ \AA}$, $c = 15.134 \text{ \AA}$, $\beta = 107.71^\circ$ and $Z=4$.⁶ The structure consists of corner shared titanium octahedra and silica tetrahedra that form an open framework. The titanium octahedra are isolated by silica tetrahedra resulting in a local bonding configuration that consists of only of Ti-O-Si and Si-O-Si type bonds. Similar to pollucite, the Cs ions reside in large cages formed by the tetrahedral and octahedral linkages. The topology of the cage around the Cs can be described by interconnecting rings of polyhedra consisting of one three ring, three five-rings, two six-rings and two eight-rings.⁶ A view down the b axis that clearly shows the five and six rings is shown in Figure 2a. It can also be seen in Figure 2a that titanium octahedra are isolated by Si_2O_7 groups and that the Cs ions form rows along the $[101]$. Figure 2b shows a view of the Cs ions looking down the $[101]$. The cavities that contain the Cs ions have large apertures normal to the $[101]$ formed by two different type of ellipsoidal 8-rings. In the first type of 8-ring there are two titanium octahedra and six silica tetrahedra and in the second type of 8-ring there are six silica tetrahedra. The average coordination of the central Cs ion is ten.

Chemical Durability

Among the important criteria that a nuclear waste form must satisfy to be suitable for long-term storage are low solubility and low Cs leach rate. The crystal structures of both silicotitanate pollucite and $\text{Cs}_2\text{TiSi}_6\text{O}_{15}$ indicate that the Cs ion will have low mobility in the structure which in turn should result in a low Cs leach rate. The Cs ion in silicotitanate pollucite is in cages where the maximum opening to the cage is defined by a 6-ring. Assuming 2.7 \AA as the diameter of the oxygens lining the inner peripheries of the 6-ring, the maximum opening size of this ring (in an ideal planar configuration) is 2.7 \AA , which is considerably smaller than a Cs ion (diameter of at least 3.5 \AA). Early investigations of the aluminosilicate pollucite isomorph of

a) b)

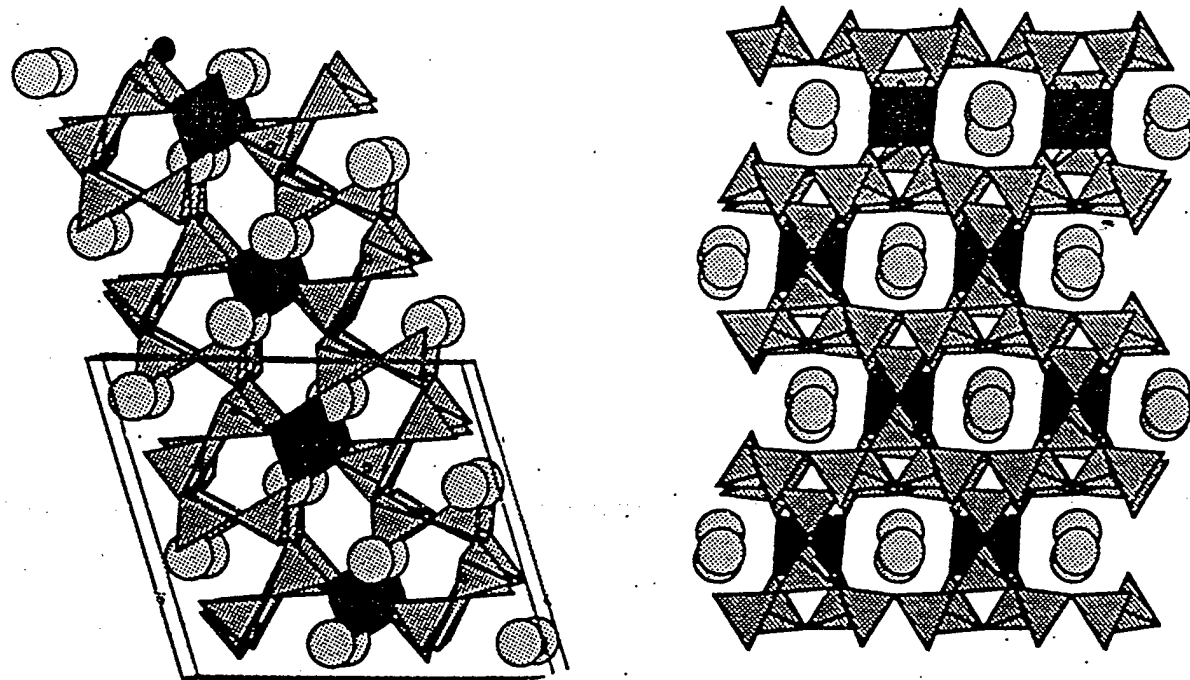


Figure 2. a.) View of the $\text{Cs}_2\text{TiSi}_6\text{O}_{15}$ structure down the b axis showing the 5- and 6-rings of silicon tetrahedra and titanium octahedra. b.) View of $\text{Cs}_2\text{TiSi}_6\text{O}_{15}$ down the $\langle 101 \rangle$ showing ellipsoidal rings of eight polyhedra.

$\text{CsTiSi}_2\text{O}_{6.5}$ show that it has high Cs leach resistance, exhibiting aqueous leach rates from $5.7 \times 10^{-4} \text{ g m}^{-2} \text{ d}^{-1}$ to $3 \text{ g m}^{-2} \text{ d}^{-1}$.⁷⁻⁹ While incorporation of excess oxygen into $\text{CsTiSi}_2\text{O}_{6.5}$ as compared to $\text{CsAlSi}_2\text{O}_6$ influences local bonding configurations, the long range crystal structure and predicted Cs mobility remain largely unchanged.

The largest apertures in the Cs cavity in $\text{Cs}_2\text{TiSi}_6\text{O}_{15}$ are two eight rings formed by eight silica tetrahedra (8T) or by two Ti-octahedra and six tetrahedra (2O + 6T). Based on an oxygen diameter of 2.7 \AA the opening size of the elliptical 8T ring is $1.8 \times 4.2 \text{ \AA}$ and that of the elliptical 2O + 6T ring is $2.5 \times 4.8 \text{ \AA}$.⁶ Therefore, the Cs ions can not move freely along the channels, and the compound is expected to have a relatively low Cs leach rate.

Cs leach rate experiments on silicotitanate pollucite and $\text{Cs}_2\text{TiSi}_6\text{O}_{15}$ support crystal structure predictions of low Cs leachability. The equivalent 14 day leach rates normalized to the surface area are $1.8 \text{ g m}^{-2} \text{ d}^{-1}$ for $\text{CsTiSi}_2\text{O}_{6.5}$ (MCC-1) and $1.47 \times 10^{-5} \text{ g m}^{-2} \text{ d}^{-1}$ for $\text{Cs}_2\text{TiSi}_6\text{O}_{15}$ (PCT) Table 1. The leach rates for silicotitanate pollucite are comparable to hot pressed $\text{CsAlSi}_2\text{O}_6$ ($3 \text{ g m}^{-2} \text{ d}^{-1}$ at 100°C) where a Soxhlet type apparatus and geometric surface area were used to measure leach rate.⁹ Values of the normalized leach rate of $\text{CsTiSi}_2\text{O}_{6.5}$ may be unrealistically high because the geometric surface area used in the MCC-1 static leach test did not reflect the true surface area of the sample. The sample pellet of silicotitanate pollucite was only 60% of theoretical density so that a large amount of surface area in the form of open porosity was not accounted for. The surface area of the powder $\text{Cs}_2\text{TiSi}_6\text{O}_{15}$ used for the PCT test was

measured using a He expansion ratio, a much more accurate measurement. The fractional Cs release, $F_R\%$, which reflects the portion of the total Cs released from the sample without normalizing to the surface area is similar for both materials (Table I). It is worth noting that the MCC-1 leach test typically yields conservative durabilities because solution concentrations of elements are comparatively low and leaching continues during the entire leach period. On the other hand, PCT tests typically have high solution concentrations of leached elements which can act to reduce dissolution rates and yield higher durabilities. In the case of $Cs_2TiSi_6O_{15}$ the Cs concentration in the PCT solution was extremely low. PCT and MCC-1 tests are planned on $CsTiSi_2O_{6.5}$ and $Cs_2TiSi_6O_{15}$ respectively so that a direct comparison of the durabilities can be made.

Table I: Cumulative Cs leach rates and fractional Cs release for $CsTiSi_2O_{6.5}$ and $Cs_2TiSi_6O_{15}$.

Time (days)	$CsTiSi_2O_{6.5}$ MCC-1		$Cs_2TiSi_6O_{15}$ PCT	
	Leach Rate ($g\ m^{-2}\ d^{-1}$)	$Cs\ F_R\%$	Leach Rate ($g\ m^{-2}\ d^{-1}$)	$Cs\ F_R\%$
1	4.0	0.41	8.4×10^{-4}	0.91
2	2.73	0.69	2.3×10^{-4}	1.17
3	2.3	0.93	1.1×10^{-4}	1.29
4	-	-	6.8×10^{-5}	1.36
6	1.83	1.5	-	-
7	-	-	3.84×10^{-5}	1.49
9	1.69	2.0	-	-
10	1.66	2.17	-	-
13	1.49	2.57	-	-
14	-	-	1.47×10^{-5}	1.6

The utility of $CsTiSi_2O_{6.5}$ and $Cs_2TiSi_6O_{15}$ as waste forms for Cs containment can be estimated by comparing the Cs leach rates to borosilicate glass; the baseline wasteform for high activity waste. The Cs leach rate using a static leach test similar to MCC-1, of a borosilicate waste glass simulant, R7T7, is $0.16\ g\ m^{-2}\ d^{-1}$ after 14 days.¹⁰ The 14 day leach rate of $CsTiSi_2O_{6.5}$ ($1.8\ g\ m^{-2}\ d^{-1}$) is higher than the borosilicate simulant, whereas that of $Cs_2TiSi_6O_{15}$ ($5 \times 10^{-4}\ g\ m^{-2}\ d^{-1}$) is four orders of magnitude lower. These results suggest that $Cs_2TiSi_6O_{15}$ would serve as an excellent wasteform. Although the Cs leach rate of $CsTiSi_2O_{6.5}$ is somewhat higher than borosilicate glass it is within the necessary durability range, and further leach tests on this compound using an exact surface area determination are warranted. It is worth noting that the Cs content and total alkali content of R7T7 (1.42 wt% and 13.26 wt%) are much lower than the Cs content of $CsTiSi_2O_{6.5}$ (42 wt% or 14 mol% Cs_2O) and $Cs_2TiSi_6O_{15}$ (39 wt% or 12.5

mol%).¹⁰ At very high alkali contents, similar to the silicotitanate zeolites, the durability of most silicate glasses is greatly diminished. For example, the leach rate of a silicate glass that contains 15 mol% potassium is 8 g m⁻² d⁻¹ at 85°C.¹¹ From these results, a silicate glass with 14 mol% Cs₂O (28 mol% Cs) is estimated to exhibit leach rates as high as 15 g m⁻² d⁻¹.

CONCLUSIONS

Both CsTiSi₂O_{6.5} and Cs₂TiSi₆O₁₅ have unique crystal structures where the Cs resides in cages formed by rings of corner sharing silica and titania polyhedra. The largest ring opening size in both structures is smaller than the effective ionic diameter of a Cs ion, indicating that Cs has limited mobility in the structure. The rate of Cs release from CsTiSi₂O_{6.5} is higher than Cs₂TiSi₆O₁₅, however, the preliminary leach rate results indicate that both materials may act as suitable waste forms for Cs containment.

ACKNOWLEDGEMENT

The authors would like to gratefully acknowledge Mr. Dave McCready for performing x-ray powder diffraction and Dr. Terrell Vanderah for assistance in fabricating single crystal specimens. Partial support for this work was provided by the Strategic Environmental Research and Development Program (SERDP).

REFERENCES

1. R.G. Dosch, N.E. Brown, D.E. Trudell, R.G. Anthony, D. Gu and C. Thibaud-Erkey, Waste Management 94, February 28, Tucson, AZ, pp. 709-719.
2. Y. Su, M.L. Balmer, and B.C. Bunker, Submitted Materials Research Society Proceedings, Boston, MA (1996).
3. D.E. McCready, M.L. Balmer, and K.D. Keefer, Powder Diffraction, in press.
4. M.L. Balmer, Q. Huang, W. Wong-Ng, R.S. Roth, and A. Santoro J. Sol. State Chem. accepted.
5. N.J. Hess and M.L. Balmer, J. Sol. State Chem., submitted.
6. I.E. Grey, R.S. Roth, and M.L. Balmer, J. Sol. State Chem. submitted.
7. S. Komareni, G.J. McCarthy, and S.A. Gallagher, Inorg. Nucl. Chem. Letters, Vol. 14, pp. 173-177, 1978.
8. E.R. Vance, B.E. Scheetz, M.W. Barnes, and B.J. Bodnar in The Scientific Basis for Nuclear Waste Management, edited by Stephen V. Topp (Elsivier Science Publishing Co. Inc., 1982).
9. K. Yanagisawa, M Nishoka, and N. Yamasaki, J. Nuc. Sci. Tech., 24[1], pp. 51-60, 1987.
10. J.L. Nogues, E.Y. Vernaz, and N. Jacquet-Francillon in The Scientific Basis for Nuclear Waste Management, Vol. 44 edited by Carol M. Jantzen, John A. Stone, and Rodney C. Ewing, (Materials Research Society, 1984).
11. M.A. Rana, and R.W. Douglas, Phys. And Chem. Of Glasses, Vol. 2, No. 6, pp. 179-195.

Section 1b

Neutron and X-Ray Diffraction Study of the Crystal Structure of $\text{CsTiSi}_2\text{O}_{6.5}$

Neutron and X-Ray Diffraction Study of the Crystal Structure of $\text{CsTiSi}_2\text{O}_{6.5}$

M.L. Balmer⁽¹⁾, Q. Huang^(2,3), W. Wong-Ng⁽³⁾, R. S. Roth⁽³⁾ and A. Santoro⁽³⁾

(1) Battelle, Pacific Northwest National Laboratory, Richland, WA 99352

(2) University of Maryland, College Park, MD 20742

(3) National Institute of Standards and Technology, Gaithersburg, MD 20899

February 23, 1996

Abstract

The structure of the silicotitanate $\text{CsTiSi}_2\text{O}_{6.5}$ has been analyzed with neutron powder and x-ray single crystal diffraction techniques. The compound crystallizes with the symmetry of space group $Ia\bar{3}d$ and lattice parameter $a=13.8417(7)\text{\AA}$. There are sixteen formula units in the unit cell. The basic structure of the silicotitanate is similar to that of pollucite and consists of a framework of corner sharing MO_4 tetrahedra ($\text{M}=1/3 \text{ Ti} + 2/3 \text{ Si}$) forming large voids in which the Cs^+ cations are located. Titanium and silicon are disordered over the $48g$ sites of the cubic space group. Compared to pollucite, there are eight extra oxygen atoms in the unit cell. These atoms partially occupy two sets of general sites and are bonded to both the cesium and the M cations of neighboring tetrahedra.

1 INTRODUCTION:

The discovery of silicotitanate ion exchangers for removal of Cs from radioactive, Na-rich wastes has stimulated research efforts in the preparation and characterization of new silicotitanate materials [1, 2]. One of the new compounds recently synthesized is a derivative of the cesium aluminosilicate pollucite, $CsAlSi_2O_6$, in which the Ti^{4+} replaces Al^{3+} [3, 4]. This substitution requires a mechanism for charge compensation, such as the presence of tri-valent titanium cations, or the incorporation of oxygen in excess of six atoms per formula unit into the structure. X-ray photoelectron spectroscopy and electron paramagnetic resonance measurements show that Ti is primarily in the Ti^{4+} state, therefore eliminating the possibility of Ti^{3+} substitution for Al^{3+} . Ti x-ray absorption near edge structure and raman spectroscopy results indicate that the Ti exists in 5-fold coordination with oxygen [5]. Therefore, it is hypothesized that the mechanism of charge compensation is incorporation of excess oxygen into the pollucite structure resulting in the stoichiometry $CsTiSi_2O_{6.5}$.

Neutron powder and x-ray single crystal diffraction experiments presented herein were undertaken in order to elucidate the complete crystal structure, and in particular, to determine the location of extra oxygen in the unit cell of $CsTiSi_2O_{6.5}$. Based on the atomic scattering amplitudes for neutrons, neutron diffraction analysis is expected to clarify oxygen positions. X-ray diffraction, on the other hand, is relatively insensitive to small changes in the oxygen position, but can more precisely measure the cation positions and temperature factors. A complete description of the structure and clarification of the cation environments will facilitate the determination of structure-property relationships and the development of new materials with tailored properties.

2 EXPERIMENTAL

A. Preparation of the sample.

Crystalline $\text{CsTiSi}_2\text{O}_{6.5}$ was prepared via a sol-gel processing route. First, an amorphous, homogeneous precursor was synthesized using tetra-isopropyl orthotitanate (TIOT), tetraethyl orthosilicate (TEOS), and cesium hydroxide. The alkoxides were mixed in a glove bag under nitrogen and then a mixture of CsOH , water and ethanol was added. The resulting hydrolyzed precursor was stirred for a minimum of 15 hours, then dried in air at room temperature. X-ray diffraction and TEM/EDS analysis showed that the precursor was both homogeneous and amorphous. Approximately 0.5 grams of this material was then heat treated in a platinum crucible in air to produce crystalline $\text{CsTiSi}_2\text{O}_{6.5}$.

Two heat treatment schemes were applied to the precursor. In the first, the material was heated from room temperature to 800°C at the rate of $5^\circ\text{C}/\text{min.}$, then held at 800°C for at least one hour. In this procedure, the onset of the formation of crystalline $\text{CsTiSi}_2\text{O}_{6.5}$ was observed at 750°C and full crystallization occurred at 800°C . Upon further heating the sample melted at 980°C . In the second scheme, the stoichiometric precursor was melted at 1200°C , then quenched to form a clear glass. The quenched glass was then ground to fine powder and heat treated at 800°C for 30 hours. Both these methods produced the same crystallized material. The sample used in the neutron diffraction experiment was produced with the first scheme previously described.

Single crystals of $\text{CsTiSi}_2\text{O}_{6.5}$ were grown from a powdered sample of the compound, using CsVO_3 as a flux. A mixture of $\text{CsTiSi}_2\text{O}_{6.5}$ and CsVO_3 was placed into a Pt tube, which was then sealed at both ends and heated in a vertical tube furnace at the rate of $50^\circ\text{C}/\text{hr}$ to 1100°C , held for one hour at this temperature, then cooled to 650°C at the rate of $1^\circ\text{C}/\text{hr}$, and finally cooled to room temperature. The flux was dissolved in warm H_2O and crystals of the title compound were isolated from a mixture of phases comprising TiO_2 , cristobalite and a new Cs-Ti silicate. Samples of quality suitable for single crystal work were selected using a polarising microscope.

B. Data collection and refinement of the structure

The neutron powder diffraction measurements were made with the new high-resolution powder diffractometer at the National Institute of Standards and Technology reactor, using the experimental conditions listed in Table 1. The profile refinements were carried out using the General Structure Analysis System (GSAS) Program of Larson and Von Dreele [6]. The observed diffraction lines could be readily indexed in terms of a cubic unit cell of lattice parameter close to that reported for cubic pollucite [7 - 9], giving a strong indication that the structures of $\text{CsTiSi}_2\text{O}_{6.5}$ and $\text{CsAlSi}_2\text{O}_6$ are basically the same. A few very weak extra reflections present in the powder pattern could not be indexed in terms of any of the derivative lattices of the cubic cell and were therefore attributed to impurities in the sample and excluded from all subsequent calculations. The first structural refinement was carried out assuming the cubic atomic arrangement of pollucite, with the Ti^{4+} and Si^{4+} cations disordered over the sites $48g$ of space group $Ia\bar{3}d$, Cs^+ located in $16b$, oxygen in the general position $96h$, and ignoring the presence of the extra oxygen atoms in the structure. This first set of calculations gave reasonable agreement between observed and calculated intensities and acceptable bond distances, thus confirming the previous observation that the structure of the title compound is indeed similar to that of pollucite. Attempts were made to refine models based on the symmetry of space groups $I4_1/acd$ and $I4_1/a$ in which the sites $48g$ of the Ti^{4+} and Si^{4+} cations are split, thus providing the possibility for the ordering of these cations. Refinements based on these models were unsuccessful, due to high correlations between the parameters varied in the refinement. These results further confirm the cubic symmetry of the sample used in the experiment.

The additional eight oxygen atoms contained in the unit cell of the title compound can be distributed over any of the positions available in space group $Ia\bar{3}d$. Special position $24c$ ($\frac{1}{4}, \frac{1}{8}, 0$) (which was found to be partially occupied by Na^+ cations in the structure of $\text{Cs}_{12}\text{Na}_4\text{Al}_{16}\text{Si}_{32}\text{O}_{96} \cdot 4\text{H}_2\text{O}$, [7]) is an unlikely site for the extra oxygen because it results in unrealistically short Cs-O distances of about 2.45\AA . Not surprisingly, a refinement of this model gave agreement factors between observed and calculated intensities not significantly different from those obtained for the model with O_6 stoichiometry (Table 2), and, more importantly, attempts to refine the occupancy of the extra oxygen atoms resulted in negative values of the occupancy factor. The position $24d$ ($\frac{3}{4}, \frac{1}{8}, 0$) was

eliminated because of similar crystal-chemical arguments and because of unsatisfactory refinement results.

In order to determine possible locations of the extra oxygen atoms, a Fourier difference map was calculated after the refinement of the structural model in which these atoms had not been included. Of the several weak peaks present in the map, only two gave acceptable Cs-O and M-O distances ($M=1/3$ Ti + $2/3$ Si). These were located in general positions with approximate coordinates x, y, z equal to 0.79, 0.21, 0.24 and 0.71, 0.06, 0.02. Refinements of models in which the atoms were located in only one of these two positions, gave agreement factors not significantly different for the two cases (Table 2), indicating that neither set of coordinates can be excluded a priori from the structural model. For this reason both positions were retained in the subsequent calculations, and the extra oxygen atoms were distributed uniformly over the two sets of sites. Since the M cations ($M=1/3$ Ti + $2/3$ Si) have a low value of the scattering amplitude compared to Cs and O ($b(M)=0.162 \times 10^{-12}$ cm), their positional parameters and temperature factor could only be determined with low precision from the neutron powder pattern. For this reason it was decided to refine the structure also using x-ray single crystal intensity data. The x-ray intensities were measured with CAD4 diffractometer, using the conditions listed in Table 3*. Twenty five reflections with $13^\circ < \theta < 19^\circ$ were employed in the least squares determination of the lattice constant. Crystal stability and orientation were monitored throughout the experiment by periodically checking the intensities of six standard reflections. The raw intensities were corrected for Lorentz and polarization effects, and the absorption correction was evaluated with the psi absorption scheme. The initial parameters used in the x-ray refinements were those obtained previously in the neutron experiment. The initial structural model, which did not include the extra oxygen atoms, yielded a value of the R factor of 3.4%, confirming again the general features of the structure. When the extra oxygen was included at the positions determined from the neutron data, this value slightly decreased to 3.2%.

The results from the final x-ray and neutron refinements are given in Table 4 together with the relevant bond distances. The agreement between observed and calculated neutron intensities is shown in the plot of Fig. 1.

*The purpose of identifying this equipment in this article is to specify the experimental procedure. Such identification does not imply recommendation or endorsement by the National Institute of Standards and Technology.

3 DISCUSSION

The structural parameters listed in Table 4 show that all the atoms in the structure of $\text{CsTiSi}_2\text{O}_{6.5}$ have unusually high temperature factors. This result is not surprising, since the presence of eight extra oxygen atoms in the unit cell, combined with the disordering of the Si^{4+} Ti^{4+} cations over the same crystallographic sites is, in general, associated with local shifts of some of the atoms and, consequently, with high thermal parameters. Similar results have been reported previously for compounds with similar structures. In the case of $\text{Cs}_{12}\text{Na}_4\text{Al}_{16}\text{Si}_{32}\text{O}_{96} \cdot 4\text{H}_2\text{O}$, water molecules and Cs^+ cations are disordered over the same crystallographic sites [7]. In our case, the presence of water in the structure can be excluded since the neutron powder pattern does not show abnormally high background.

The oxygen atoms O(1) form a network of corner-sharing tetrahedra practically identical to the one described for pollucite [7, 8]. The configuration of the tetrahedra in the immediate vicinity of a central cesium atom is schematically represented in Figure 2 in projection along the [111] axis of the cubic unit cell. As indicated in the figure, six-membered loops of tetrahedra form channels along the [111] direction (as well as along the other three-fold axes), with the Cs^+ cations located in the channels and bonded to twelve O(1) oxygen atoms with distances of 3.424(4) and 3.573(4) Å. These bond distances, as well as the M-O separations reported in Table 4, agree very closely with the corresponding values reported for pollucite [7]. The distribution of the O(2) atoms around cesium is illustrated in Figure 3, and the environment of one of these atoms is shown in greater detail in Figure 4, where the Cs-O(2) and M-O(2) distances are also indicated. We have to point out, however, that the distances reported in Table 4 represent average values and that, on a local level, these separations may be significantly different due to shifts of the atoms involved in the bonding. It is reasonable to assume that a site O(2) is occupied by an oxygen atom only when the centers of neighboring tetrahedra are occupied by titanium, rather than silicon. This is in agreement with ^{29}Si NMR Studies and Ti-EXAF results published elsewhere which show that both four and five-coordinated Ti is present in the structure [5, 10]. The O(3) sites are clustered above and below the cesium along the three-fold axes, as shown in Figure 5, and form rings within

which O(3)-O(3) separations are as short as 0.8 Å. Consequently, only one atom of oxygen can be present in each ring, located on any one of the available sites. The distances reported in Table 4 show that O(3) has strong bond with cesium and a weak bond with M. As a consequence of the presence of extra oxygen in the unit cell of $\text{CsTiSi}_2\text{O}_{6.5}$, the average coordination of the central Cs^+ cation is thirteen-fold, rather than twelve-fold as in pollucite. In addition, when an O(2) site is occupied by oxygen, the coordination of the M cations located at the centers of the neighboring tetrahedra is five-fold, rather than four-fold, as shown in Figure 4.

Some O(1)-O(2) and O(1)-O(3) distances in this structure are unreasonably short (of the order of 1.7-1.8 Å). Since the O(1) position is fully occupied, this means that not all the O(2) and O(3) sites are available to the extra oxygen atoms. This may result in ordering of the oxygen vacancies, and possibly, lowering of the structural symmetry. As mentioned previously, however, the thermal parameters obtained in the refinement indicate that large distortions are possible, with some of the atoms locally shifted from their average positions by about 0.3 Å. It is the existence of these shifts that makes the positions given in Table 4 for O(2) and O(3) acceptable as possible locations of the extra oxygen in the unit cell.

4 Bibliography

(1) B. C. Bunker, Pacific Northwest Laboratory, PNL Report, TWRSP-94-085, September, 1994.

(2) R. G. Anthony, C. V. Phillip and R. G. Dosch, Waste Management 13, 503 (1993).

(3) M. L. Balmer and B. C. Bunker, PNL-10460, March 1995.

(4) D. E. McCready, M. L. Balmer and K. D. Keefer, Powder Diffraction, submitted.

(5) N. J. Hess and M. L. Balmer, J. Solid State Chem., submitted.

(6) A. C. Larson and R. B. Von Dreele, General Structure Analysis System. Report LA-UR-86-748, Los Alamos National Laboratory, Los Alamos, NM 87545 (1990).

(7) R. M. Beger, Zeit. Kristallographie 129, 280 (1969).

(8) R. E. Newnham, Am. Mineralogist, 52, 1515 (1967).

(9) R. F. Martin and M. L. Agache, Canadian Mineralogist 13, 275 (1975).

(10) M. L. Balmer, L. Q. Wang, C. H. F. Peden and B. C. Bunker, unpublished work.

5 Figure Captions

Fig. 1. Observed (crosses) and calculated (continuous line) intensities in the neutron powder pattern of $\text{CsTiSi}_2\text{O}_{6.5}$. The difference, $I(\text{obs})-I(\text{cal})$, is shown in the plot in the lower part of figure. The short vertical lines mark the 2θ angles of the Bragg reflections. The three angular intervals with no data shown, are the regions affected by weak peaks attributed to impurities in the sample. These regions were excluded in the refinement.

Fig. 2. View along one of the $\langle 111 \rangle$ axes of the distribution of the MO_4 tetrahedra around a Cs^+ cation. The oxygen atoms O(1) bonded to the cesium are indicated by the Cs-O lines.

Fig. 3. Locations of the O(2) oxygen atoms (hatched circles) around a Cs^+ cation. This figure is a projection along one of the three-fold axes. On the average, each O(2) site is occupied by 0.063 atoms.

Fig. 4. Environment of one of the O(2) extra oxygen (the atom represented in this figure is the one identified by an arrow in Figure 3).

Fig. 5. Distribution of the O(3) sites around a central Cs^+ cation. The two O(3) rings are located above and below the cesium. On average each O(3) site is occupied by 0.023 atoms.

Table 1. Collection of neutron powder diffraction data.

Monochromatic beam:	311 reflection of a Cu monochromator
Wavelength:	1.5396 Å
Horizontal divergences:	15', 20, 7' of arc for the inpile, monochromatic, and diffracted beam collimators, respectively
2θ angular range:	3 — 168°, steps: 0.05°
Scattering amplitudes (10^{-12} cm):	$b(\text{Cs})=0.542$, $b(\text{Si})=0.415$, $b(\text{Ti})=-0.344$, and $b(\text{O})=0.581$

Table 2. Refinement in different structural models.

	No extra oxygen	Extra O at (1/4,1/8,0)	Extra O at (3/4,1/8,0)	O(3)	O(2)	O(3)+O(2)
R_p	6.70	6.52	6.25	6.03	5.73	5.66
R_{wp}	7.75	7.62	7.41	7.07	6.90	6.79
χ^2	1.38	1.33	1.26	1.15	1.09	1.06
a (Å)	13.8418(8)	13.8418(7)	13.8417(7)	13.8418(7)	13.8417(7)	13.8417(7)

Table 3. Crystal data and summary of intensity data collection and structure refinement.

Color	Colorless
Formula weight	340.97
Temp., °C	≈25
Radiation, graphic monochromator	Mo, 0.71073
Crystal dimensions, mm	0.12×0.10×0.06
Crystal data	
Space group	Ia $\bar{3}$ d
Cell constants*, Å	13.8359(14)
Formula units/unit cell	16
Data Collection	
Total reflections measured	3598
Independent reflections	703
Observed reflections*	158
θ range, °	28
Range of transm. factors, ** %	82.4 to 100, Ave. 92.1
Refinements	
$R = \sum F_o - F_c / \sum F_o $	0.032
R_w	0.048
No. parameters varied	13
Weights**	non-Poisson, $p=0.4$
Extinction coefficient	1.279×10^{-7}
GOF	1.5
Largest shift/error	0.01

* CAD4 operation manual, Enraf-Nonius, Delft, The Netherlands (1977).

** Molen, Structure solution package provided by Enraf-Nonius, Inc. (1991). Scattering factors from: D.T.Cromer and J.T.Waber, International Tables for x-ray Crystallography, Vol. IV. The Kynoch Press, Birmingham, UK (1974).

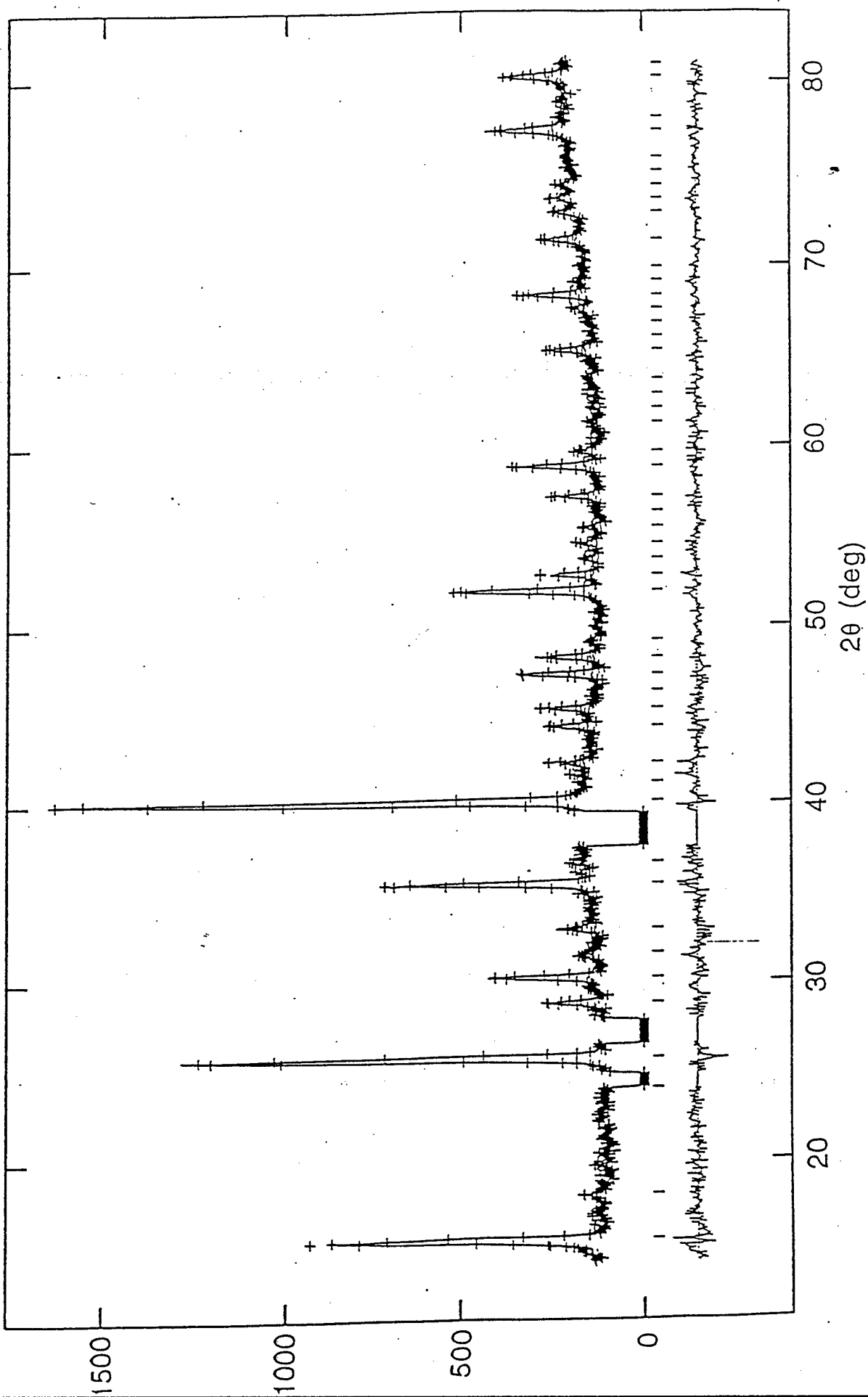
Table 4. Structural parameters and selected bond distances (Å) of $\text{CsTiSi}_2\text{O}_{6.5}$ at 295 K.Space group: $\text{Ia}\bar{3}\text{d}$, neutron(first line) $a=13.8417(7)$ Å, x-ray(second line) $a=13.8359(14)$ Å, $z=16$.

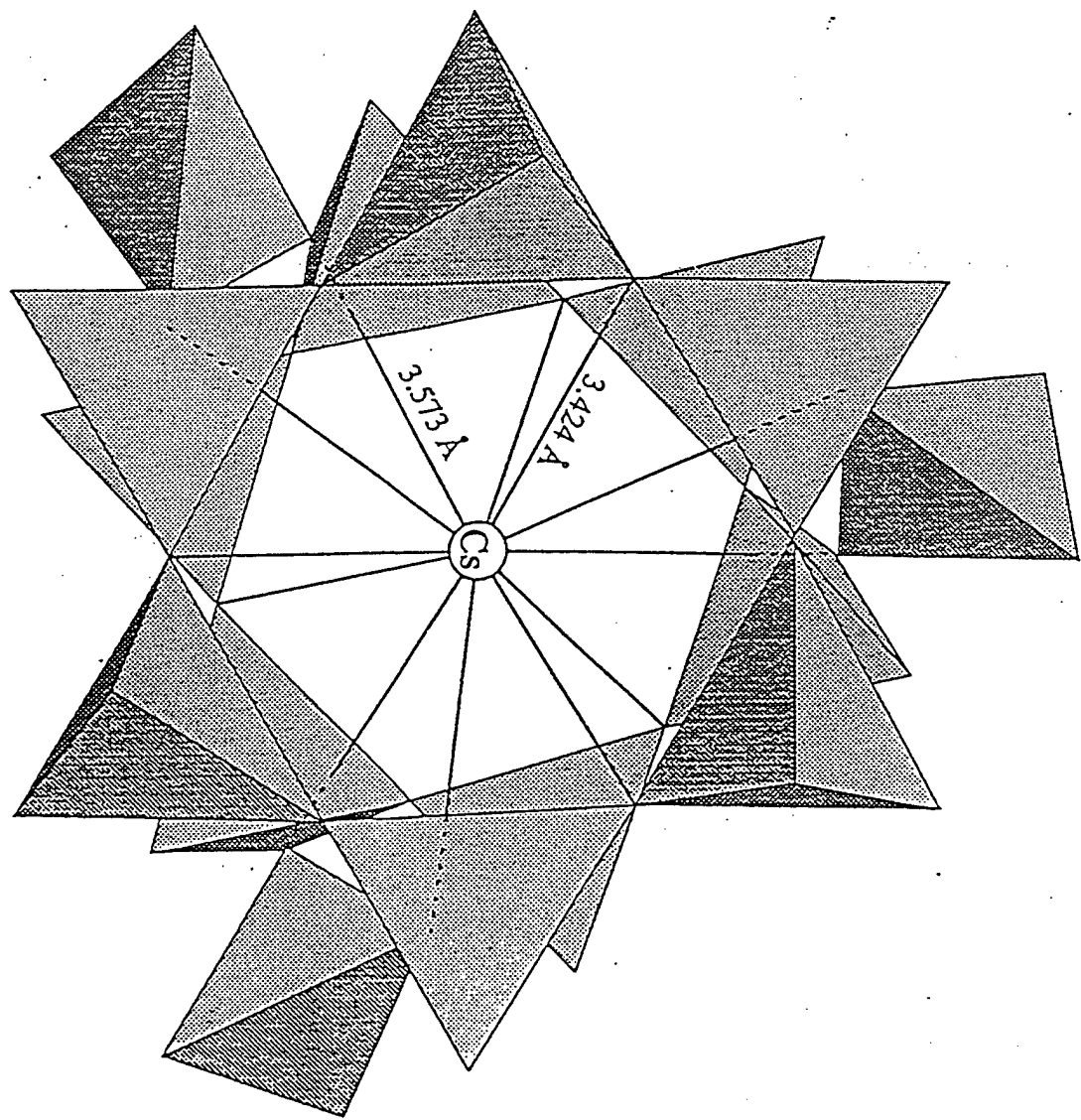
Atom	Site	x	y	z	B (Å ²)	Occup.
Cs	16b	.32	1/8 "	1/8 "	1/8 "	4.0(2) 3.645(7)
Ti	48g	..2	0.661(1) 0.6639(2)	0.589(1) 0.5861(2)	1/8 "	6.3(5) 2.85(4)
Si	48g	..2	0.661(1) 0.6639(2)	0.589(1) 0.5861(2)	1/8 "	6.3(5) 2.85(4)
O(1)	96h	1	0.1042(3) 0.1047(5) [B(11) [8.8(3)	0.1349(3) 0.1353(5) B(22) 8.0(3)	0.7175(3) 0.7171(7) B(12) 4.2(2)	1 1 B(13) 1.6(2)
O(2)	96h	1	0.706 "	0.062 "	0.021 "	4.8 "
O(3)	96h	1	0.791 "	0.205 "	0.235 "	4.8 "

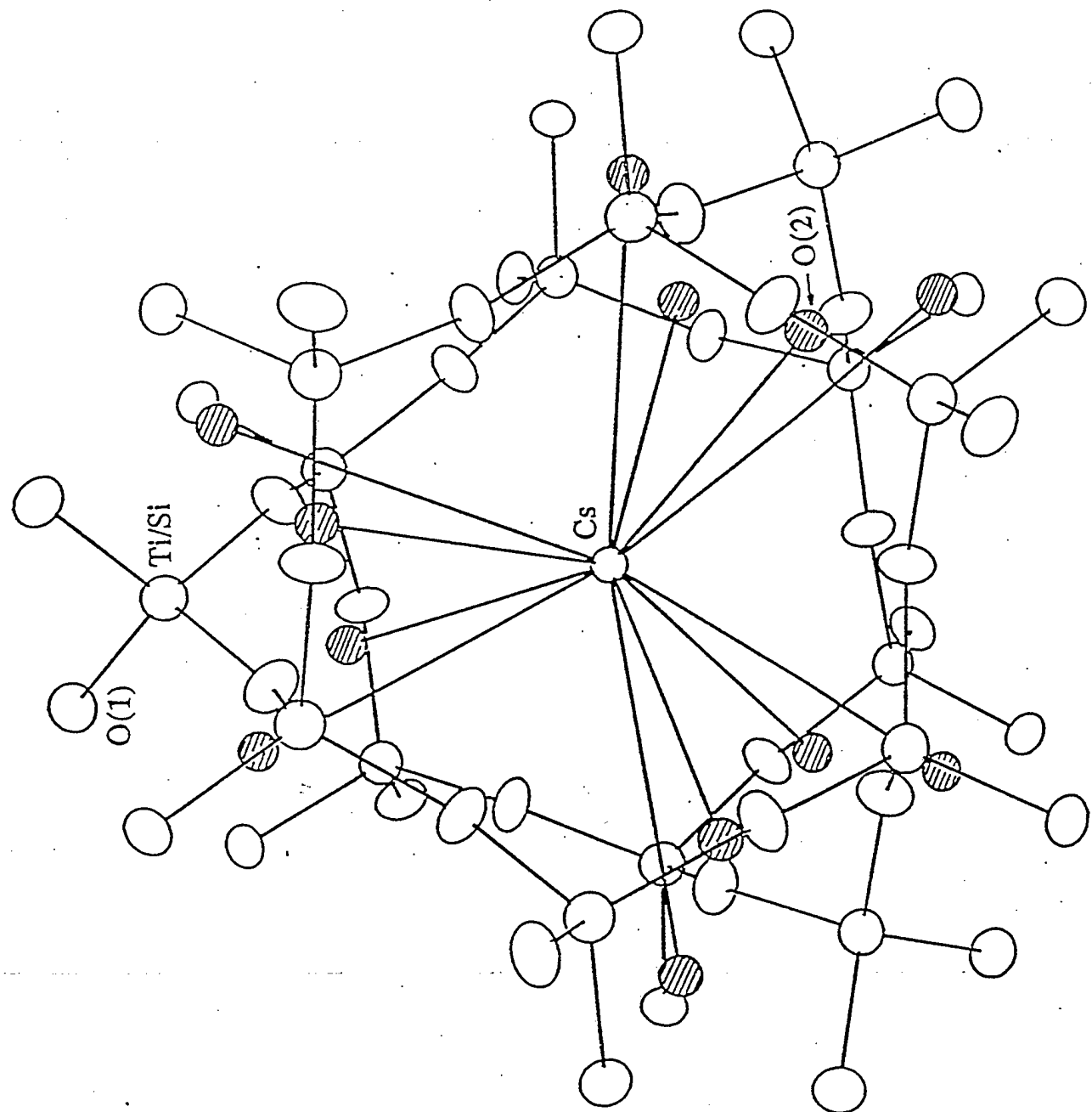
 $R_p=5.66$, $R_{wp}=6.80$, $\chi^2=1.06$.

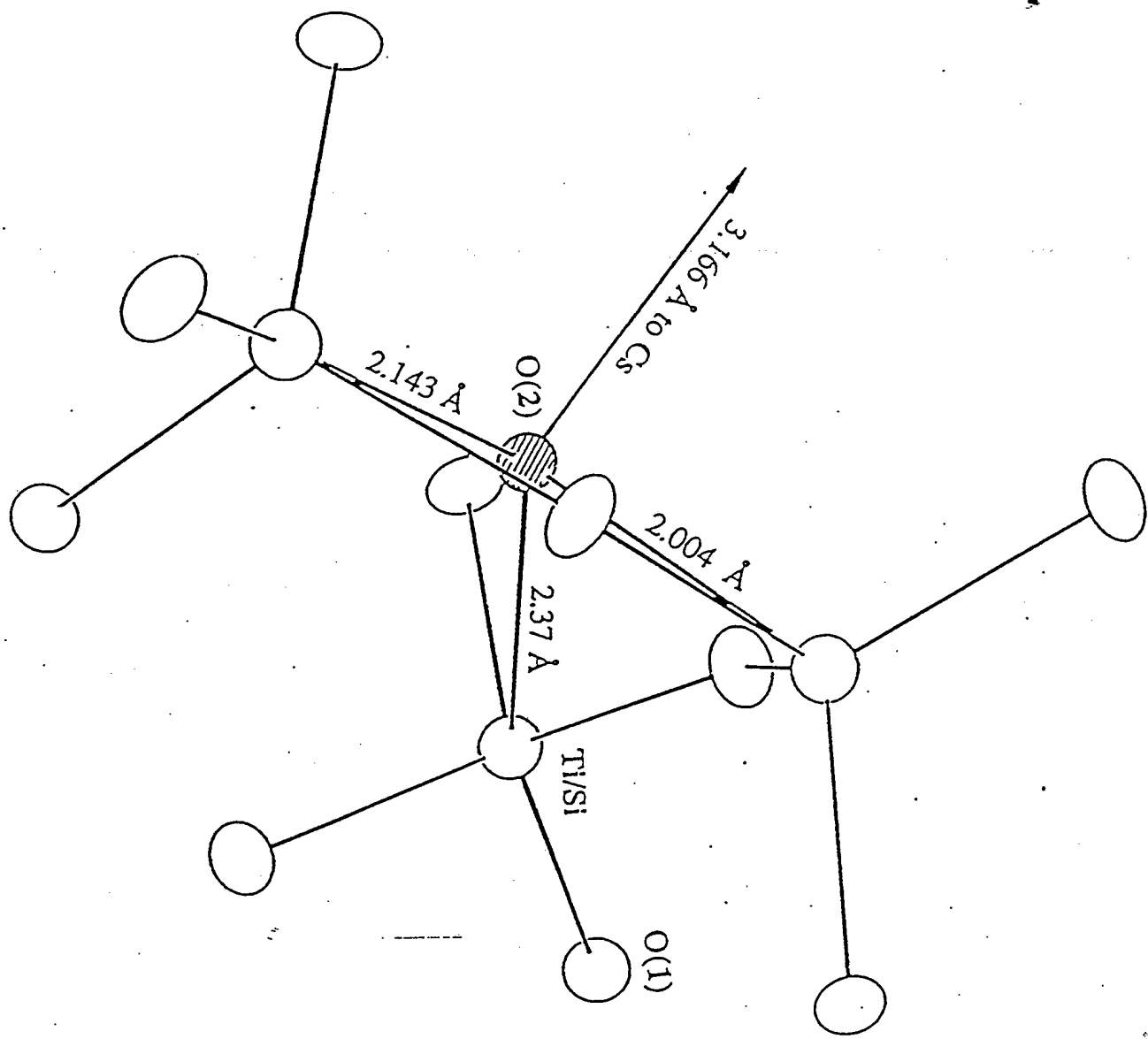
Selected bond distances (Å)

Cs — O(1)	$\times 6$	3.424(4) 3.427(9)	Ti/Si — O(1)	$\times 2$	1.70(1) 1.67(1)
Cs — O(1)	$\times 6$	3.573(4) 3.564(8)	Ti/Si — O(1)	$\times 2$	1.63(1) 1.66(1)
Cs — O(2)		3.17 "	Ti/Si — O(2)		2.00 2.01
Cs — O(2)		4.03 "	Ti/Si — O(2)		2.14 2.13
Cs — O(3)		3.03 "	Ti/Si — O(2)		2.37 2.33
Cs — O(3)		3.20 "	Ti/Si — O(3)		2.31 2.33
			Ti/Si — O(3)		2.46 2.46









Section 1c

The Crystal Structure of $\text{CsTiSi}_6\text{O}_{15}$

The Crystal Structure of $Cs_2TiSi_6O_{15}$

I.E. GREY⁽¹⁾, R.S. ROTH⁽²⁾ and M.L. BALMER⁽³⁾

- (1) CSIRO Division of Minerals, Melbourne, Australia
- (2) National Institute of Standards and Technology, Gaithersburg, MD 20899
- (3) Battelle, Pacific Northwest National Laboratory, Richland, WA 99352

ABSTRACT

Crystals of a new titanosilicate phase, $Cs_2TiSi_6O_{15}$, were grown from a cesium vanadate flux. The compound has monoclinic symmetry, space group C2/c, with $a = 13.386(5)$, $b = 7.423(3)$, $c = 15.134(5)$ Å, $\beta = 107.71(3)^\circ$, $Z = 4$. The crystal structure was solved using single crystal x-ray data (Mo $K\alpha$ radiation) and refined to $R(F) = 0.039$ for 1874 unique reflections. In the structure, isolated titanium-centred octahedra and silica-centred tetrahedra share all corners to form an open framework structure containing large cavities in which the cesium ions are located. Each cavity is bound by three 5-rings, two 6-rings and two 8-rings. The cavities are linked via the 8-rings into channels parallel to [101]. The cesium ions occur in pairs along the channels, separated by 3.765(2) Å.

INTRODUCTION

An important new development in inorganic microporous materials was the discovery in 1989 of a family of microporous titanosilicates, incorporating octahedrally coordinated Ti^{4+} ions (1,2). The TiO_6 octahedra corner-link to SiO_4 tetrahedra to form the host framework. Members of the family have been commercially developed (Engelhard Corporation titanosilicates, ETS) for application as molecular sieves and selective catalysts (1). These compounds extended earlier developments in catalyst chemistry, based on enhanced selective catalytic activity of microporous silicas by partial isomorphous replacement of tetrahedrally coordinated Si^{4+} by Ti^{4+} (3).

Further stimulus for research on the preparation and characterisation of titanosilicates has come from the recognition that these compounds are effective ion exchangers for selective removal of cesium from radioactive, sodium-rich wastes (4). Recent work at Pacific Northwest National Laboratory of Battelle has shown that certain $Cs_2O-TiO_2-SiO_2$ compositions can be thermally converted to crystalline titanosilicates with high durabilities towards leaching (5). One of the new compounds, with composition $CsTiSi_2O_{6.5}$, has a zeolitic structure closely related to that for pollucite, $CsAlSi_2O_6$ (6). Pollucite has been reported to be an excellent candidate for cesium containment (7). Whereas pollucite contains only tetrahedrally coordinated cations, the titanium derivative has 5-coordinated Ti^{4+} (6).

As part of a program on the characterisation of $CsTiSi_2O_{6.5}$, single crystals were grown from a cesium vanadate flux. In addition to the desired compound, crystals were also obtained of another cesium titanosilicate with a higher silica content, $Cs_2TiSi_6O_{15}$. The x-ray diffraction data and unit cell dimensions for the second phase could not be reconciled with any known structure type. We report here the structural characterisation of this phase.

EXPERIMENTAL

Synthesis and characterisation.

A mixture of 0.08 g of microcrystalline $CsTiSi_2O_{6.5}$ and 0.07 g of $CsVO_3$ was sealed in a 3 mm diameter platinum tube. The tube was placed in a vertical tube furnace at 800°C. The temperature was increased to 1100°C at a heating rate of 50°C/h, held for one hour at 1100°C, then cooled to 650°C at a rate of 1°C/h. Despite being sealed the flux was found to have penetrated the walls of the tube and crystals were found both outside and inside the tube. After dissolving the flux in warm water, crystals of four different phases were identified. Three of these were known phases, $CsTiSi_2O_{6.5}$, rutile and cristobalite. The fourth, and most

prevalent phase comprised relatively large (0.1-0.5 mm) tabular-shaped crystals, showing high birefringence under a polarising microscope.

Several of the crystals were examined by x-ray diffraction using the precession method. They were all found to be single crystals having C-centred monoclinic symmetry, with approximate cell dimensions $a = 13.4$, $b = 7.4$, $c = 15.1 \text{ \AA}$, $\beta = 108^\circ$. The dominant faces of the plate-like crystals was found to be (001). Systematic absences in the precession photos were consistent with the space groups C2/c and Cc.

Wavelength dispersion electron microprobe analyses were made on sectioned and polished crystals using a JEOL Superprobe model JXA-8900R operated at 15 kV and 20 nA. Standards used were pollucite, rutile and vanadium metal. The analyses showed small variations within and between crystals. The ranges obtained were 36.0 - 37.4 wt% Cs, 22.5 - 23.3 wt% Si, 7.2 - 8.7 wt% Ti and 0.5 - 0.6 wt% V.

Data collection and structure analysis

For the data collection, a tabular crystal was mounted along b on a Siemens AED diffractometer employing Mo K α radiation. Lattice parameters were determined by the least squares technique applied to the setting angles of reflections with $11 < \theta < 26^\circ$. Intensities were collected using θ - 2θ scans. Three standard reflections which were monitored every 50 reflections to correct for intensity drift showed no significant deviations. Details of the data collection, data processing and structure refinement are given in Table 1.

Working in the centrosymmetric space group C2/c, the positions of a cesium and a titanium atom were obtained from an analysis of the three dimensional Patterson map. The silicon and oxygen atoms were located in successive Fourier and difference Fourier maps. Refinement of all coordinates, isotropic displacement parameters and an extinction parameter converged at a high $R(F)$ value of 0.15. Release of anisotropic displacement parameters resulted in a rapid convergence to $R(F) = 0.039$ for all 1874 independent reflections. The refinement was based on F^2 s and the final $wR(F^2)$ was 0.13. Some of the oxygen atoms had large anisotropic displacement parameters. Attempts to model these with split atoms and with refinements in Cc gave no further improvement in the R values. The highest peaks in the difference Fourier map obtained after the final refinement were 1.2 and 1.4 e/ \AA^3 , close to the cesium atoms.

The data processing, including the absorption correction, was made using SHELX-76 (8) and the structure refinement was carried out with SHELXL93 (9).

RESULTS AND DISCUSSION

The refined atomic coordinates and equivalent isotropic displacement parameters are reported in Table 2. The anisotropic displacement parameters are given in Table 3. Selected interatomic distances and angles are presented in Table 4.

From the structure refinement, the unit cell composition was established to be $Cs_8Ti_4Si_{24}O_{60}$, ie $4 \times Cs_2TiSi_6O_{15}$. The calculated analyses for this composition are 36.8 wt% Cs, 23.3 wt% Si and 6.6 wt% Ti. The cesium and silicon analyses are within the range of measured microprobe values but the titanium is lower than the measured range of 7.2-8.7% Ti. There was no evidence of other partially occupied sites in the final difference Fourier map that could be occupied by excess titanium. A possible explanation is that minor substitution of silicon by titanium occurs, as found for $CsTiSi_2O_{6.5}$ (6), although the Si-O bond lengths listed in Table 4 show no evidence for this. They are, if anything, on the low side for Si-O. Repeat microprobe analyses using different standards for titanium ($CaTiSi_2O_5$ and $BaTiSi_3O_9$) showed small but consistent variations in the titanium analyses as a function of the standard used and so some doubt is cast on the accuracy of the microprobe results for titanium.

The structure building units are a titanium-centred octahedron, a Si_2O_7 group containing Si(1) and two further silicon-centred tetrahedra containing Si(2) and Si(3). The polyhedra are connected by corner-sharing of all vertices to form an open framework. There are only Ti-O-Si and Si-O-Si linkages between polyhedra. The TiO_6 octahedra are indirectly linked to one another via two intervening SiO_4 tetrahedra. The polyhedral linkages create large cages in which the cesium ions reside. The cages are formed by a three-ring, three 5-rings, two 6-rings and two 8-rings.

A polyhedral representation of the structure, viewed down the unique axis, *b*, is given in Fig. 1. This view shows clearly the 5-rings and 6-rings. The former involves the edges of a TiO_6 octahedron, a $Si(1)_2O_7$ group and two SiO_4 tetrahedra, while the latter includes an additional octahedral edge. A second type of 5-ring, which is perpendicular to the section shown in Fig. 1, involves the edges of five tetrahedra. It is seen from Fig. 1 that parallel to (001), narrow blocks containing only TiO_6 octahedra are separated by blocks containing zig-zag chains of Si_2O_7 groups. The Si_2O_7 groups are oriented approximately along [101] and [100] in the chains. These chains are linked vertically by further corner sharing into blocks parallel to (001). This plane is the main growth plane of the platy or tabular crystals.

From Fig. 1 it is seen that the cesium ions form undulating rows, oriented along [101]. Alternately short and long Cs-Cs separations occur along the rows with distances of 3.765(2) and 4.904(2) Å. The next shortest Cs-Cs separation is

5.946(2) Å, between cesium ions in adjacent [101] rows. Fig. 2 shows a view of the structure parallel to the [101] rows of cesium ions. It is seen that the cavities containing the cesium ions have large apertures normal to this direction, formed from 8-rings of two types. One is formed from the edges of eight tetrahedra (8T) while the other is formed from the edges of six tetrahedra and two octahedra (6T+2O). Both apertures are compressed into elliptical shapes. The principal axes of the two types of ellipses are orthogonal. The cavities containing cesium ions are connected via these apertures into channels parallel to [101]. The minimum free diameter of the 6T+2O aperture is about 2.5×4.8 Å, based on an O radius of 1.35 Å. The corresponding value for the 8T aperture is 1.8×4.2 Å. However this aperture is constricted at the centre and is probably better described as comprising two adjacent minimum free diameters, each about 2.1×2.1 Å. It is clear that the cesium ions, with a diameter of at least 3.5 Å, will not be free to migrate along the channels.

Ball-and-stick models of the two types of 8-ring apertures are presented in Fig. 3, showing the the anisotropic displacement ellipsoids. Whereas the oxygen atoms forming the TiO_6 octahedra, O(2), O(4) and O(7), show only moderate anisotropy, the oxygens involved in Si-O-Si linkages are highly anisotropic, particularly those associated with the $\text{Si}(1)\text{O}_7$ group, O(3), O(5) and O(8). The principal displacement axes for these oxygens are almost in the plane of projection in Fig. 3. The orientation of the ellipsoids is suggestive of cooperative rotation of the Si(1)-centred tetrahedra about the apical Si(1)-O(4) bonds that form the Si-O-Ti linkages.

The short Cs-Cs interatomic distance of 3.76 Å occurs across the 8-ring aperture shown in Fig. 3(a), comprising 6 tetrahedra and two octahedra. The cesium cations are shielded in the plane of the aperture by the rectangle of four oxygens, $2 \times [\text{O}(2) + \text{O}(7)]$, which form the two octahedral edges. It is interesting to note that in the cesium hollandite phase, $\text{Cs}_1.36\text{Ti}_8\text{O}_{16}$, pairs of cesium ions along the hollandite tunnels are also shielded by four oxygens, and the Cs-Cs separation of 3.72 Å (10) is very close to the short Cs-Cs distance in $\text{Cs}_2\text{TiSi}_6\text{O}_{15}$. In the cesium hollandite the four oxygens form a square planar arrangement rather than a rectangle, but the cross-section area defined by the four anion positions is about the same in both compounds. In $\text{Cs}_2\text{TiSi}_6\text{O}_{15}$, the longer Cs-Cs separation of 4.90 Å occurs across the 8-ring aperture comprising 8 tetrahedral edges. As seen in Fig. 3(b) the main shielding of the cesium cations is by only two oxygens in this case. The short Cs-Cs distances of 3.72 and 3.76 Å are to be compared to a separation between cesium atoms in the bcc metal of 5.25 Å (11).

The interatomic distances and angles for the framework polyhedra are given in Table 4. The TiO_6 octahedron shows only slight departures from ideal geometry. The three independent Ti-O distances are identical, at 1.939(4) Å and the O-Ti-O angles range from 86.7(2) to 93.3(2)°. The mean Ti-O distance is identical to that in benitoite, $\text{BaTiSi}_3\text{O}_9$, which also comprises a framework of isolated TiO_6

octahedra sharing all corners with SiO_4 tetrahedra (12). The three SiO_4 tetrahedra are also quite regular, with Si-O distances in the range 1.580(1) to 1.638(5) Å, and O-Si-O angles in the range 104.5(3) to 112.9(2)°. The average Si(1)-O, Si(2)-O and Si(3)-O distances are 1.594, 1.610 and 1.603 Å. The latter two distances agree with reported mean Si-O distances in zeolites with ordering of silicon and aluminium (13, 14). The shorter mean Si(1)-O distance involves those oxygens that have the largest anisotropic displacement parameters, so the actual Si-O distances will be longer than obtained in the refinement. The cesium ion has 10 closest oxygen neighbours, with Cs-O distances in the range 3.030(5) to 3.608(4) Å and a mean Cs-O value of 3.336 Å. This is of the order of 0.2 Å longer than the mean Cs-O distance in cesium hollandite where the cesium is eight coordinated (10), but shorter than the mean Cs-O distance of 3.48 Å in pollucite (15), in which the cesium is twelve coordinated.

COMPARISON WITH OTHER STRUCTURES AND CONCLUSIONS

The structure of $\text{Cs}_2\text{TiSi}_6\text{O}_{15}$ represents a new type of microporous titanosilicate framework structure. The ordering of titanium atoms into isolated, undistorted octahedra so that there are only Si-O-Si and Ti-O-Si linkages in the framework is relatively unusual. This situation also occurs in the mineral benitoite, $\text{BaTiSi}_3\text{O}_9$ (12). However reported titanosilicates containing TiO_6 octahedra generally have higher Ti/Si ratios and involve Ti-O-Ti linkages, which form octahedral clusters as in $\text{Na}_2\text{Ti}_2\text{O}_3\text{SiO}_4\cdot 2\text{H}_2\text{O}$ (16) and $\text{Cs}_3\text{HTi}_4\text{O}_4(\text{SiO}_4)_3\cdot 4\text{H}_2\text{O}$ (17) or linear chains as ETS-10 (Engelhard Corporation titanosilicate) (18).

The other known cesium titanosilicate structure is that of $\text{CsTiSi}_2\text{O}_6\cdot 5$ (6) which differs significantly from that for $\text{Cs}_2\text{TiSi}_6\text{O}_{15}$ in having the titanium atoms disordered over the tetrahedral sites in a pollucite type framework. Relative to pollucite, $\text{CsAlSi}_2\text{O}_6$, there are extra oxygen atoms in the unit cell and Ti-EXAF studies indicate that these are coordinated to titanium so that the tetrahedral coordination is modified locally to 5-coordination (6). Five coordinated titanium occurs in layered titanosilicates such as the mineral fresnoite, $\text{Ba}_2\text{TiSi}_2\text{O}_8$ (19) and $\text{Na}_4\text{Ti}_2\text{Si}_8\text{O}_{22}\cdot 4\text{H}_2\text{O}$ (20). In these compounds the titanium has square pyramidal coordination with a very short apical bond typical of the titanyl group.

Work in progress indicates that $\text{Cs}_2\text{TiSi}_6\text{O}_{15}$ has a high durability towards leaching. It thus has potential for containment of cesium selectively adsorbed onto titanosilicate ion exchangers from sodium-rich radioactive wastes.

ACKNOWLEDGEMENTS

We appreciate help from (???) Bob with the synthesis method, and from Colin McRae with the microprobe analyses.

REFERENCES

- (1) S.M. Kuznicki, US Patent No. 4567029 (1989).
- (2) D.M. Chapman and A.L. Roe, *Zeolites*, 10, 730 (1990).
- (3) M. Taramasso, G. Perego and B. Notari, US Patent No. 4410501 (1983).
- (4) R.G. Anthony, C.V. Phillip and R.G. Dosch, *Waste Management*, 13, 503 (1993).
- (5) M.L. Balmer and B.C. Bunker, *Inorganic Ion Exchange Evaluation and Design - Silicotitanate Waste Form Conversion*. PNL-10460, March 1995.
- (6) M.L. Balmer, Q. Huang, W. Wong-Ng, R.S. Roth and A. Santoro, *J. Solid State Chem.*, submitted (1996).
- (7) K. Yanagisawa, <. Nishioka and N. Yamasaki, *J. Nucl. Sci. & Techn.*, 24, 51 (1987).
- (8) G.M. Sheldrick, *SHELX 76, Program for Crystal Structure Determination*, University of Cambridge (1976).
- (9) G.M. Sheldrick, *SHELXL93, Program for the Refinement of Crystal Structures*, University of Gottingen, Germany (1993).
- (10) R.W. Cheary, *Acta Crystallogr.*, B47, 325 (1991).
- (11) C.S. Barrett, *Acta Crystallogr.*, 9, 671 (1956).
- (12) K. Fischer, *Z. Kristallogr.*, 129, 222 (1969)
- (13) E. Galli, *Acta Crystallogr.*, B32, 1623 (1976).
- (14) I.S. Kerr and D.J. Williams, *Acta Crystallogr.*, B25, 1183 (1969).
- (15) R.E. Newnham, *Am. Mineralogist*, 52, 1515 (1967).
- (16) D.M. Poojary, R.A. Cahill and A. Clearfield, *Chem. Mater.*, 6, 2364 (1994).
- (17) W.T. Harrison, T.E. Gier, E. Thurman, and G.D. Stucky, *Zeolites*, 15, 408 (1995).

(18) M.W. Anderson, O. Terasaki, T. Ohsuna, A. Philippou, S.P. MacKay, A. Ferreira, J. Rocha and S. Lidin, *Nature*, 367, 347 (1994).

(19) S.A. Markgraf, A. Halliyal, A.S. Bhalla, R.E. Newnham and C.T. Prewitt, *Ferroelectrics*, 62, 17 (1985).

(20) M.A. Roberts, G. Sankar, J.M. Thomas, R.H. Jones, H. Du, J. Chen, W. Pang and R. Xu, *Nature*, 381, 401 (1996).

FIGURE CAPTIONS

Fig. 1. Polyhedral representation of the structure of $\text{Cs}_2\text{TiSi}_6\text{O}_{15}$, projected along the b axis. Filled circles represent cesium ions.

Fig. 2. (101) slice of the structure of $\text{Cs}_2\text{TiSi}_6\text{O}_{15}$, viewed along [101]. Filled circles represent cesium ions on either side of the polyhedral layer.

Fig. 3. Atom connectivity in the 8-membered rings formed by (a) 6 tetrahedra and 2 octahedra and (b) 8 tetrahedra. Anisotropic displacement ellipsoids (50% probability) are shown.

TABLE 1
Details of X-Ray Data Collection and Refinement

Formula mass	721.7
Space group	C2/c
a, Å	13.386(5)
b, Å	7.423(3)
c, Å	15.134(5)
β, deg.	107.71(3)
V, Å ³	1432.5
Z	4
Radiation	Mo Kα, λ = 0.7107 Å
Linear absorption coefficient, mm ⁻¹	6.30
Absorption correction	Analytical, using crystal faces (ref. 8)
Transmission factors	0.244 to 0.551
Calculated density, Mg m ⁻³	3.35
Crystal size, mm	0.24 x 0.24 x 0.10
Data scan type	θ - 2θ
Scan width, deg.	(2.4 + Δ2θ)
2θ scan range, deg.	2 - 30
No. reflections measured	1975
No. unique reflections	1874
R _{int}	0.034
Refinement on F ²	
wR(F ²), all reflections	0.13
R(F), all reflections	0.039
Extinction coefficient	0.0022(3), (ref. 9)
Δρ _{max} , e Å ⁻³	1.46
Δρ _{min} , e Å ⁻³	-1.73

TABLE 2
Fractional atomic coordinates and equivalent
isotropic displacement parameters (\AA^2)

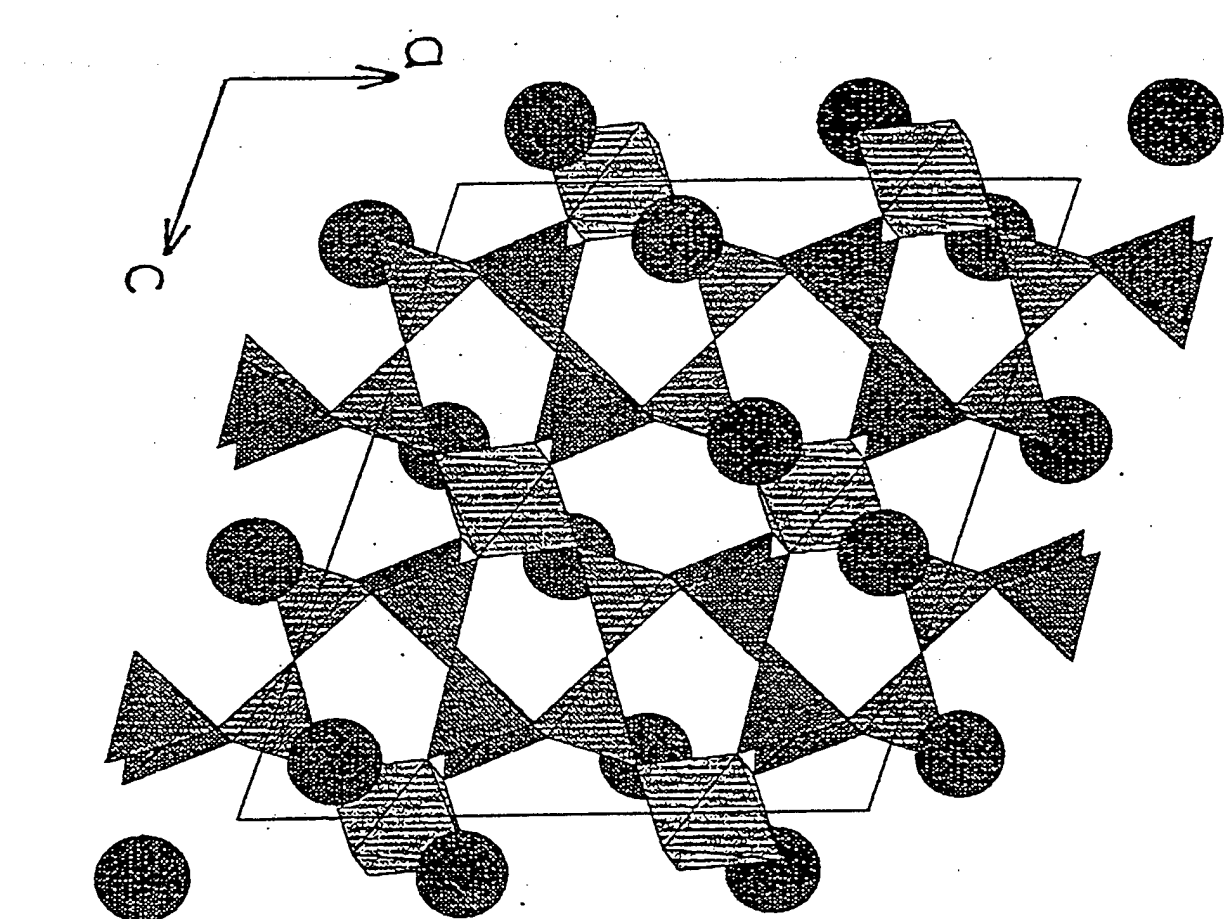
Atom	x	y	z	Ueq
Cs	0.11728(3)	0.25839(5)	0.40996(3)	0.0330(2)
Ti	1/4	1/4	0	0.0143(3)
Si(1)	0.0028(1)	0.2682(2)	0.6466(1)	0.0141(3)
Si(2)	0.1554(1)	0.0399(2)	0.1446(1)	0.0231(3)
Si(3)	0.1752(1)	0.4287(2)	0.1663(1)	0.0229(3)
O(1)	0.1189(3)	0.2353(6)	0.1722(3)	0.034(1)
O(2)	0.1973(3)	0.0526(5)	0.0568(2)	0.0233(7)
O(3)	0	0.254(1)	3/4	0.079(4)
O(4)	0.3915(3)	0.1910(7)	0.0750(3)	0.0324(8)
O(5)	0.4483(3)	0.4167(8)	0.3768(4)	0.059(2)
O(6)	0.2531(3)	0.4604(9)	0.2686(3)	0.051(1)
O(7)	0.2359(3)	0.4231(5)	0.0914(3)	0.0311(8)
O(8)	0.4169(4)	0.0732(9)	0.3576(5)	0.079(2)

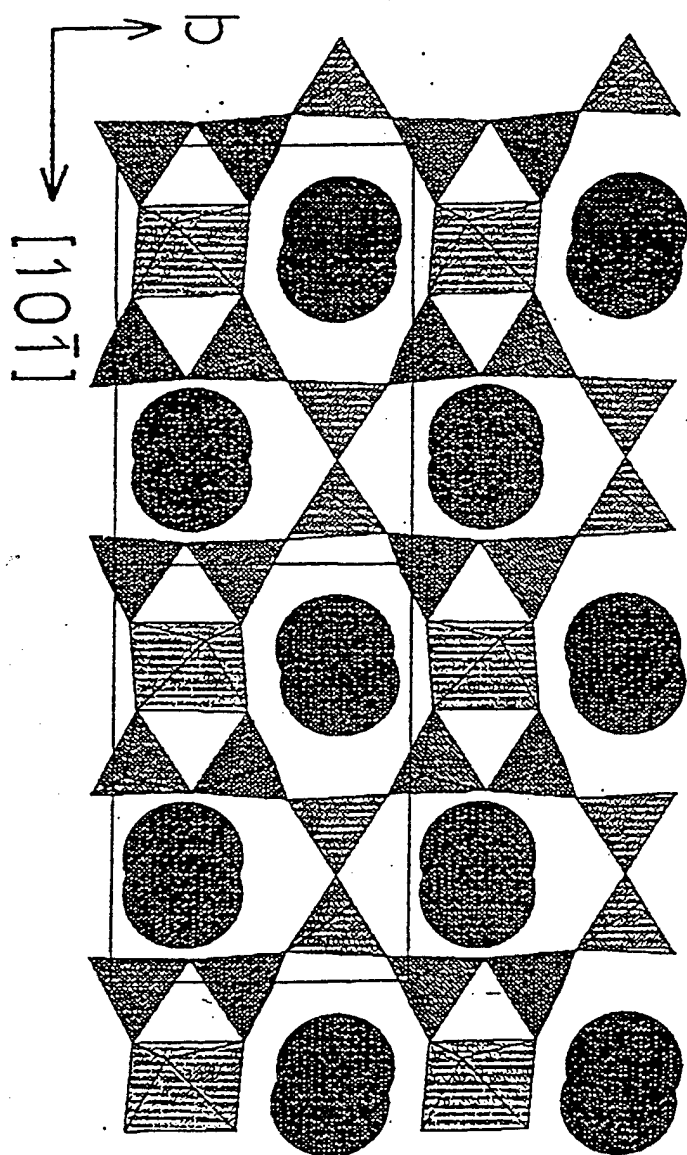
TABLE 3
Anisotropic Displacement Parameters (\AA^2)

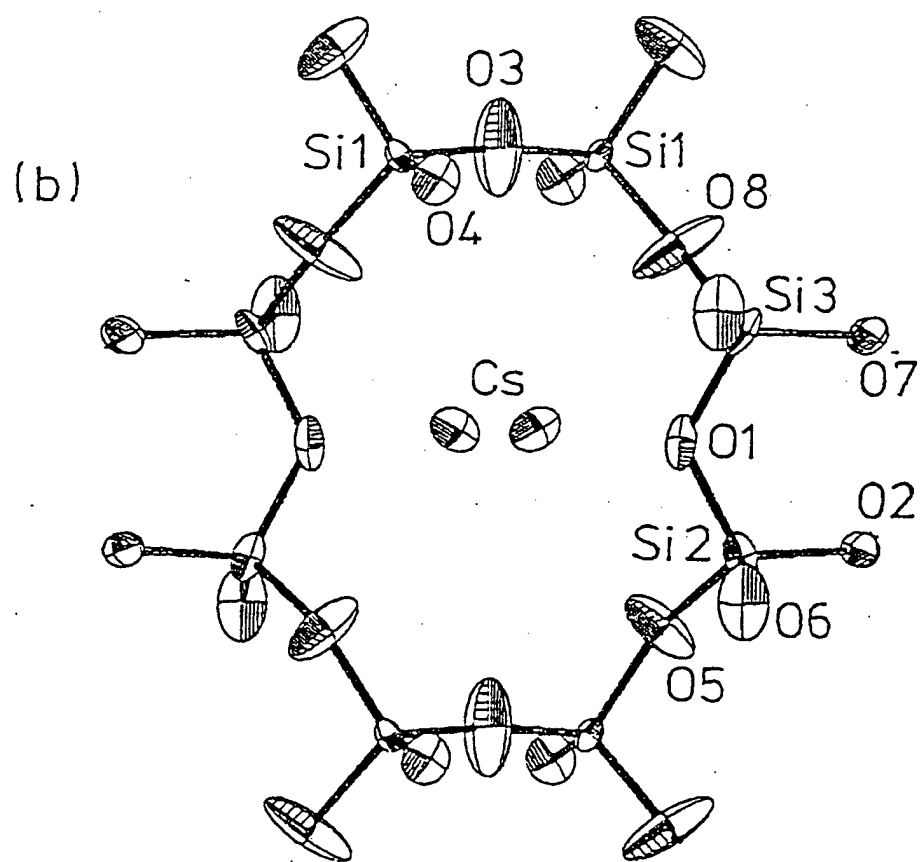
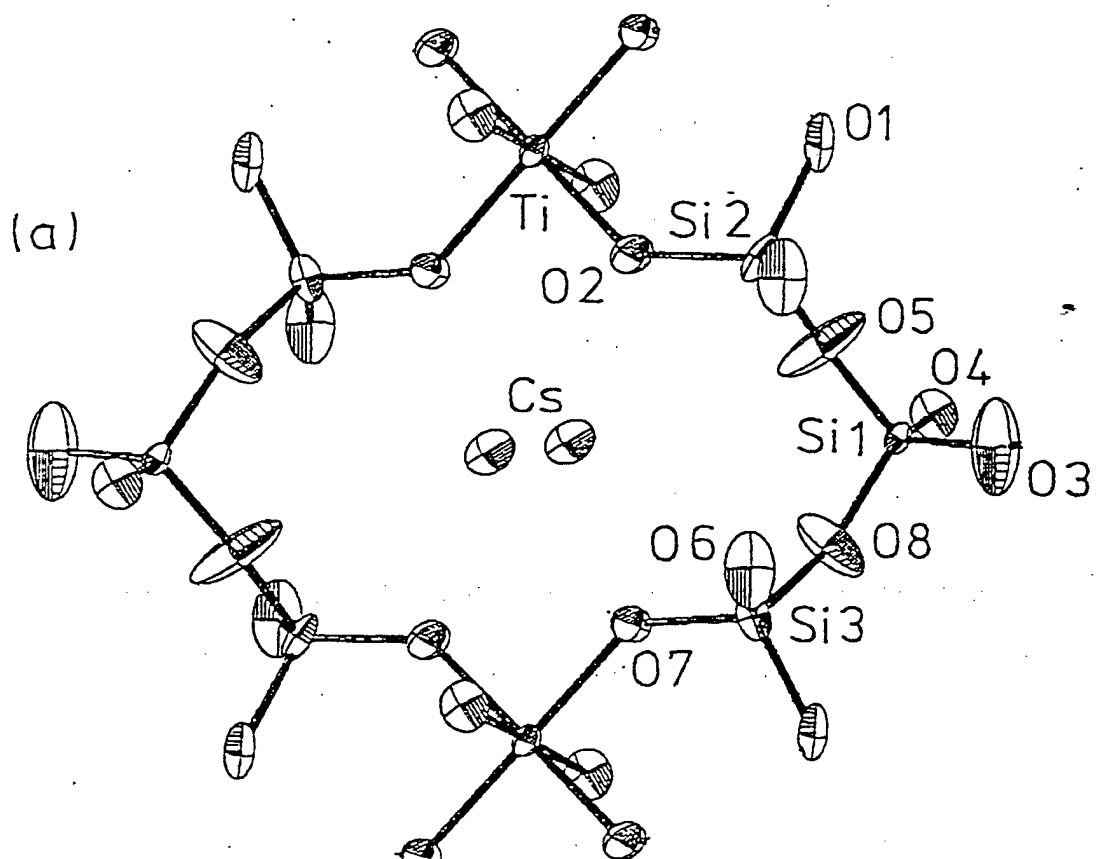
Atom	U11	U22	U33	U23	U13	U12
Cs	0.0179(2)	0.0341(3)	0.0417(3)	0.0100(1)	0.0011(2)	-.0001(1)
Ti	0.0142(5)	0.0177(5)	0.0110(4)	-.0038(3)	0.0036(4)	0.0008(3)
Si(1)	0.0106(5)	0.0181(5)	0.0135(5)	0.0013(4)	0.0033(4)	-.0039(4)
Si(2)	0.0130(5)	0.0390(8)	0.0151(5)	0.0063(5)	0.0011(4)	0.0001(3)
Si(3)	0.0134(5)	0.0365(7)	0.0159(5)	-.0126(5)	0.0003(4)	0.0075(5)
O(1)	0.022(2)	0.056(3)	0.029(2)	-.008(2)	0.015(2)	-.004(2)
O(2)	0.031(2)	0.022(2)	0.016(1)	-.002(1)	0.007(1)	-.003(1)
O(3)	0.048(5)	0.17(1)	0.026(4)	0	0.014(4)	0
O(4)	0.017(2)	0.043(2)	0.030(2)	0.005(2)	-.003(1)	0.001(1)
O(5)	0.022(2)	0.066(3)	0.073(3)	-.041(3)	-.008(2)	0.015(2)
O(6)	0.028(2)	0.101(4)	0.019(2)	-.016(2)	-.002(2)	-.013(2)
O(7)	0.047(2)	0.024(2)	0.027(2)	-.009(1)	0.019(2)	-.002(2)
O(8)	0.037(3)	0.072(4)	0.099(5)	0.057(4)	-.022(3)	-.034(3)

TABLE 4
Selected Interatomic Distances (Å) and Angles (°)

Ti-O(7) (x2)	1.939(3)	180	91.2(2)	93.3(2)
			88.8(2)	86.7(2)
Ti-O(4) (x2)	1.939(4)	91.2(2)	180	90.4(2)
		88.8(2)		89.6(2)
Ti-O(2) (x2)	1.938(3)	93.3(2)	90.4(2)	180
		86.7(3)	89.6(2)	
		O(7)	O(4)	O(2)
Si(1)-O(3)	1.580(1)			
Si(1)-O(4)	1.582(4)	112.9(2)		
Si(1)-O(5)	1.605(5)	107.2(4)	111.9(2)	
Si(1)-O(8)	1.609(5)	107.9(4)	109.5(3)	107.2(4)
		O(3)	O(4)	O(5)
Si(2)-O(2)	1.594(4)			
Si(2)-O(6)	1.610(4)	109.2(2)		
Si(2)-O(5)	1.613(5)	111.4(3)	110.5(3)	
Si(2)-O(1)	1.625(4)	111.8(2)	109.3(3)	104.5(3)
		O(2)	O(6)	O(5)
Si(3)-O(8)	1.589(5)			
Si(3)-O(7)	1.583(4)	112.7(4)		
Si(3)-O(6)	1.600(4)	110.7(3)	111.8(2)	
Si(3)-O(1)	1.638(5)	105.4(3)	111.2(2)	105.4(3)
		O(8)	O(7)	O(6)
-----	-----	-----	-----	-----
Cs-O(1)	3.030(5)	Cs-O(5)	3.336(6)	
Cs-O(2)	3.156(3)	Cs-O(8)	3.459(7)	
Cs-O(7)	3.173(4)	Cs-O(6)	3.536(5)	
Cs-O(4)	3.224(5)	Cs-O(7)	3.607(4)	
Cs-O(2)	3.232(4)	Cs-O(1)	3.608(4)	







Ti XAS of a novel Cs-Ti-silicate

NJ Hess*, ML Balmer, BC Bunker
Pacific Northwest National Laboratory,
Richland WA 99352

and

SD Conradson
Los Alamos National Laboratory
Los Alamos NM 87545

Abstract.

Ti XANES and EXAFS were performed to determine the coordination environment of Ti in several Ti oxide standards with known structures and two unknowns with $\text{CsTiSi}_2\text{O}_{6.5}$ composition, one amorphous and one fully crystalline. Analysis of both the XANES and EXAFS data of the unknowns indicate that Ti^{4+} is 5-fold coordinate in $\text{CsTiSi}_2\text{O}_{6.5}$ and that the site is highly distorted. Plots of intensity versus the energy of a Ti pre-edge feature result in the separation of 6-, 5-, and 4-fold coordinate Ti into three distinct regions. EXAFS and XANES data show that the Ti coordination environment for the amorphous and crystalline $\text{CsTiSi}_2\text{O}_{6.5}$ samples is the same indicating that the Ti coordination environment forms early in the crystallization process. Preliminary measurements at the Cs K-edge EXAFS on the same samples shows that the Cs coordination environment is different for the amorphous and the crystalline $\text{CsTiSi}_2\text{O}_{6.5}$ samples suggesting that the Cs coordination environment forms late in the crystallization process.

INTRODUCTION.

Crystalline Silicotitanates (CSTs) have been proposed as ion exchange materials for the removal of Cs and Sr from high level nuclear waste streams (1). Currently, Cs and Sr are released from the loaded traditional ion exchange resins by elution and then incorporated into solid waste forms. Reprocessing by elution is not possible with CSTs; however, another strategy is to directly incorporate the loaded CST into a solid waste form, for example, borosilicate glass logs, by melting. In addition, recent studies (2) have demonstrated that some cesium silicotitanates can be directly transformed to a crystalline material isostructural with pollucite ($\text{CsAlSi}_2\text{O}_6$) at temperatures well below those required for formation of borosilicate glass. The Ti-substituted pollucite, $\text{CsTiSi}_2\text{O}_{6.5}$, has leach rates that lower than that for the borosilicate glass, generates lower volumes of high level waste, and due to the low processing temperatures, the Cs losses due to volatilization during processing are extremely low. This application and the potential use of other silicotitanate zeolites as catalytic materials has spurred interest in determining the coordination environment of Ti in these novel materials.

X-ray Absorption Spectroscopy experiments were performed to determine the oxidation state and coordination environment of Ti^{4+} where it is substituted for Al^{3+} in the cesium aluminosilicate pollucite, $\text{CsAlSi}_2\text{O}_6$. In pollucite, both Al and Si occupy tetrahedral sites and the tetrahedra share apexes to form an open three dimensional network. The cesium atoms occupy the largest cavities in the network. The substitution of Ti^{4+} for Al^{3+} requires some mechanism for charge compensation, perhaps the presence

additional oxygen as suggested by neutron powder diffraction results (3). Recently, questions of Ti valence and coordination in zeolitic materials have been addressed using the analysis of the XANES and EXAFS spectra (4-9). Some researchers have reported some difficulty in determination of Ti coordination number (4,8,10). In this work, several Ti standards, a Cs standard and two $\text{CsTiSi}_2\text{O}_{6.5}$ samples prepared with different heat treatments were analyzed. The intensity and energy of a pre-edge feature in the Ti-XANES spectra allowed separation of the 6-, 5-, and 4-fold coordinate Ti samples into distinct regions. These results were supported by analysis of the EXAFS data once the EXAFS spectra had been corrected for self-absorption effects.

Data Collection.

The analyzed samples included standards: TiO_2 - anatase and rutile, $\text{BaTiSi}_3\text{O}_9$, $\text{NaTiSi}_4\text{O}_{11}$, ETS-4, $\text{Na}_2\text{TiSiO}_5$, $\text{K}_2\text{Ti}_2\text{O}_5$, Ba_2TiO_4 , $\text{Ba}_2\text{TiSi}_2\text{O}_8$, $\text{CsAlSi}_2\text{O}_6$ - pollucite, and CsAlTiSiO_4 , and two 'unknowns' of $\text{CsTiSi}_2\text{O}_{6.5}$ synthesized at PNNL. The structure and the Ti coordination environment of the standards have been reported in the literature. However for $\text{K}_2\text{Ti}_2\text{O}_5$ there is a discrepancy in the reported metrical parameters and what is calculated based on the space group, lattice dimensions and fractional coordinates for this structure. Based on the metrical parameters, the Ti is reported as occupying a trigonal bipyramidal structure (11,12). Based on the space group and fractional coordinates, Ti in $\text{K}_2\text{Ti}_2\text{O}_5$ resides in a severely distorted square-pyramidal polygon. The square pyramidal coordination environment is consistent with the recent structure refinement of $\text{K}_2\text{Ti}_2\text{O}_5$ using the results from Raman spectroscopy and

powder diffraction (13). The microporous silicate, ETS-4 (9), was chosen as a standard because of the occurrence of Ti in three dimensional silica network, an environment that is thought to be analogous to the Ti environment in the $\text{CsTiSi}_2\text{O}_{6.5}$. The structure of ETS-4 is thought to be similar to the zeolite, Ti- β , and has only been determined by XAS analysis (18). The 'unknown', $\text{CsTiSi}_2\text{O}_{6.5}$ A, was sintered at 700 C and is amorphous using x-ray powder diffraction while, $\text{CsTiSi}_2\text{O}_{6.5}$ B, which was sintered at 800 C, is fully crystalline.

The XAS data were collected at the Stanford Synchrotron Radiation Laboratory during six experimental runs in a two year period 1994-1996. To allow data collection at both the Ti- edge at 6965 eV and the Cs K- edge at 36000 eV, a wiggler line endstation, beamline 4-2, using Si[220] and Si[400] crystals was selected. Additional data at the Ti K- edge was collected on a bending magnet line, beamline 2-3, using Si[220] crystals. Data were collected in fluorescence using either a 13-element Ge array detector or, in later experiments, a Lytle detector. In both arrangements the beam path was flooded with He to reduce the intensity attenuation of the low energy x-rays by air at the Ti K- edge . To maximize flux the spectra were collected with the two monochrometer crystals fully tuned and harmonic rejection at Ti K- edge was accomplished using critical angle reflection off of a Rh-coated mirror. No method of harmonic rejection was employed at the high energy of the Cs K- edge . All data were collected at liquid nitrogen temperatures.

All the samples were analyzed in powder form. The $\text{Na}_2\text{TiSiO}_5$ and $\text{K}_2\text{Ti}_2\text{O}_5$ samples were heated treated at 400 C for 12 hours prior to analysis to drive off water. The amount of powders required to result in an absorption unit of one was calculated, weighed-out, and thoroughly mixed with small amount of glucose using a mortar and pestle. The resulting mixture was pressed into a slot of a sample holder using a hydraulic press. The sample holder was then sealed with kapton tape mounted on the cold finger of a liquid nitrogen cryostat. The cryostat was placed in the beam path so that the plane of the samples was at 45 degrees to the incident beam. A titanium metal foil was also mounted on the sample holder and was used to calibrate the x-ray energy periodically during the fluorescence measurements. Data at the Cs K-edge data were internally calibrated by setting the inflection point to 36005.0 eV. In almost all cases, multiple scans were collected and averaged to increase the signal to noise ratio.

Data Analysis.

The XAS spectra were split into two regions for data analysis. The XANES, or pre-edge region, extending from approximately 50 eV below the absorption edge to 100 eV above the edge, and the EXAFS region, at energies above the absorption edge. The XANES region generally contains direct information about the oxidation state of the absorber. In the case of Ti the XANES region is especially rich and can be used to extract information on bond length and site symmetry (14,15). However, much of the interpretation of the XANES data is based on an empirical association of features that are observed in well-characterized standards to similar features observed in unknowns.

The data in the EXAFS region is used to extract quantitative information on the number and bond length of coordinating atoms in each coordination sphere. In addition, the chemical identity of the coordinating atoms can be determined. Unlike XANES data analysis, there is a complete theoretical understanding of the EXAFS features (16,17).

Background subtraction and normalization were performed following standard practice described briefly below. A linear polynomial is fit through the pre-edge region and extrapolated under the absorption edge. A second polynomial is fit to the EXAFS region and extrapolated to the absorption edge. At approximately 5 to 20 eV above the edge, the extrapolated pre-edge is set to zero value and the resulting vertical difference between these two extrapolated lines is normalized to one. As a result the intensity of the EXAFS oscillations is on a per atom basis. A two or three segment, polynomial spline through the EXAFS region was determined by the minimization of the amplitude of the Fourier Transform region from 1 to 3 Å. The normalized absorption spectra was subtracted from the spline and weighted by k^3 .

Ti-XANES.

The Ti-XANES region was fit using a commercially available fitting package GRAMS386. The pre-edge region from 4950 to 4990 eV was fit using a linear combination of Gaussian curves. For anatase, which displayed the most complex XANES spectra, eight Gaussian curves were required. Most of the other XANES spectra were significantly simpler and required fewer Gaussian components. To

represent the Ti K-edge jump a single Gaussian curve was fixed at 4990 eV with an amplitude of 1 ± 0.05 for all spectra. As found by Waychunas (14), the resulting Gaussian curves could be grouped into two regions; on the low energy tail of the absorption edge and on the edge itself. The frequency and intensity of the Gaussian features have been correlated with the symmetry, coordination number and bond length of the first coordination sphere. No analysis of the Cs XANES was performed because this region is relatively featureless.

EXAFS.

The Ti and Cs EXAFS data were simulated and fit with parameterized scattering amplitudes calculated using the FEFF6.0 code developed by Professor John Rehr and co-workers at the University of Washington (16,17). Several model compounds were created using the FEFF6.0 code and crystallographic data from the literature. From these model compounds, individual scattering paths were parameterized and used to fit the several of the standards and the two unknowns. The fits were made to the unfiltered data. Each fit was evaluated by several methods. First, Fourier transforms were performed over the fitted region to see if results actually fitted features apparent in r-space. In addition each scattering path was compared to the residual in k-space to be sure there was frequency and node matching. A third method to evaluate the quality of the fit was to Fourier Transform each scattering path and compare it to the residual. A fourth method was to perform the fit over several k-ranges to determine whether some features were not created by the choice of Fourier Transform range.

For each shell there are five parameters used in the fit: ΔE_0 , the scale factor, the number of atoms, the distance, and sigma or the disorder. Two of these, ΔE_0 and the scale factor, are determined by fitting the filtered EXAFS of the first oxygen shell of a known reference material, in this case anatase. ΔE_0 and the scale factor are fixed at these values for the remaining samples. The other three parameters, the number of atoms, the distance, and sigma or the disorder are allowed to vary for each shell.

Ti EXAFS:

The Ti EXAFS region was fit over the data range from $k = 2.5$ to 10 \AA^{-1} except for the data for $\text{K}_2\text{Ti}_2\text{O}_5$ which was fit over the data range from $k = 2.5$ to 9 \AA^{-1} . The change in fitting range was necessary because the EXAFS of this sample was perturbed by a large monochromator glitch at approximately $k = 9.1 \text{ \AA}^{-1}$. The Ti K-edge EXAFS over the two fitting ranges for the six samples are shown in Figure 1. Qualitatively, the EXAFS of all six samples show a general similarity in the periodicity and the node placements of the first two oscillations. At higher k values, the similarity of the EXAFS decreases. In addition the signal-to-noise ratio decreases. The amplitude of the anatase EXAFS is appreciably greater than the other samples, especially at high k .

The Fourier Transforms of the EXAFS data over the fitted k -range are presented in Figure 2. The Fourier Transform of the EXAFS is commonly called the radial distribution function, or RDF. The RDF gives a more immediate "physical" picture of

the EXAFS results because it represents the radial spatial distribution and density of neighboring atoms from the point of reference of the absorbing atom. The first peak in the RDF represents the scattering off Ti nearest neighbor atoms, in this case oxygen. The RDF plot shown in Figure 2 has not been corrected for the phase shift and the apparent distances are generally shorter by 0.5 to 1.0 Å than those distances determined by fitting the data. At the first level of approximation, a large amplitude can reflect either a large number of atoms or atoms with high atomic number. The amplitude can be diminished in intensity by both static and thermal contributions to the disorder in atomic positions.

Because the focus of this study is on the immediate coordination environment around the Ti atoms, back Fourier transforms were performed around the oxygen shell to remove contributions to the EXAFS from the more distant shells. The amplitude and the real part of the back Fourier transforms are plotted in Figure 3. The oxygen EXAFS oscillation at anatase exhibits the largest amplitude, in addition the amplitude is uniform across the k-range indicating there is minimal disorder in the oxygen positions. The microporous silicate, ETS-4, has the next largest amplitude at low k, however the amplitude decreases significantly at high k. The decrease in amplitude at k suggests that the disorder in oxygen positions is greater than that found for anatase. $\text{Na}_2\text{TiSiO}_5$ oxygen amplitude has lower amplitude at low k than both anatase and ETS-4 but the amplitude does not decrease at high k suggesting that $\text{Na}_2\text{TiSiO}_5$ has fewer oxygen nearest neighbors than anatase and ETS-4 but less disorder than ETS-4. The two

$\text{CsTiSi}_2\text{O}_{6.5}$ unknowns and the $\text{K}_2\text{Ti}_2\text{O}_5$ sample have amplitudes that are similar to $\text{Na}_2\text{TiSiO}_5$ but their amplitudes diminish dramatically at high K indicating significant disorder in the oxygen positions. Also apparent in Figure 3 is the difference in the frequency of the EXAFS oscillations. Generally, higher frequency oscillations reflect longer Ti-O bond lengths. Fits to the back Fourier transform involved a single oxygen shell based on the phase and amplitude functions extracted from FEFF calculations on anatase.

Cs EXAFS.

The EXAFS of the Cs k -edge were not analyzed in detail. The objective of the Cs EXAFS study was to determine how the Cs environment compared qualitatively to the alumino-silicate pollucite and whether the Cs environment changed between the two heat treatments for the synthesized samples. The Cs K-edge EXAFS are shown in Figure 4. Fourier Transforms performed over a k -range from $k = 4$ to 10 \AA^{-1} are shown in Figure 5. The first shell consists of scattering amplitude from 10 oxygens at bond lengths of 3.3 to 3.5 \AA . The second shell with the largest amplitude consists of scattering paths from both Si and Ti second nearest neighbors. Cs atoms at approximately 4.8 \AA dominate the contribution to the third most distant shell. There is striking similarity in the transforms of the Cs environment in $\text{CsTiSi}_2\text{O}_{6.5}\text{B}$ and the alumino-silicate pollucite $\text{CsAlSi}_2\text{O}_6$ in even the most distant shell. $\text{CsTiSi}_2\text{O}_{6.5}\text{A}$ only exhibits amplitude in the first shell.

Fitting Results.

The Ti K-edge XANES region of the samples is shown in Figure 6. Based on the energy of the absorption edge all of the compounds analyzed contain Ti^{4+} . In addition, two groups of pre-edge features can be recognized, one group centered at approximately 4970 eV and a second group on the steep slope of the absorption edge. Of these, the second feature in the first group, A2, shows significant variation in intensity and energy relative to the absorption edge from compound to compound. Changes in A2 intensity have been correlated to the amount of distortion from perfect octahedral coordination (14), and the energy of this peak has been correlated with the number of coordinating oxygens. Pre-edge features on the steep slope of the absorption edge show a strong correlation with Ti-O bond length. The curve-fitting results for anatase Ti-XANES is shown in Figure 7. The Table I lists the fitting results for peak A2 for all samples and for values found in the literature.

Table Ia. Curve-fitting results for pre-edge feature A2

sample	Intensity	Energy ^a (ev)	coordination
TiO ₂ anatase	0.20	5.50	6
TiO ₂ rutile	0.14	5.3	6.0
Na ₂ TiSiO ₅	0.68	4.2	5
K ₂ Ti ₂ O ₅	0.41	3.8	5
ETS-4	0.19	4.6	5 or 6
BaTiSi ₃ O ₉	0.13	4.7	6
Na ₂ TiSi ₄ O ₁₁	0.30	4.5	6
Ba ₂ TiSi ₂ O ₈	0.51	4.1	5.0
CsAlTiO ₄	0.83	3.4	4
CsTiSi ₂ O _{6.5} B	0.35	3.4	?
CsTiSi ₂ O _{6.5} A	0.27	3.1	?

Table Ib. Literature values for pre-edge feature A2

sample	Intensity	Energy ^a (ev)	coordination
TiO ₂ anatase ^b	0.21	5.5	6
TiO ₂ rutile ^b	0.18	5.5	6
ramsayite ^b	0.29	4.8	6
titanyl phthalocyanine ^b	0.79	4.5	5
fresnoite ^b	0.60	4.0	5
Ba ₂ TiO ₄ ^b	0.84	3.5	4
Ti(OAm) ₄ ^c	0.74	2.8	4
Ti(OPr) ₄ ^c	0.50	3.0	4
Ti(OEt) ₄ ^c	0.32	3.4	5
Ti(OBu) ₄ ^c	0.30	3.1	5.00

a. Energy relative to E₀ defined as the first inflection point of the absorption edge of Ti foil at 4965 eV.

b. Data from reference 5.

c. Data from reference 18.

The XANES fitting results listed in Table I are compared graphically in Figure 8.

Plotting the relative energy versus A2 peak intensity separates the samples into three regions. The samples with six-coordinate Ti have low A2 peak intensity and large relative energy. Samples with five-coordinate span a diagonal of the plot from low relative energy and A2 peak intensity to high relative energy and A2 peak intensity. The four-coordinate Ti samples have low relative energy and high A2 peak intensity.

The $\text{CsTiSi}_2\text{O}_{6.5}$ unknowns fall in the diagonal region representing 5-coordinate compounds.

The EXAFS fitting results are listed in Table II for the oxygen coordination shell around Ti. The calculated FEFF Ti-O scattering amplitude was multiplied by a scattering factor of 0.42 in order to generate the six oxygens required for the anatase structure.

Typically the FEFF6 code correctly calculates the scattering amplitude so that little correction is needed. A correction of this magnitude suggests that the low energy x-ray fluorescence may have been absorbed by the powder particles themselves, a process called self-absorption. Self absorption can usually be avoided by diluting the sample with a low Z matrix material and grinding the powders to a small particle size. Both techniques were employed in this work. If the scattering geometry is known and the stoichiometry of one standard is known, then self-absorption corrections can be made to the amplitude of the EXAFS oscillations following the procedure of Torger (19).

Evaluation of the fitting results to the standards where the coordination environment of

Ti is known allows one to gauge the certainty of the results determined for the unknowns and for structural situations where the fitting results are problematic. Therefor, the fitting results for the standards will be discussed in some detail before moving on to the two $\text{CsTiSi}_2\text{O}_{6.5}$ unknowns.

Table IIa EXAFS fitting results for first oxygen shell

sample	distance ^a	number ^b	sigma	r^2
TiO_2 - anatase	1.96 ± 0.01	6.0 ± 0.9	0.00 ± 0.00	0.4601
ETS-4	1.99 ± 0.01	5.7 ± 0.9	0.01 ± 0.00	0.5009
$\text{Na}_2\text{TiSiO}_5$	2.00 ± 0.01	4.8 ± 0.7	0.00 ± 0.00	0.3360
$\text{K}_2\text{Ti}_2\text{O}_5$	1.95 ± 0.02	5.3 ± 0.9	0.09, fixed	0.5301
$\text{Cs}_2\text{TiSiO}_5\text{B}$	1.93 ± 0.01	5.3 ± 0.9	0.07 ± 0.01	0.5161
$\text{Cs}_2\text{TiSiO}_5\text{A}$	1.94 ± 0.01	5.4 ± 0.9	0.06 ± 0.02	0.6652

a. Delta E_0 for Ti - O = 1.0 eV

b. Scale factor for Ti - O = 1.00

Table IIb Metrical Parameters for first oxygen shell

standard	distance		number
TiO_2 - anatase ^c	1.94		4
	1.97		2
$\text{Na}_2\text{TiSiO}_5$ ^d	1.70		1
	1.99		4
$\text{K}_2\text{Ti}_2\text{O}_5$	1.58	1.67 ^g	1
	1.65 ^e or 1.91	1.87	1
	1.99	1.99 to 2.08 ^f	3
ETS-4 ^h	1.94 ± 0.02		5.5 ± 0.5

c. from reference 20.

d. from reference 21.

e. distance published by Andersson and Wadsley (11,12).

f. distance calculated using crystallographic data in Andersson and Wadsley (11,12).

g. distances from reference 13

h. based on EXAFS from reference 18.

The fitting results for the two 6-coordinate standards, anatase and ETS-4, reveal an oxygen shell containing six oxygens at 1.95 Å. Sigma, the disorder parameter, is quite small but consistent with the minor difference between the six Ti-O bond lengths. The fitting results for anatase are in quite good agreement with the metrical parameters and the results for ETS-4 agree well with XAFS results on a similar structure, the zeolite Ti- β (18).

The fitting results for the two 5-coordinate standards, $\text{Na}_2\text{TiSiO}_5$ and $\text{K}_2\text{Ti}_2\text{O}_5$, reveal an oxygen shell containing five oxygens at 2.00 Å and 1.95 Å, respectively. As listed in Table IIb, these structures contain one Ti-O bond that is significantly shorter than the four other Ti-O bonds. Such a large difference in bond lengths generally results in a large sigma value. Surprisingly, sigma for the $\text{Na}_2\text{TiSiO}_5$ Ti-O shell has zero value. When the EXAFS oscillations for a short Ti-O bond (eg 1.70 Å) and for the longer 2.0 Å bond length are overlayed in k-space, the oscillations are nearly π out of phase over most of the fitting range. As a result, the two waves beat against each other, interfering destructively. This result suggests that the square pyramidal coordination environment may present a problematic geometry for EXAFS analysis, especially when a limited k-space range is used in the fit. The sigma value for the $\text{K}_2\text{Ti}_2\text{O}_5$ structure is quite large and is consistent with the large distribution of Ti-O bond lengths determined for this structure.

The best fits to the two $\text{CsTiSi}_2\text{O}_{6.5}$ unknowns result in five oxygens at 1.93 Å. This Ti-

O distance is consistent with the results of Pei (10) who found that compounds with 5-fold coordinate Ti had Ti-O bond distances of 1.90 Å or greater whereas 4-fold and 6-fold coordinate and Ti compounds are typified by 1.76 to 1.81 Å and 1.95 to 2.00 Å Ti-O bond lengths, respectively. The similarity of the Ti-O environments for the two $\text{CsTiSi}_2\text{O}_{6.5}$ compounds is remarkable considering that the powder XRD for these samples indicate that the $\text{CsTiSi}_2\text{O}_{6.5}\text{A}$ sample is x-ray amorphous and the $\text{CsTiSi}_2\text{O}_{6.5}\text{B}$ sample is fully crystalline. This suggests that the local Ti-O environment forms early in the crystallization sequence of these compounds. Sigma is quite large for both samples indicating that there is significant variability in the Ti-O bond lengths. A comparison of the fitted EXAFS to the back Fourier transforms is shown in Figure 9.

Conclusions.

Based of the energy of the inflection point of the Ti K-edge absorption feature, the oxidation state of Ti in the $\text{CsTiSi}_2\text{O}_{6.5}$ samples is Ti^{4+} . Analysis of the XANES spectra strongly indicate that the Ti in the two $\text{CsTiSi}_2\text{O}_{6.5}$ samples is 5-fold coordinate and this result is supported by the analysis EXAFS data. Comparison of the fitting results of the Ti standards to the metrical parameters suggests that once the EXAFS are corrected for self-absorption effects the number of oxygens can be determined. For 5-fold coordinate Ti compounds, a determination of the disorder associated with the Ti-O bond lengths in each structure may not be possible due to destructive interference of EXAFS scattering amplitudes from the short Ti-O bond distance and the longer Ti-O

bonds. However, the intensity and energy of a pre-edge feature in the XANES can be used to separate 4-, 5-, and 6-fold coordinate Ti compounds reliably.

The similarity of the Ti-O environments for the amorphous and fully crystalline $\text{CsTiSi}_2\text{O}_{6.5}$ samples suggests that the local Ti-O environment forms early in the crystallization sequence for these compounds. This results contrasts with the EXAFS result for the local Cs-O environment. Only the fully crystalline $\text{CsTiSi}_2\text{O}_{6.5}$ sample showed strong similarity to the aluminosilicate standard pollucite. This suggests that the Cs coordination environment is formed at the latest stages of crystallization, a result that could have significant impact on Cs waste form synthesis.

ACKNOWLEDGEMENTS

The authors thank Dr. Jim Dickinson, Corning Glass Corporation for providing samples of $\text{Na}_2\text{Ti}_2\text{Si}_2\text{O}_9$ and $\text{K}_2\text{Ti}_2\text{O}_5$ and Drs. Farrel Lytle and Glen Waychunas for helpful discussions on data collection and XANES analysis of Ti compounds. This work was performed at Stanford Synchrotron Radiation Laboratory which is operated by the US Department of Energy, Office of Basic Energy Sciences, Division of Chemical Sciences. Pacific Northwest National Laboratory is operated by Battelle Memorial Institute for the US Department of Energy under contract DE-AC06-76-RLO 1830.

REFERENCES.

1. R.G. Anthony, C.V. Phillip and R.G. Dosch, "Selective adsorption and ion exchange of metal cations and anions with silico-titanates and layered titanates," *Waste Management*, 13:503, 1993.
2. M.L. Balmer and B.C. Bunker, "Inorganic ion exchange evaluation and design-silicotitanate ion exchange waste conversion," Pacific Northwest National Laboratory Technical Report, PNL-10460, 1995.
3. M.L. Balmer, Q. Huang, W. Wong-Ng, A. Santoro, and B. Roth, "Neutron and X-ray diffraction study of the crystal structure of $\text{CsTiSi}_2\text{O}_{6.5}$," *Journal of Solid State Chemistry*, submitted, 1996.
4. P. Behrens, H. Felsche, S. Vetter, G. Schulz-Ekloff, N.I. Jaeger, and W. Niemann, "A XANES and EXAFS investigation of titanium silicalite," *Journal of Chemical Society, Chemical Communications*, p. 678-680, 1991.
5. T. Blasco, M.A. Camblor, A. Corma, J. Perez-Pariente, "The state of Ti in titanoaluminosiliicates isomorphous with Zeolite β ," *Journal of American Chemical Society*, 115:11806-11813, 1993.
6. G. Deo, A.M. Turek, I.E. Wachs, D.R.C. Huybrechts, and P.A. Jacobs, "Characterization of titania silicalites," *Zeolites*, 13:365-373, 1993.
7. G. Sankar, F. Rey, J.M. Thomas, G.N. Greaves, A. Corma, B.R. Dobson, and A.J. Dent, "Probing active sites in solid catalysts for the liquid-phase epoxidation of alkenes," *Journal of the Chemical Society, Chemical Communications*, p. 2279-2280, 1994.
8. E. Schultz, C. Ferrini, and R. Prins, "EXAFS and XANES on Ti-containing zeolite Y," *Japanese Journal of Applied Physics*, 32:490-492, 1993.
9. S.M. Kuznicki, K.A. Thrush, F.M. Allen, S.M. Levine, M.M. Hamil, D.T. Hayhurst, and M. Mansour, "Synthesis and adsorptive properties of titanium silicate molecular sieves," in *Synthesis of Microporous*, 1, M.L. Ocelli, ed., Van Nostrand Reinhold, New York, pp. 427, 1992.

10. S. Pei, G.E. Zajac, J.A. Kaduk, J. Faber, B.I. Boyanov, D. Duck, D. Fazzini, T.I. Morrison, and D.S. Young, "Re-investigation of titanium silicalite by X-ray absorption spectroscopy: are the novel titanium sites real?", *Catalysis Letters*, 21:33-344, 1993.
11. S. Andersson and A.D. Wadsley, "Five-coordinate Titanium in $K_2Ti_2O_5$," *Nature*, 187:499-500, 1960.
12. S. Andersson and A.D. Wadsley, "The crystal structure of $K_2Ti_2O_5$," *Acta Chemica Scandinavica*, 15:662-669, 1961.
13. F.D. Hardcastle, H. Klesnar, and C.H.F. Peden, "Structure refinement of $K_2Ti_2O_5$ by Raman spectroscopy and X-ray powder diffraction," submitted to *Journal of Solid State Chemistry*, 1996.
14. G.A. Waychunas, "Synchrotron radiation XANES spectroscopy of Ti in minerals: Effects of Ti bonding distances, Ti valence, and site geometry on absorption edge structure," *American Mineralogist*, 72:89-101, 1987.
15. G.E. Brown, Jr., G. Calas, G.A. Waychunas, and J. Petiau, "X-ray absorption spectroscopy: applications in mineralogy and geochemistry," in *Spectroscopic Methods in Mineralogy and Petrology*, vol 18, F.C. Hawthorn, ed., pp. 431-505, 1988.
16. J. Mustre de Leon, J.J Rehr, S.I. Zabinsky, and R.C. Albers, "Ab initio curved-wave x-ray absorption fine structure," *Physical Review B* 44:4146 (1991).
17. S.I. Zabinsky, J.J. Rehr, A. Ankudinov, R.C. Albers, and M.J. Eller, "Multiple scattering calculations of X-ray absorption spectra," *Physical Review B*, 1994.
18. S. Boridga, S. Coluccia, C. Lamberti, L. Marchese, A. Zecchina, F. Buffa, F. Genoni, G. Leofanti, G. Petrini, and G. Vlaic, "EXAFS study of Ti-silicalite: structure and framework Ti(IV) in the presence and absence of reactive molecules (H_2O , NH_3) and comparison with ultraviolet-visible and IR results," *Journal of Physical Chemistry*, 98:4125-4132, 1994.

19. L. Troger, D. Arvanitis, K. Baberschke, H. Michaelis, U. Grimm, and E. Zschech, "Full correction of the self-absorption in soft-fluorescence extended x-ray fine structure," *Physical Review B*, **46**:3283-3289.
20. D.H. Lindsley, "The crystal chemistry and structure of oxide minerals as exemplified by the Fe-Ti oxides," in *Oxide Minerals*, vol. 3, D. Rumble III, ed., Bookcrafters, Chelsea, pp. L1-L52, 1976.
21. H. Nyman, M. O'Keefe, and J.-O. Bovin, "Sodium titanium silicate, $\text{Na}_2\text{TiSiO}_5$," *Acta Crystallography*, **B34**:906-906, 1978.

Figure Captions.

Figure 1. Ti K-edge EXAFS. The EXAFS of the two $\text{CsTiSi}_2\text{O}_{6.5}$ unkowns are compared to the Ti standards.

Figure 2. Radial Distribution Function at Ti K-edge. Fourier transforms were calculated from 2.5 to 10 \AA^{-1} using a Gaussian window of 0.5 \AA^{-1} . Note that peak postions have not been phase corrected.

Figure 3. Back Fourier Transform of Ti-O Peak. Back Fourier transforms were calculate for the Ti-O peak centered between 0.8 to 2.1 \AA^{-1} . The real component of the Fourier transform and the amplitude are plotted.

Figure 4. Cs K-edge EXAFS. The EXAFS of the two $\text{CsTiSi}_2\text{O}_{6.5}$ unkowns are compared to the Cs standard, $\text{CsAlSi}_2\text{O}_6$ -pollucite .

Figure 5. Radial Distribution Function at Cs K-edge. Fourier transforms were calculated from 4.0 to 12 \AA^{-1} using a Gaussian window of 0.5 \AA^{-1} . Note that peak postions have not been phase corrected.

Figure 6. Ti K-edge XANES. The EXAFS of the two $\text{CsTiSi}_2\text{O}_{6.5}$ unkowns are compared to the Ti standards.

Figure 7. Gaussian Components Used in the Curve-fit of Anatase Ti-XANES. Anatase XANES from 4955 to 4990 eV was fit using a linear combination of 8 Gaussian curves. The pre-edge feature, A2, displays a systematic shift in intensity and in energy with Ti coordination number.

Figure 8. Plot of the Intensity versus Energy of Pre-edge Feature A2. Curve-fit results for the Ti standards and unkowns are compared to values found in the literature. 4-, 5-, and 6-coordinate Ti separate into distinct regions of intensity and energy.

Figure 9. Comparison of the Fit to Back-Fourier Transform for Ti-O. K-space comparison of the FEFF fitting results to the back Fourier transforms of the Ti-O shell for the two $\text{CsTiSi}_2\text{O}_{6.5}$ unkowns.

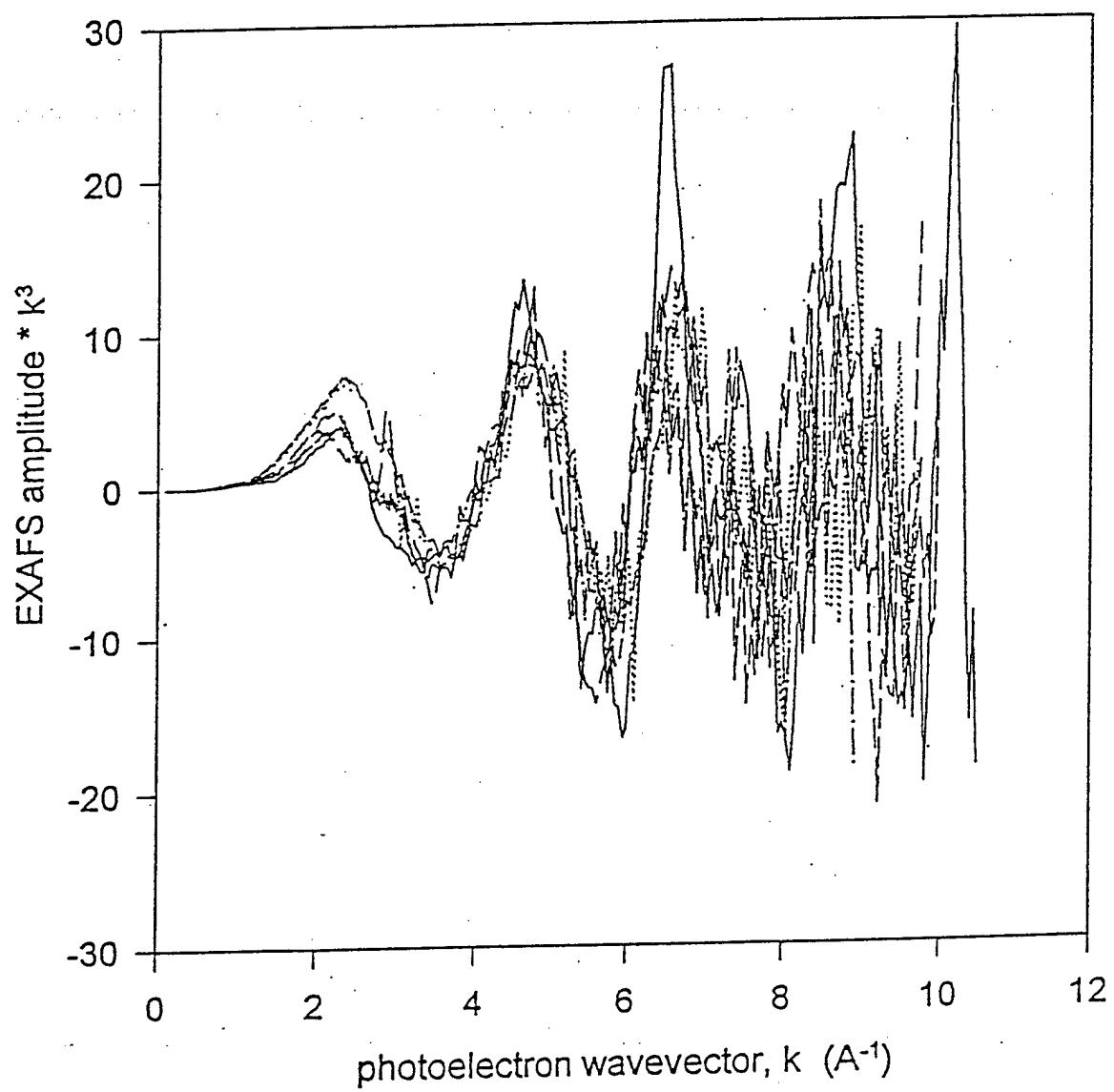


Figure 1.

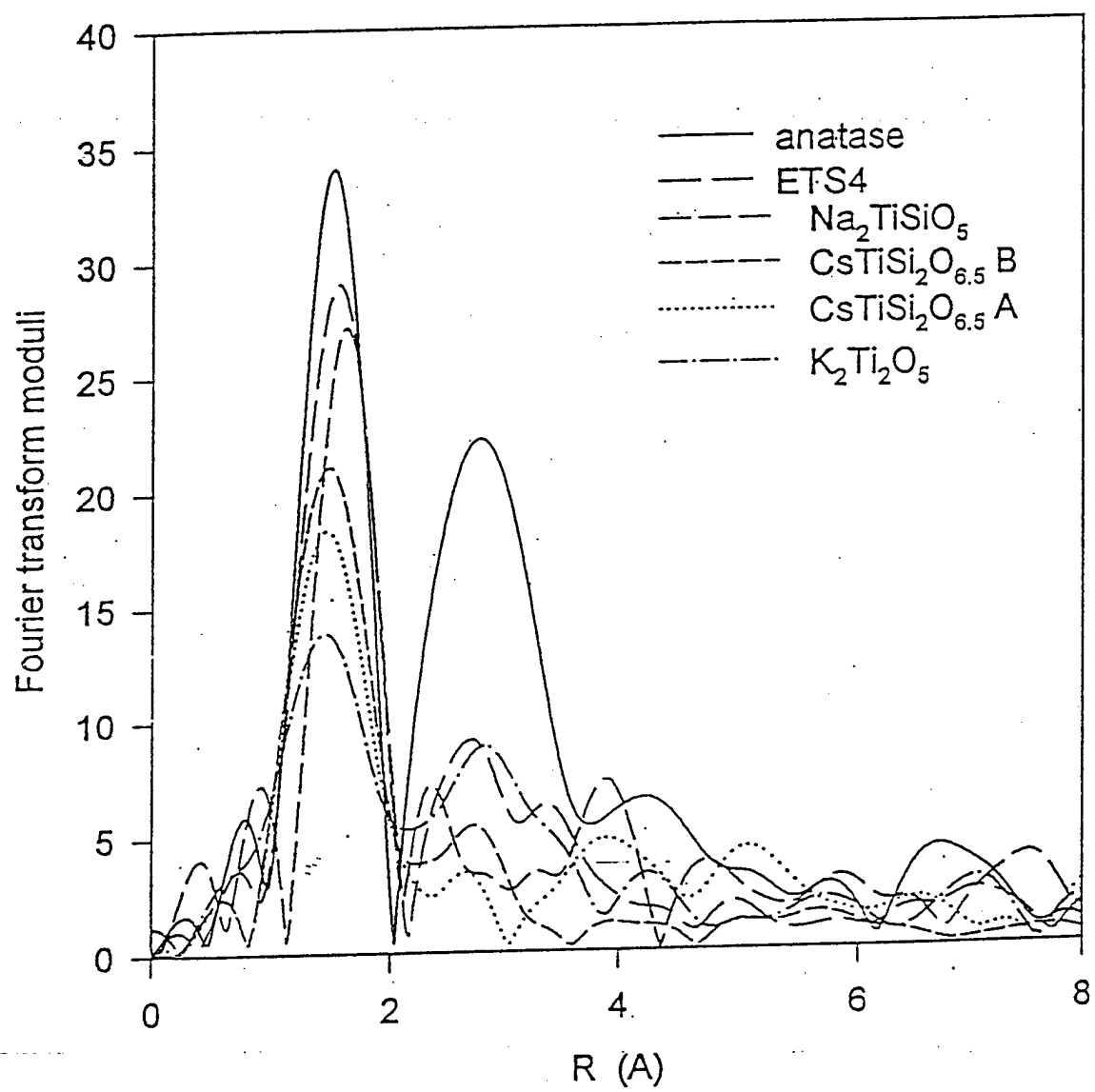


Figure 2.

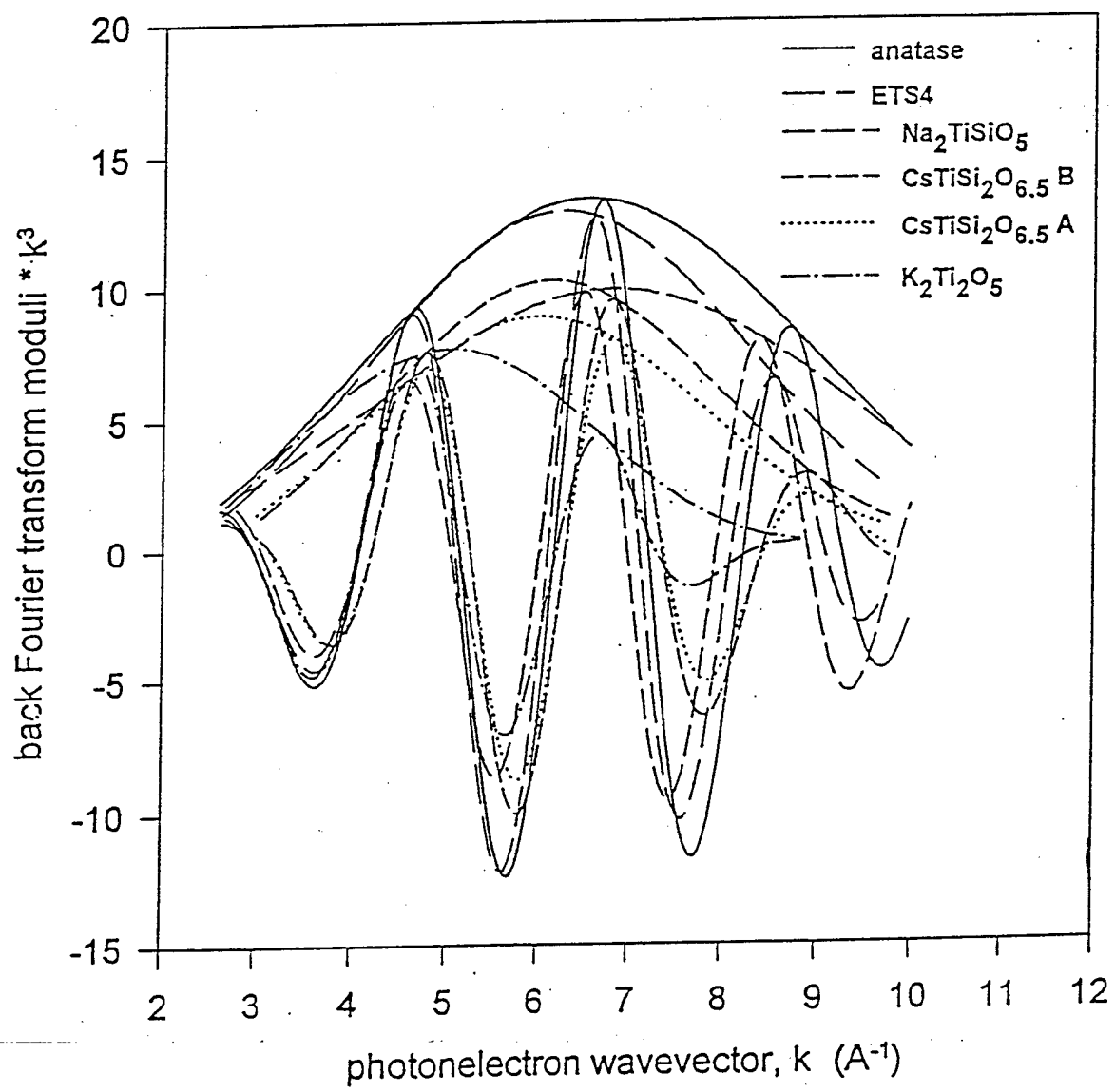


Figure 3.

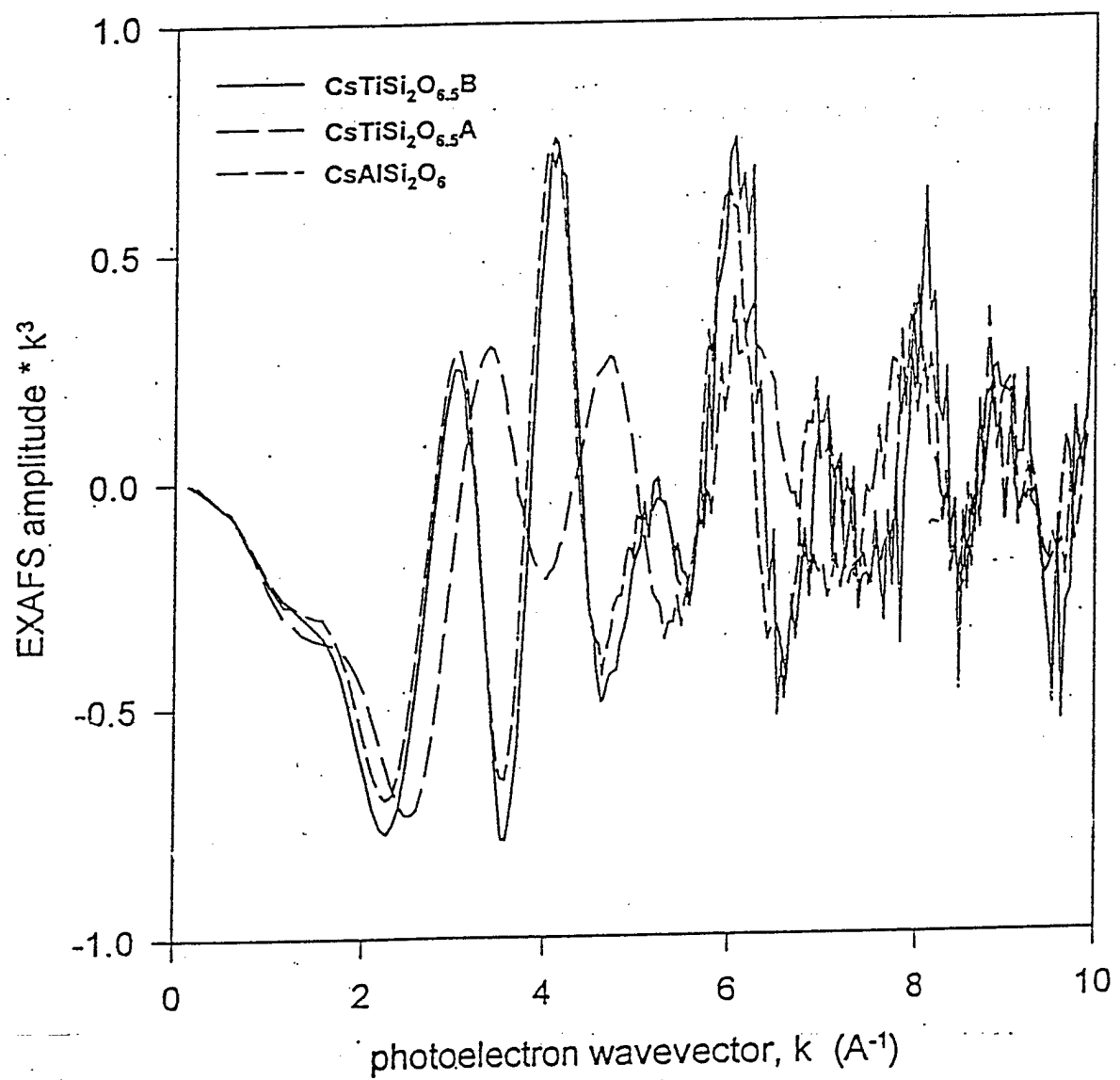


Figure 4.

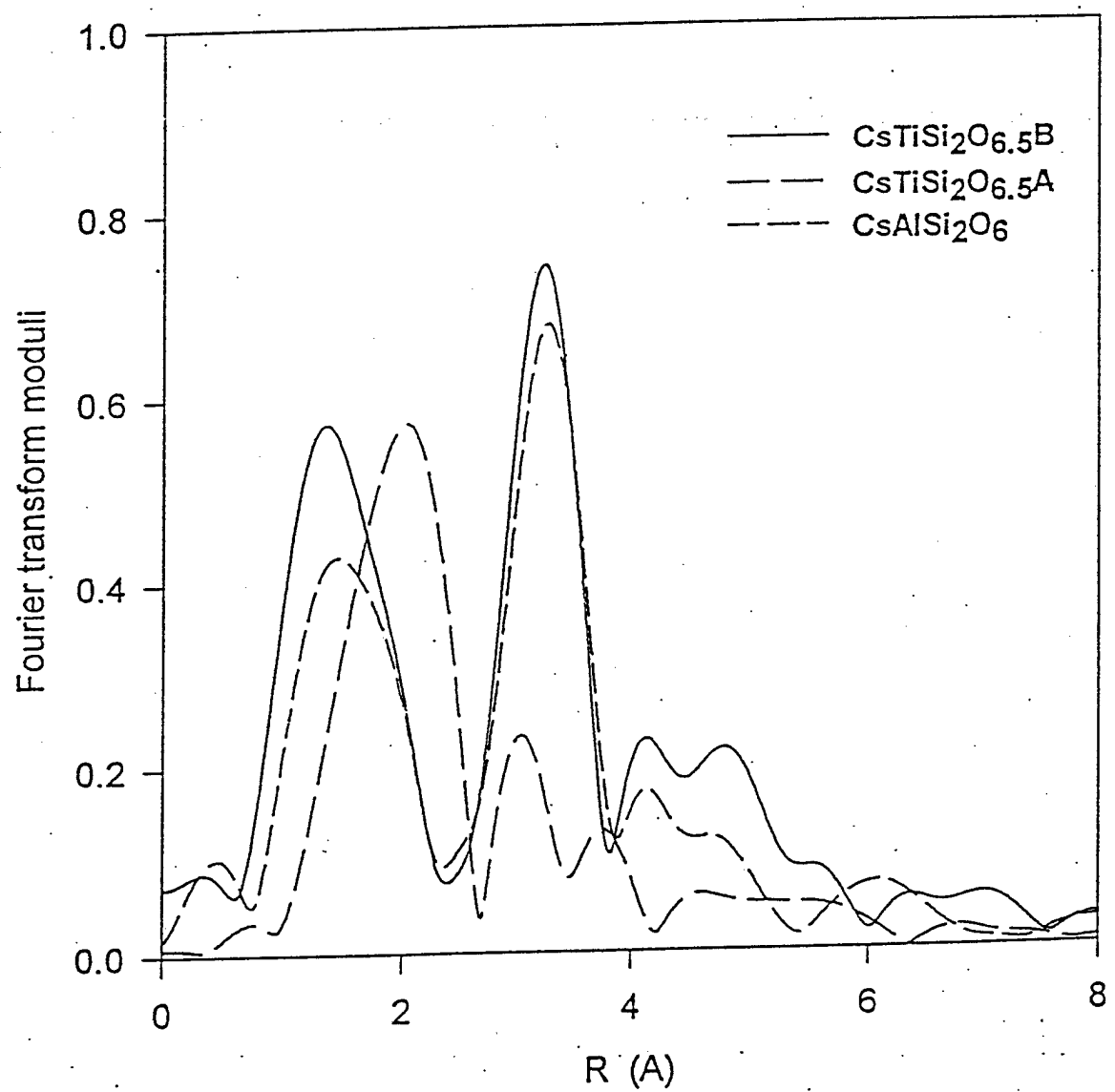


Figure 5.

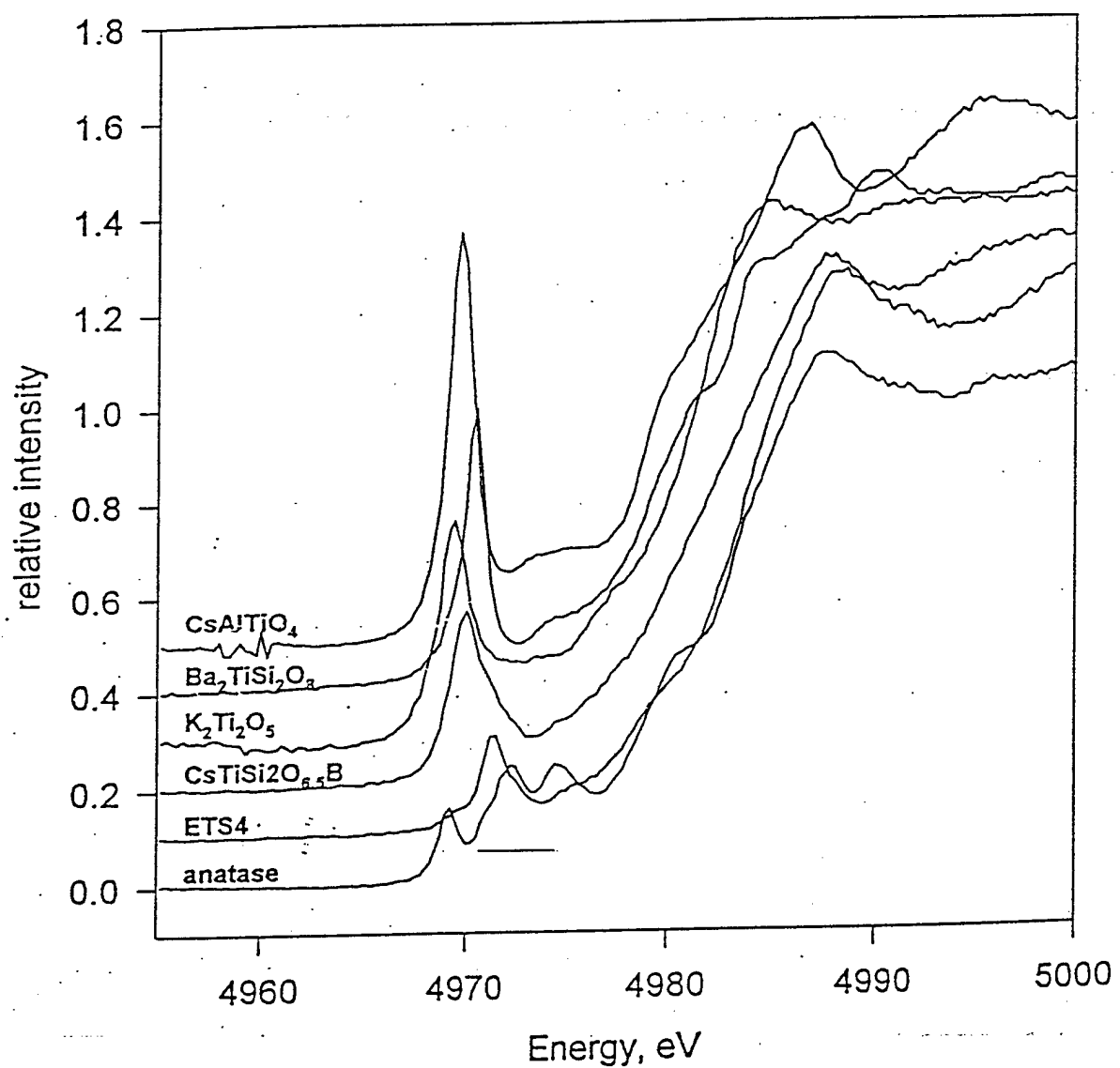


Figure 6.

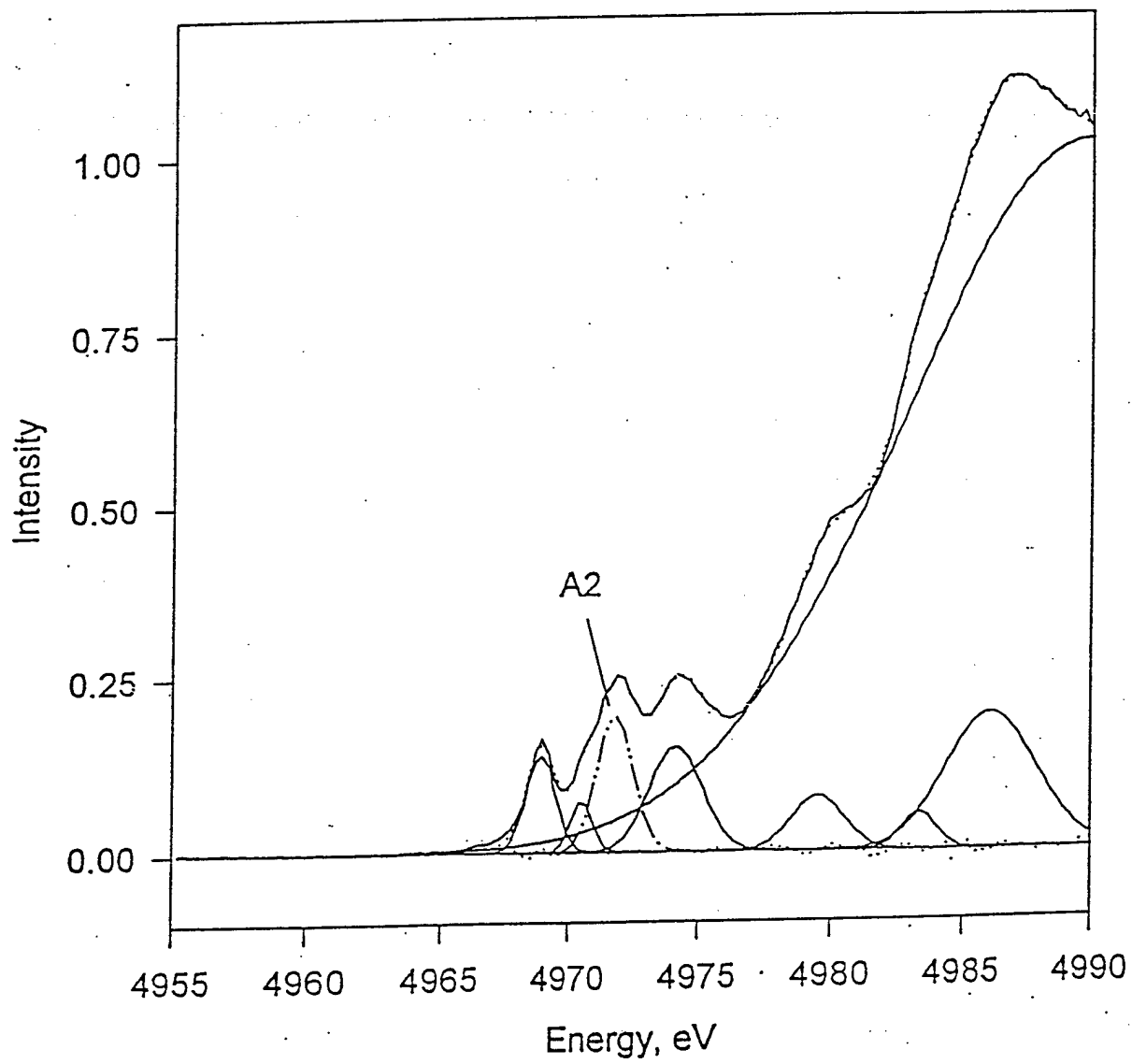


Figure 7.

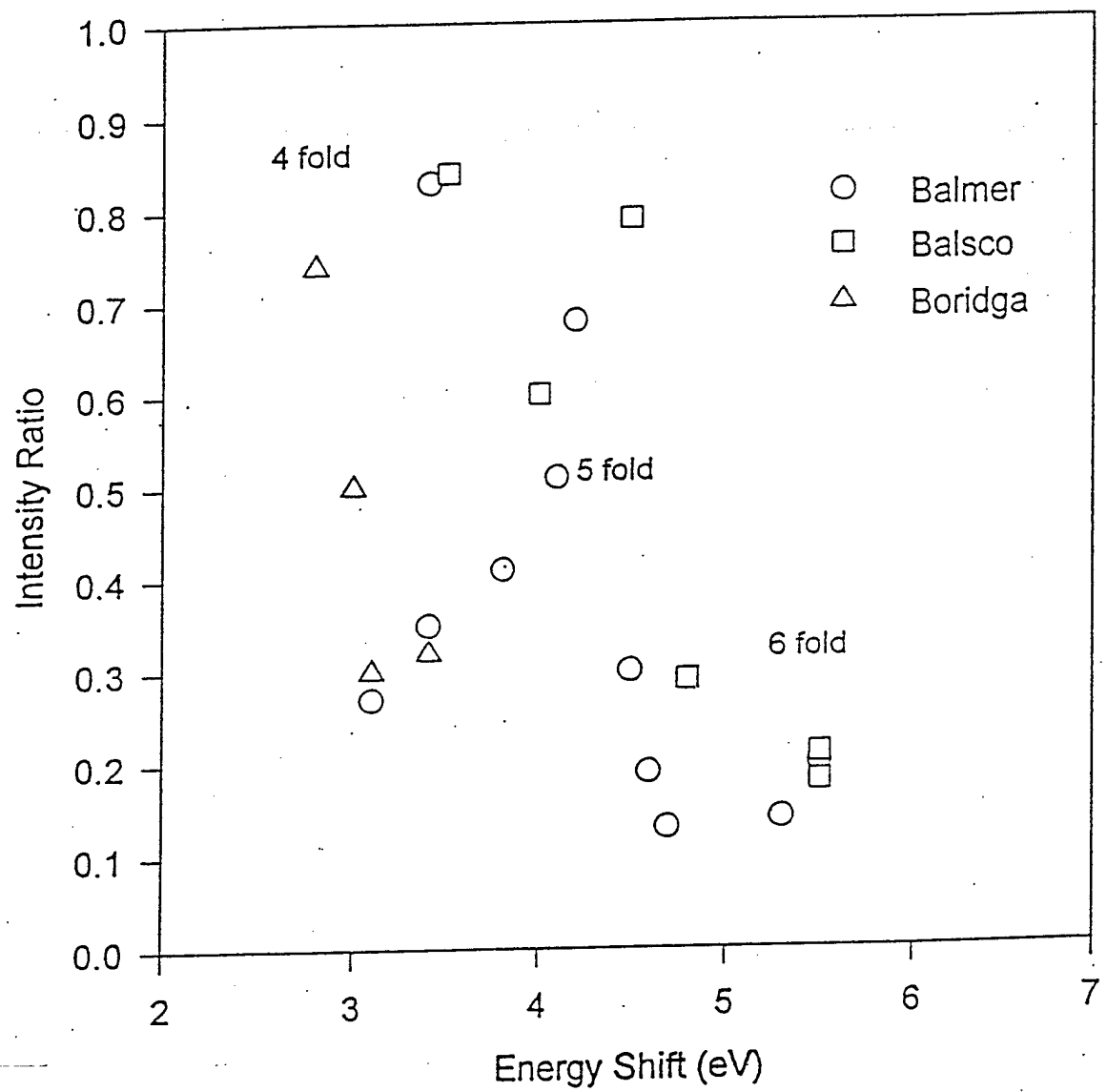


Figure 8.

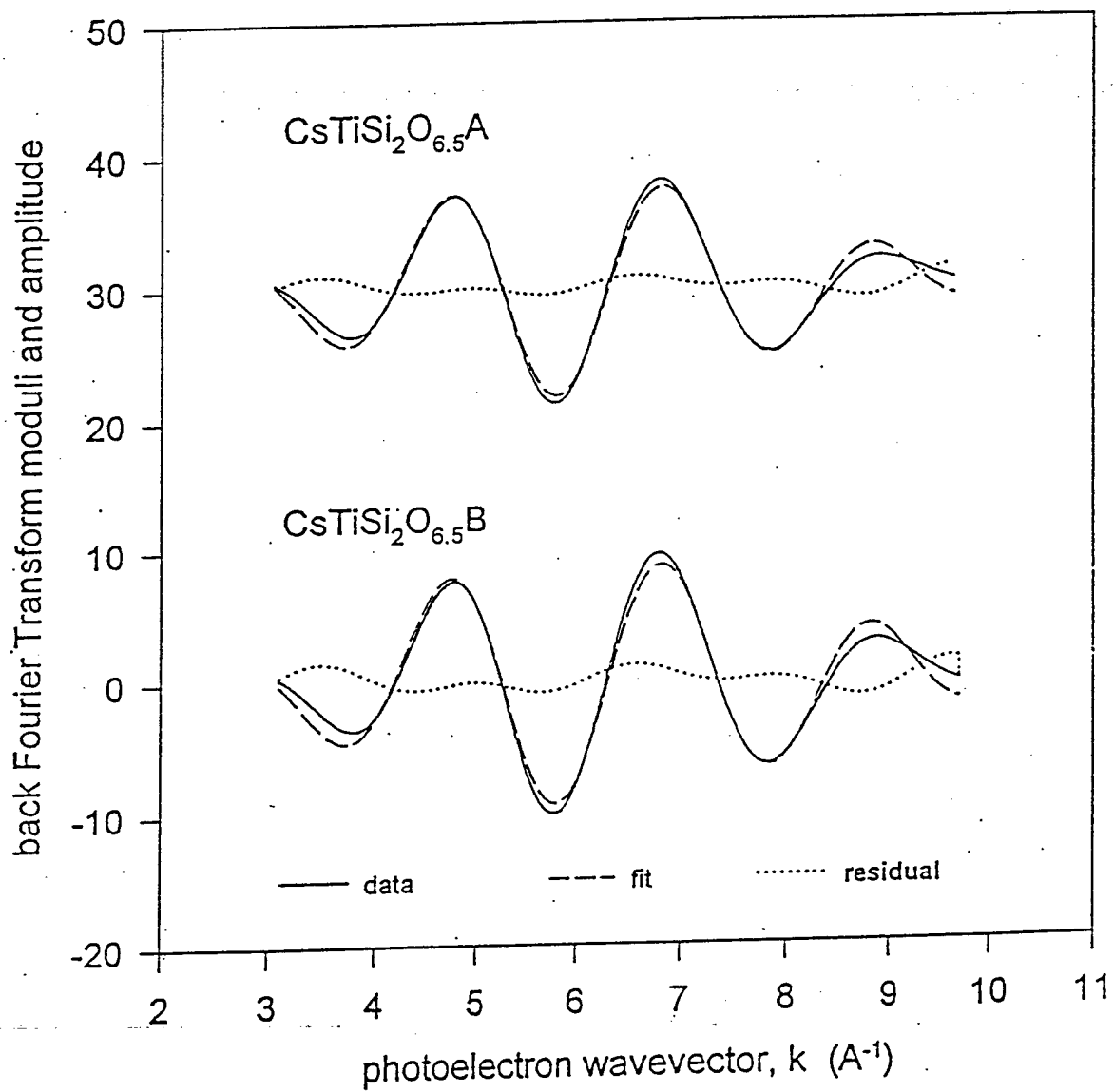


Figure 9.

Section 1d

Experimental and Calculated X-Ray Powder Diffraction Data for Cesium Titanium Silicate CsTiSi₂O_{6.5}: A New Zeolite

Experimental and Calculated X-ray Powder Diffraction Data for Cesium Titanium Silicate, $\text{CsTiSi}_2\text{O}_{6.5}$: A New Zeolite

David E. McCready, M. Lou Balmer, and Keith D. Keefer

Pacific Northwest National Laboratory

PO Box 999, Richland, Washington 99352

ABSTRACT

Standardized experimental and calculated x-ray powder diffraction data for a new synthetic zeolite, cesium titanium silicate, $\text{CsTiSi}_2\text{O}_{6.5}$, are reported. In addition, a structure model in space group $\text{Ia}3\text{d}$ (230), which is isomorphous with the mineral pollucite ($\text{CsAlSi}_2\text{O}_6 \cdot x\text{H}_2\text{O}$), is proposed for $\text{CsTiSi}_2\text{O}_{6.5}$. This structure model is the basis of the reported calculated x-ray powder diffraction data for $\text{CsTiSi}_2\text{O}_{6.5}$. The experimental pattern for $\text{CsTiSi}_2\text{O}_{6.5}$ shows this compound crystallizes in a body-centered cubic (BCC) unit cell with $a = 13.8423(1)$ Å. The measured value of the reference intensity ratio (I/I_c) of $\text{CsTiSi}_2\text{O}_{6.5}$ is 2.37, while the contrasting calculated value of I/I_c is 4.45. The experimental density (D_m) of $\text{CsTiSi}_2\text{O}_{6.5}$ is 3.48 ± 0.09 g/cm³, in agreement with the calculated density (D_x) of 3.42 g/cm³. Chemical analysis of $\text{CsTiSi}_2\text{O}_{6.5}$ by atomic absorption spectroscopy gives its composition as 54 ± 2 wt% Cs; 23 ± 2 wt% Ti; 23 ± 2 wt% Si, which compares favorably with the theoretical composition of 56 wt% Cs; 20 wt% Ti; 24 wt% Si.

KEYWORDS

x-ray powder diffraction, structure model, cesium titanium silicate, zeolite, pollucite

I. INTRODUCTION

Metastable and stable phase development from amorphous precursors in the system $\text{Cs}_2\text{O}-\text{TiO}_2-\text{SiO}_2$ has recently been investigated by Balmer and Bunker (1995). During the course of that work, a new, stable ternary phase was discovered: $\text{CsTiSi}_2\text{O}_{6.5}$. This new compound is an isomorph of the zeolitic mineral pollucite ($\text{CsAlSi}_2\text{O}_6 \cdot x\text{H}_2\text{O}$), which has the International Zeolite Association (IZA) structure type ANA (analcime-type).

Potential applications of $\text{CsTiSi}_2\text{O}_{6.5}$ include its proposed use as a form for containing radioactive Cs, a prevalent constituent of high-level defense nuclear wastes currently under study for remediation at Hanford, Washington and at other former nuclear weapons production sites in the United States. Incorporating radioactive Cs in $\text{CsTiSi}_2\text{O}_{6.5}$ for long-term storage is expected to be a viable alternative to vitrification and related proposed methods of nuclear waste treatment. Thus applied, $\text{CsTiSi}_2\text{O}_{6.5}$ has the potential benefit of facilitating the treatment of radioactive Cs-loaded nuclear wastes that also incorporate high concentrations of Ti-bearing compounds. In contrast, vitrification schemes are generally limited in application to the treatment of nuclear wastes that are Ti-loaded on the order of only a few weight percent. At higher Ti concentrations, solidified melts from vitrification processes typically include crystallized Ti-bearing by-products that generally cause instability of the resulting waste glass forms.

While further study of the application of $\text{CsTiSi}_2\text{O}_{6.5}$ to Cs remediation in high-level defense nuclear wastes is indicated, and additional characterization of $\text{CsTiSi}_2\text{O}_{6.5}$ is planned, the purpose of this paper is to present standardized experimental and calculated x-ray powder diffraction (XRPD) data for $\text{CsTiSi}_2\text{O}_{6.5}$. The present study also

proposes a zeolitic, BCC (Ia3d) structure model analogous to pollucite for $\text{CsTiSi}_2\text{O}_{6.5}$. A discussion of the substitution of Al^{3+} in pollucite by Ti^{4+} , and of the proposed structure model for $\text{CsTiSi}_2\text{O}_{6.5}$, is also presented.

II. SAMPLE PREPARATION

A. Synthesis

An amorphous, homogenous precursor of $\text{CsTiSi}_2\text{O}_{6.5}$ was synthesized using titanium and silicon alkoxides (tetraisopropyl orthotitanate, TIOT, and tetraethyl orthosilicate, TEOS) and cesium hydroxide. The alkoxides were mixed in a glove bag under nitrogen, after which a mixture of CsOH , water, and ethanol was added. The hydrolyzed precursor was stirred for a minimum of 15 h, then dried in air at room temperature. Subsequent TEM/EDS and XRPD analyses showed the stoichiometric precursor was both homogeneous and amorphous. Approximately 0.5 g of the precursor material was then heat-treated in a Pt crucible in air to produce crystalline $\text{CsTiSi}_2\text{O}_{6.5}$.

Two heat treatment schemes applied to the precursor yielded crystalline $\text{CsTiSi}_2\text{O}_{6.5}$. In the first scheme, the precursor was heated from room temperature to 800°C at 5°C/min, then held for at 800°C for a minimum of 1 h. Here, the onset of crystalline $\text{CsTiSi}_2\text{O}_{6.5}$ formation was observed at 750°C, while full crystallization occurred at 800°C. Upon further heating, the sample incongruently melted at 980°C. In the second scheme, the stoichiometric precursor was melted at 1200°C, then quenched to form a clear glass. The quenched glass was then ground to fine powder and heat-treated at 800°C for 30 h. Both methods produced crystalline $\text{CsTiSi}_2\text{O}_{6.5}$ in an opaque, white, solid bulk form. The

second preparation scheme was used to generate the sample material for the present study.

III. SPECIMEN PREPARATION AND DIFFRACTION DATA COLLECTION

The $\text{CsTiSi}_2\text{O}_{6.5}$ study sample was prepared for XRPD analysis by manually grinding the bulk material with an agate mortar and pestle, followed by sieving to -325 mesh ($<45\text{ }\mu\text{m}$) particle size. Specimens were mounted in a front-loading, shallow-cavity holder fabricated from low-background, off-axis, single-crystal quartz by the Gem Dugout, State College, PA. Data collection was performed at room temperature ($26 \pm 2^\circ\text{C}$), with and without any internal standard. For the standardized measurement, silicon (NIST SRM 640b) was added as an internal d-spacing standard. A 50/50 weight mixture of $\text{CsTiSi}_2\text{O}_{6.5}$ and corundum (NIST SRM 674) was used to measure the relative intensity ratio (I/I_c). A summary of the instrumental conditions and diffraction scan parameters used in this study appears in Table 1.

IV. RESULTS AND DISCUSSION

A. Experimental Diffraction Data for $\text{CsTiSi}_2\text{O}_{6.5}$

The unstandardized, experimental $\text{CsTiSi}_2\text{O}_{6.5}$ x-ray powder pattern is illustrated in Figure 1. The standardized experimental powder diffraction data for $\text{CsTiSi}_2\text{O}_{6.5}$ appear in Table 2. The reported experimental peak positions and d-spacings were corrected for 2θ error by comparing the measured and certified positions of the internal d-spacing standard (NIST SRM 640b), followed by applying the resultant second-order correction curve to the original position data. Note that the experimental peak positions and d-

spacings shown in parentheses in Table 2 were obscured by overlapping peaks of the internal d-spacing standard and were therefore calculated on the basis of the refined unit cell structure. The reported experimental intensities were the observed peak heights after background subtraction and were derived from the unstandardized diffraction pattern of $\text{CsTiSi}_2\text{O}_{6.5}$. In addition, the reported experimental intensities were corrected to the fixed-slit approximation using the $1/\sin\theta$ function resident in the x-ray powder pattern processing code JADE+, Ver. 2.1 (Materials Data, Inc., MDI, Livermore, CA). Lastly, note that no diffraction peaks occur for $\text{CsTiSi}_2\text{O}_{6.5}$ below the reported cutoff (8.84 Å, or $10^\circ 2\theta$ under Cu radiation).

B. Unit Cell Refinement

Initial inspection of experimental powder data for $\text{CsTiSi}_2\text{O}_{6.5}$ revealed its similarity to reference diffraction data for the mineral pollucite ($\text{CsAlSi}_2\text{O}_6 \cdot x\text{H}_2\text{O}$, PDF 15-317, 25-194, 29-407). Because the crystal structure of pollucite is a body-centered cubic (BCC) unit cell, space group Ia3d (230) with $a = 13.69$ Å (Beger, 1969), an analogous structure solution was sought for the experimental diffraction pattern of $\text{CsTiSi}_2\text{O}_{6.5}$. First, the 2θ error-corrected experimental d-spacings were indexed using the Louer algorithm-based code included in Micro-INDEX, Ver. 2.0 (MDI, Livermore, CA). The hkl-space search was limited to the cubic system with an input maximum lattice parameter of $a = 20$ Å and input unit cell volume limits of 2400-2800 Å³. The unit cell solution from indexing was $a = 13.841$ Å, with $F(50) = 29(0.006,271)$ and $M(50) = 20.2$. Next, the lattice parameter result from indexing and the 2θ error-corrected experimental d-spacings were input to the Appleman-Evans algorithm-based, auto-indexing cell refinement program resident in Micro-CELLREF, Ver. 2.0 (MDI, Livermore, CA). The

refinement code executed five least-squares cycles to reach convergence with an input 2θ -error limit of 0.03° . The final, refined lattice parameter was $a = 13.8423 (1) \text{ \AA}$.

C. Observed Non-Space Group Peaks

In addition to the diffraction data presented in Table 2, the $\text{CsTiSi}_2\text{O}_{6.5}$ study specimen also produced four weak, unindexed peaks. The 2θ error-corrected d-spacings and relative intensities of the unindexed peaks were: 3.6355 \AA , 2%; 3.5332 \AA , 2%; 3.2665 \AA , <1%; and 3.0228 \AA , <1%. The unindexed peak at 3.5332 \AA indicated the possible presence of a small amount of Anatase, TiO_2 (PDF 21-1272), in the sample. However, the match of this peak to reference powder data for Anatase was not determinative and may have been only coincidental. The peak at 3.2665 \AA could be indexed as (330), but this reflection is extinct in space group Ia3d (230). As such, this peak may have been evidence of some ordering phenomenon in the $\text{CsTiSi}_2\text{O}_{6.5}$ structure, but was otherwise unidentifiable. Similarly, the two remaining weak peaks at 3.6355 \AA and 3.0228 \AA could not be positively matched to any reference data in the ICDD Powder Diffraction File database (Sets 1-45, 1995).

D. Calculated Diffraction Data for $\text{CsTiSi}_2\text{O}_{6.5}$

X-ray powder diffraction data for $\text{CsTiSi}_2\text{O}_{6.5}$ were calculated using Micro-POWD, Ver. 2.3 (MDI, Livermore, CA). The basis of the calculated pattern was the proposed structure model for $\text{CsTiSi}_2\text{O}_{6.5}$ shown in Table 3. This structure model resulted from a separate study involving Rietveld refinement of neutron powder diffraction data for $\text{CsTiSi}_2\text{O}_{6.5}$ (Balmer *et.al.*, 1996a). A discussion of Ti substitution in pollucite and the rationale for the proposed structure model for $\text{CsTiSi}_2\text{O}_{6.5}$ is presented below. Other

inputs to Micro-POWD included the experimental refined lattice parameter for $\text{CsTiSi}_2\text{O}_{6.5}$, Philips-type FWHM peak widths, and Pearson VII peak profiles. Also input were fixed slits and the 2θ value for a graphite diffracted beam monochromator (26.38°). In addition, neutral scattering factors were used to calculate the powder pattern for $\text{CsTiSi}_2\text{O}_{6.5}$ because bonding mechanisms in compounds of this type are typically predominantly covalent. Anomalous dispersion corrections were also applied. The resultant calculated diffraction data for $\text{CsTiSi}_2\text{O}_{6.5}$ appear along with the experimental data in Table 2. The calculated intensities reported therein were the calculated peak heights. The Miller indices (hkl) shown in Table 2 also resulted from the Micro-POWD calculations.

A graphical comparison of the experimental and calculated x-ray powder data for $\text{CsTiSi}_2\text{O}_{6.5}$ is shown in Figure 2. This figure was constructed using the pattern simulation option in JADE+ (MDI) and the experimental and calculated d-spacings and intensities from Table 2. Acceptable agreement of the experimental and calculated patterns of $\text{CsTiSi}_2\text{O}_{6.5}$ is illustrated in Figure 2 by the plotted difference pattern.

E. Relative Intensity Ratio (I/Ic)

Three separate mounted specimens of a 50/50 weight mixture of $\text{CsTiSi}_2\text{O}_{6.5}$ and NIST SRM 674 (corundum) were scanned to determine the relative intensity ratio (I/Ic). After background subtraction and correction of intensity by $1/\sin\theta$, the experimental value of I/Ic was taken as the ratio of the height of the (400)/100% peak of $\text{CsTiSi}_2\text{O}_{6.5}$ to the height of the (113)/100% peak of corundum. The resulting average experimental value of I/Ic for $\text{CsTiSi}_2\text{O}_{6.5}$ was 2.37 (Table 2). In contrast, the calculated value of I/Ic output from Micro-POWD (for fixed slits) was 4.45.

Because of the stark discrepancy between the experimental and calculated values of I/I_c for $\text{CsTiSi}_2\text{O}_{6.5}$, an additional trial measurement of I/I_c was performed. A review of both the experimental procedures used and the inputs to Micro-POWD concluded that the relatively large particle size of the study specimen ($<45 \mu\text{m}$) may have accounted for the disagreement between the experimental and calculated values of I/I_c . Accordingly, a second subsample of $\text{CsTiSi}_2\text{O}_{6.5}$ was ground to a measured particle size of $2\text{-}3 \mu\text{m}$ using a McCrone Micronizing Mill and mixed 50 wt% with corundum. A scan of this 50/50 weight mixture of $\text{CsTiSi}_2\text{O}_{6.5}$ and corundum confirmed the original experimental result for I/I_c obtained from the -325 mesh study specimen.

Because the discrepancy between the experimental and calculated values of I/I_c for $\text{CsTiSi}_2\text{O}_{6.5}$ persisted, a cross-check of these results using natural mineral pollucite was performed. The pollucite sample obtained for this purpose contained minor impurities, but was deemed suitable for measuring I/I_c . The pollucite sample was mill-ground to $2\text{-}3 \mu\text{m}$ particle size and mixed 50 wt% with SRM 674 (corundum). The relative intensity ratio for the standardized pollucite specimen was then measured under the same conditions as was I/I_c of the study material. This experiment resulted in a value of I/I_c for pollucite of 1.93. Note that using Micro-POWD and crystal data for pollucite according to Beger (1969), the contrasting calculated value of I/I_c (for fixed slits) was 4.70.

Finally, I/I_c for $\text{CsTiSi}_2\text{O}_{6.5}$ was calculated using Micro-POWD with the input parameters *including* a 2θ compensating slit, as was integral with the study diffractometer. This resulted in a calculated value of I/I_c for $\text{CsTiSi}_2\text{O}_{6.5}$ of 2.45, which more closely agreed with the experimental value of I/I_c of 2.37. Accordingly, it appeared likely that the

observed discrepancies between the experimental and calculated values of I/I_c for $\text{CsTiSi}_2\text{O}_{6.5}$ and for mineral pollucite were due in large measure to artifacts of the beamline of the study diffractometer. Alternatively, other experimental errors may have contributed to the discrepancy between the observed and calculated values of I/I_c . Because experimental confirmation of the source of the discrepancy between the observed and calculated values of I/I_c was not practicable, the reported calculated value of I/I_c of 4.45 (for fixed slits) may be interpreted as best representing the actual value of I/I_c for $\text{CsTiSi}_2\text{O}_{6.5}$.

F. Density (D_m , D_x)

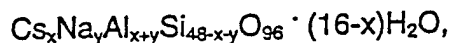
The density (D_m) of $\text{CsTiSi}_2\text{O}_{6.5}$ was measured by the helium expansion ratio method in six trials at $3.48 \pm 0.09 \text{ g/cm}^3$. The calculated density (D_x) of $\text{CsTiSi}_2\text{O}_{6.5}$, derived from the output of Micro-POWD, was 3.42 g/cm^3 , which agreed with the experimental value within the error limits.

G. Chemical Analysis

Chemical analysis was performed on the $\text{CsTiSi}_2\text{O}_{6.5}$ study sample dissolved in a mixture of nitric and hydrofluoric acid. Analysis of Cs, Ti, and Si content in the dissolved sample by atomic absorption spectroscopy yielded $54 \pm 2 \text{ wt\% Cs}$; $23 \pm 2 \text{ wt\% Ti}$; $23 \pm 2 \text{ wt\% Si}$ (excluding oxygen). These results were in good agreement with the theoretical elemental composition of $\text{CsTiSi}_2\text{O}_{6.5}$ (56 wt% Cs; 20 wt% Ti; 24 wt% Si), and were confirmed by semi-quantitative analysis of the bulk study material by SEM/EDX.

H. Ti Substitution in Pollucite

The mineral pollucite can be expressed by the general chemical formula



and is a network aluminosilicate containing interconnected 4- and 6-membered rings (Beger, 1969). Pollucite has been further described as a member of a series related to analcime, $\text{Na}(\text{Si}_2\text{Al})\text{O}_6 \cdot \text{H}_2\text{O}$ (Nel, 1944). According to that work, Na, together with H_2O , can substitute for Cs in pollucite. In the analcime framework (Ia3d), Al and Si are distributed on the 48g positions, with oxygen atoms on the 96h sites (Beger, 1969; Naray-Szabo, 1938). In pollucite, Cs occupies large cages centered around 16b at 1/8, 1/8, 1/8. Additionally, the 16b sites in pollucite are coordinated by 12 oxygens (Newnham, 1967; Naray-Szabo, 1938; Beger, 1969).

While direct substitution of Al^{3+} in this framework by Ti^{3+} would satisfy charge constraints, it is extremely unlikely that Ti^{3+} formation would occur in the oxidizing conditions under which the $\text{CsTiSi}_2\text{O}_{6.5}$ study sample was synthesized. Furthermore, the distinctly remote possibility of direct substitution of Ti^{3+} for Al^{3+} in the pollucite lattice was eliminated by analysis of the study material using x-ray photoelectron spectroscopy (XPS), which showed the Ti atoms in $\text{CsTiSi}_2\text{O}_{6.5}$ present primarily in the +4 oxidation state (Hess and Balmer, 1996).

Substitution of Al^{3+} in pollucite by Ti^{4+} requires the addition of eight oxygen ions per unit cell for charge balance. The results of Rietveld refinement of neutron diffraction data for $\text{CsTiSi}_2\text{O}_{6.5}$ place these eight additional oxygen atoms at sites slightly distorted from 16a, as shown in Table 3 (Balmer *et al.*, 1996a). Such siting of the additional oxygen

atoms places them within the Ti coordination sphere, which would result in fivefold coordination of the nearby Ti atoms. Confirmation of these results was by complementary analysis of the local structure of Ti in $\text{CsTiSi}_2\text{O}_{6.5}$ by extended adsorption fine structure (EXAFS), extended adsorption near edge structure (EXANES), and Raman spectroscopy, all of which showed Ti present in both fourfold and fivefold coordination with oxygen (Hess and Balmer, 1996). Combined with the results of ^{29}Si MAS NMR analysis, these results also showed that the additional oxygen atoms coordinate half of the Ti atoms as non-bridging oxygens (Balmer *et al.*, 1996b). That is, in eight of the 16 sites in the unit cell, Ti is fivefold coordinated by oxygen. The remaining eight Ti atoms in the unit cell of $\text{CsTiSi}_2\text{O}_{6.5}$ are in fourfold coordination.

VI. ACKNOWLEDGMENTS

The authors acknowledge Bruce Bunker of Battelle PNNL, who provided valuable advice during the course of this study, Mark Englehard of Battelle PNNL, who performed the XPS analyses, and Nancy Hess of Battelle PNNL, who conducted the EXAFS and EXANES analyses. In addition, Dr. Deane K. Smith of the Pennsylvania State University generously provided guidance in the application and use of Micro-POWD. This work was supported by the Strategic Environmental Research and Development Program (SERDP) of the U.S. Department of Energy, and through the Tank Waste Remediation Science (TWRS) program directed by Westinghouse Hanford Company, Richland, WA, USA. Pacific Northwest National Laboratory is operated for the U.S. Department of Energy by Battelle under Contract DE-AC06-76RLO 1830.

VII. REFERENCES

Balmer, M.L., and Bunker, B.C. (1995). *Inorganic Ion Exchange Evaluation and Design - Silicotitanate Ion Exchange Waste Conversion*. Report #PNL-10460, Pacific Northwest Laboratory Richland, WA 99352.

Balmer, M.L., Huang, Q., Wong-Ng, W., Roth, R., Santoro, A. (1996a). *Neutron and X-ray Diffraction Study of the Crystal Structure of $CsTiSi_2O_6.5$* . Submitted to J. Sol. State Chem.

Balmer, M.L., Wang, L.Q., Peden, C.H.F., and Bunker, B.C. (1996b). *Solid State ^{29}Si MAS NMR Study of Silicotitanates*. Submitted to Chem. Mater.

Beger, R.M. (1969). *The Crystal Structure and Chemical Composition of Pollucite*. Z. Kristallogr., 129, 280-302.

Hess, N.J. and Balmer, M.L. (1996). *Ti XAS of a Novel Cs-Ti-Silicate*. Submitted to J. Sol. State Chem.

Powder Diffraction File PDF-2 Database (1995). PDF 15-317, 21-1272, 25-194, 29-407, JCPDS-ICDD.

Nel, H.J. (1944). *Pollucite from Karibib, South West Africa*. Amer. Mineral., 29, 443-452.

Newnham, R. E. (1967). *Crystal Structure and Optical Properties of Pollucite*.

Am. Mineral., Mineral. Notes, 32, 1515-1518.

St. V. Naray-Szabo (1938). *Die Struktur des Pollucits $CsAlSi_2O_6 \cdot xH_2O$.*

Z. Kristallogr., 99, 277-282.

TABLE I. Instrumental Conditions and Diffraction Scan Parameters

INSTRUMENTAL CONDITIONS

Goniometer : Philips Type PN3550/00X, Vertical
X-ray Source : Fixed-Anode LFF Cu Tube
Power : 40 kV, 45 mA (1800 W)
Radiation, λ : Cu K α 1, 1.540598 Å
Monochromator : Graphite
Counter : Scintillation
Soller Slits : Employed on incident beam side only
Divergence Slit : Variable
Receiving Slit : Fixed, 0.2 mm

DIFFRACTION SCAN PARAMETERS

<u>2θ Range</u>	<u>Scan Rate</u>	<u>Comments</u>
10 - 130°	0.02° / 10 s	No internal standard used. No peaks observed below 10°.
10 - 130°	0.02° / 30 s	SRM 640b (Si) added as internal d-spacing standard.
20 - 30°; 40 - 50°	0.02° / 3 s	SRM 674 (Corundum) added for I/I _c measurements.

TABLE II. Experimental and Calculated X-ray Powder Diffraction Data for $\text{CsTiSi}_2\text{O}_{6.5}$.

Cesium Titanium Silicate				$\text{CsTiSi}_2\text{O}_{6.5}$				
Radiation: $\text{CuK}\alpha 1$	$\lambda: 1.540598 \text{ \AA}$		Filter: Monochromator	d-sp: Diffractometer				
Cutoff: 8.84	Int: Diffractometer		I/I_c (obs): 2.37	I/I_c (calc): 4.45				
System: Cubic				Space Group: $\text{Ia}3\text{d}$ (230)				
$a: 13.8423 (1)$				$Z: 16$				
$D_x: 3.42$				$D_m: 3.48$				
SS/FOM: $F(50) = 29(0.006, 271)$				Color: White				
$2\theta_{\text{obs}}$	d_{obs}	I_{obs}	$h\ k\ l$	$2\theta_{\text{calc}}$	d_{calc}	I_{calc}		
15.670	5.6505	4	2 1 1	15.66	5.651	6		
18.120	4.8919	1	2 2 0	18.12	4.894	1		
24.040	3.6989	48	3 2 1	24.04	3.700	50		
25.720	3.4610	100	4 0 0	25.72	3.461	100		
28.812	3.0962	2	4 2 0	28.82	3.095	1		
30.263	2.9509	45	3 3 2	30.26	2.951	42		
31.637	2.8258	1	4 2 2	31.64	2.826	<1		
32.975	2.7141	4	4 3 1	32.96	2.715	2		
35.500	2.5267	6	5 2 1	35.50	2.527	8		
36.704	2.4465	26	4 4 0	36.70	2.447	33		

40.129	2.2453	12	6 1 1	40.12	2.246	15
41.207	2.1890	<1	6 2 0	41.22	2.189	1
42.286	2.1356	<1	5 4 1	42.28	2.136	<1
44.352	2.0408	7	6 3 1	44.34	2.041	8
45.367	1.9975	4	4 4 4	45.36	1.9980	5
46.346	1.9575	1	5 4 3	46.34	1.9576	<1
(47.317)	(1.9196)	1	6 4 0	47.32	1.9196	1
48.287	1.8833	14	7 2 1	48.28	1.8837	16
49.224	1.8496	<1	6 4 2	49.22	1.8498	<1
51.986	1.7576	13	6 5 1	51.98	1.7580	16
52.885	1.7299	3	8 0 0	52.88	1.7303	4
53.767	1.7035	2	7 4 1	53.76	1.7039	1
54.631	1.6786	<1	8 2 0	54.62	1.6786	<1
55.508	1.6541	2	6 5 3	55.50	1.6545	3
(56.353)	(1.6314)	<1	6 6 0	56.36	1.6313	<1
57.210	1.6089	1	8 3 1	57.20	1.6091	1
58.886	1.5671	2	7 5 2	58.88	1.5673	3
59.708	1.5474	4	8 4 0	59.70	1.5476	6
61.342	1.5101	<1	8 4 2			
62.147	1.4924	2	9 2 1	62.14	1.4927	4
62.934	1.4756	<1	6 6 4	62.94	1.4756	<1
63.744	1.4588	<1	7 5 4	63.74	1.4591	<1
65.308	1.4276	2	9 3 2	65.30	1.4277	4
66.088	1.4127	2	8 4 4	66.08	1.4128	3
66.853	1.3983	<1	9 4 1			

67.617	1.3844	<1	8 6 0	67.62	1.3842	<1
68.390	1.3706	3	7 7 2	68.40	1.3706	4
71.421	1.3197	3	9 5 2	71.42	1.3198	5
72.904	1.2965	<1	8 7 1	72.90	1.2965	<1
73.641	1.2853	<1				
74.384	1.2743	1	9 6 1	74.38	1.2743	1
(75.853)	(1.2532)	<1	8 7 3			
77.319	1.2331	1	9 6 3	77.32	1.2332	2
78.042	1.2235	<1	8 8 0	78.04	1.2235	1
80.205	1.1958	1	11.3.2	80.20	1.1958	3
81.644	1.1784	<1	8 7 5	81.64	1.1783	<1
83.084	1.1615	<1	9 6 5	83.08	1.1616	<1
83.799	1.1534	1	12.0.0	83.80	1.1535	1
85.925	1.1303	<1	11.5.2	85.92	1.1302	2
88.777	1.1012	<1	11.6.1	88.78	1.1012	1
89.482	1.0943	<1	12.4.0	89.48	1.0943	1
90.178	1.0877	<1	11.5.4			
90.889	1.0810	<1	12.4.2			
91.606	1.0744	<1	9 9 2	91.62	1.0744	1
94.448	1.0494	<1	11.7.2	94.46	1.0494	1
(95.165)	(1.0434)	<1	12.4.4	95.16	1.0434	1
96.584	1.0318	<1	12.6.0			
97.305	1.0261	<1	10.9.1	97.30	1.0261	1
98.736	1.0150	<1	13.4.1			
100.174	1.0043	<1	10.9.3	100.18	1.0042	<1

100.906	0.9990	<1	8 8 8	100.90	0.9990	<1
101.614	0.9939	<1	12.7.1			
103.079	0.9837	<1	14.1.1	103.08	0.9837	1
106.005	0.9645	1	11.9.2	106.02	0.9644	1
			12.8.0	106.76	0.9598	<1
108.988	0.9463	<1	13.6.3	108.98	0.9462	<1
112.009	0.9291	<1	11.10.1	112.02	0.9290	1
112.790	0.9249	<1	12.8.4	112.78	0.9249	1
115.103	0.9128	<1	14.5.3	115.12	0.9127	1
118.281	0.8973	<1	15.3.2	118.30	0.8973	<1
121.569	0.8826	<1	11.10.5	121.58	0.8826	<1
124.965	0.8686	<1	13.7.6	124.96	0.8685	1
			15.6.1	128.52	0.8552	<1

TABLE III. Proposed Structural Model for $\text{CsTiSi}_2\text{O}_{6.5}$.

Space Group: Ia3d (230)				a: 13.8425 (1)	Z: 16	
<u>Atom</u>	<u>x</u>	<u>y</u>	<u>z</u>	<u>Wyckoff Position</u>	<u>Occupancy</u>	<u>B_{iso}</u>
Cs	0.125	0.125	0.125	16b	1	4.0
Ti	0.661	0.589	0.125	48g	1/3	6.3
Si	0.661	0.589	0.125	48g	2/3	6.3
O(1)	0.1042 (2)	0.1349 (3)	0.7175 (3)	96h	1	*
O(2)	0.706	0.062	0.021	96h	0.060 (4)	4.8
O(3)	0.791	0.205	0.235	96h	0.023 (4)	4.8

* $B(1,1) = 8.8 (3)$; $B(2,2) = 8.0 (3)$; $B(3,3) = 4.2 (2)$

$B(1,2) = 1.6 (2)$; $B(1,3) = 1.6 (2)$; $B(2,3) = 0.5 (2)$

Reference: Balmer *et al.*, (1996a).

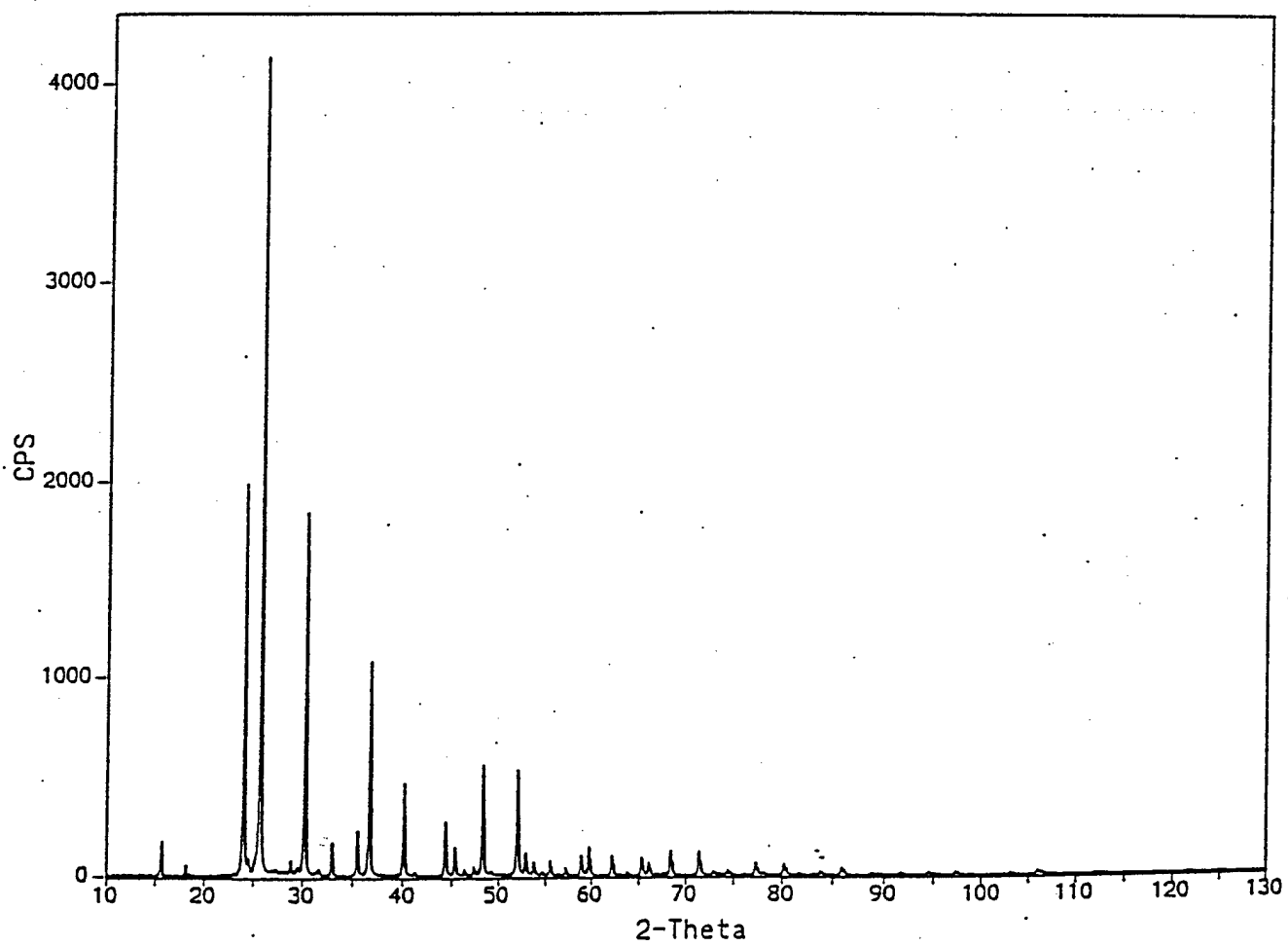


Figure 1. X-ray Powder Diffractogram of Cesium Titanium Silicate, $\text{CsTiSi}_2\text{O}_{6.5}$.

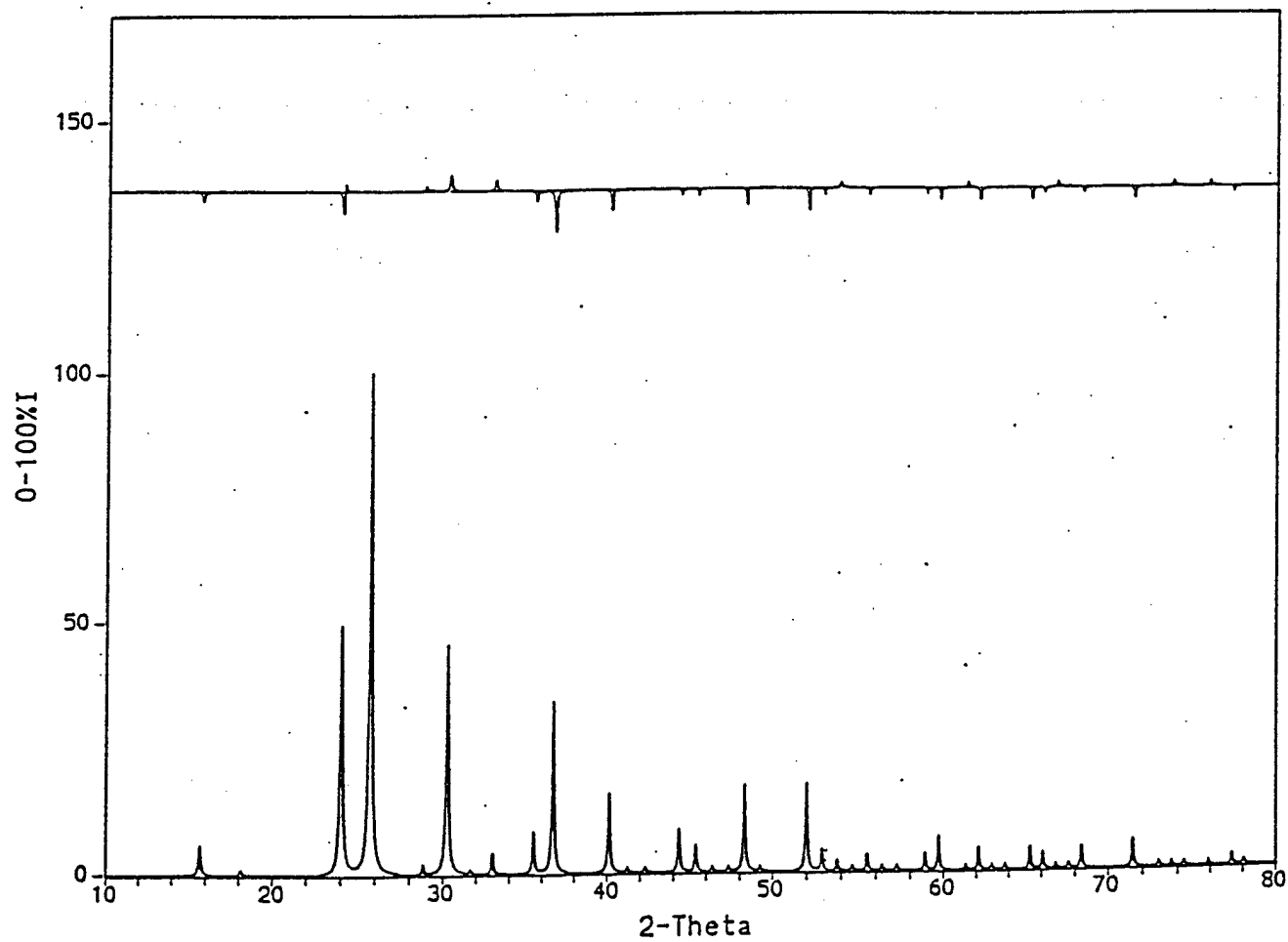


Figure 2. Experimental vs. Calculated X-ray Powder Diffraction Data for $\text{CsTiSi}_2\text{O}_{6.5}$.

Chapter 2

IMMOBILIZATION OF HIGH-LEVEL RADIOACTIVE SLUDGES IN IRON PHOSPHATE GLASS

FINAL TECHNICAL REPORT
to
BATTELLE PACIFIC NORTHWEST LABORATORIES

Subcontract No. 295503-A-F1
for the period
1 January 1995 to 30 September 1996
Waste Form Remediation-Disposal of Radioactive Waste in Glass

**"IMMOBILIZATION OF HIGH-LEVEL RADIOACTIVE SLUDGES IN IRON
PHOSPHATE GLASS"**

Written by
Delbert E. Day, Curator's Professor
and
Melissa Mesko, Graduate Research Assistant

Ceramic Engineering Department and
Graduate Center for Materials Research
University of Missouri-Rolla
Rolla, MO 65401

Phone: 573-341-4354

30 December 1996

Immobilization of High-Level Radioactive Sludges in Iron Phosphate Glass

Abstract

Iron phosphate wasteforms made by vitrifying four Hanford high-level radioactive waste sludges were investigated. Determining the maximum amount of sludge that could be incorporated in the iron phosphate wasteform along with an evaluation of the chemical durability of the wasteform was the prime focus of this study. The density, thermal expansion coefficient, dilatometric softening temperature, and crystallization temperature of the wasteforms were also measured.

Up to 60 wt% of the C-112 sludge, 50 wt% of the B-110 and T-111 sludges, and 20 wt% of the C-106 sludge could be vitrified with an iron phosphate glass at $<1200^{\circ}\text{C}$ in a short time (~1 hour). The dissolution rate of the glassy wasteforms in distilled water at 90°C was 10^{-8} to 10^{-9} $\text{g/cm}^2/\text{min}$ which was equivalent to, or lower than that of three borosilicate waste glasses, the R7T7 glass developed in France, the CVS-IS glass developed at Pacific Northwest National Labs (PNNL), and the DWPF-EA glass developed at the Savannah River Laboratory (SRL). The excellent chemical durability of the glassy iron phosphate wasteform was retained even after crystallizing the glass for 24 hours at temperatures between 650 and 750°C .

Wasteforms made with 7 wt% CaF_2 in the batch melted at a lower temperature and had a lower melt viscosity, but about the same chemical durability. Adding CaF_2 to the batch caused a small amount of phase separation and crystallization to occur in the glassy wasteform in some cases which in turn increased the tendency for the wasteform to crystallize. Although the crystallization tendency was increased, crystallized wasteforms made with CaF_2 had a lower

dissolution rate (10^{-9} g/cm²/min) in distilled water at 90°C than crystallized wasteforms not made with CaF₂ (10^{-8} g/cm²/min).

Introduction

The Hanford site in Washington State was originally built in the early 1940's to produce plutonium for the nation's first atomic weapons. Throughout its years of operation during and after WWII, approximately 1.4 billion cubic meters of hazardous and radioactive wastes were generated.¹ Some of these wastes were discharged into the ground, air, and water, but the majority of the high level wastes (HLW) have been temporarily stored in large, underground metal tanks awaiting permanent disposal. In the 1980's Hanford was closed as a production facility as large stock piles of nuclear weapons were no longer needed, but the HLW from the previous years still remained. In 1989, Hanford undertook a new mission-to permanently dispose of the nuclear wastes accumulated during the previous 50 years.

The Hanford site contains approximately two thirds of all of the Department of Energy's (DOE's) high-level waste.¹ The HLW at the Hanford site is present in many forms including liquids, sludges, and salt cakes most of which are stored in large single or double wall steel tanks. Each steel tank can hold from 500,000 to 1.1 million gallons of waste. The primary problem at Hanford stems from the fact that the HLW contained in these tanks is chemically corrosive and the metal tanks now in use were designed only for temporary storage. Monitoring of the soil around the tanks shows that many tanks are already leaking waste into the ground at Hanford.¹ Finding a safe, permanent disposal form for these wastes is a primary concern.

An additional problem at Hanford is the variety of HLW compositions in the

tanks. HLW accumulated over the past 50 years came from different sources and have widely varying compositions. The fact that the waste composition varies significantly from tank to tank poses the problem of finding a permanent disposal mode that can accommodate a wide range of waste compositions.

The DOE has decided that the primary route for disposing of HLW in the United States is to vitrify the HLW to form a chemically durable glassy wasteform. Vitrification is achieved by melting a mixture of the HLW and other material (usually a glass powder or frit) to form a glassy wasteform whose properties satisfy the stringent requirements for nuclear waste disposal such as a high waste loading (cost factor) and high chemical durability (safety factor). The decision to immobilize the HLW in a glassy wasteform rather than other types of wasteforms, such as Synroc or tailored ceramics, was based on the favorable properties of glass. Glass can contain large amounts of waste, can have a high chemical durability, and is easy to process. Glasses can be melted continuously, in a short amount of time (a few hours), at low temperatures (typically $<1300^{\circ}\text{C}$). This makes glass easy and safe to process remotely, and at a reasonable cost.

Currently borosilicate glasses are being investigated for vitrifying many of the different waste compositions at Hanford.² A borosilicate glass is currently being used at the Savannah River Site and in other foreign countries for the vitrification of certain HLW.^{2,3} Borosilicate glasses have desirable properties for nuclear waste disposal applications including a low melting temperature ($1200\text{-}1300^{\circ}\text{C}$), a low dissolution rate in distilled water (10^{-8} to 10^{-9} g/cm²/min) and a high waste loading

(typically 30 wt%).⁴ Most importantly borosilicate glasses have been made commercially for >50 years and are well understood. While many waste compositions are suitable for disposal in a borosilicate glass, some HLW compositions are not. Wastes that are high in phosphorus, fluorine, and heavy metals (actinides) often have a low solubility limit⁵ in borosilicate glasses. This low solubility can limit the waste loading to unreasonably low percentages (costly), or worse yet, cause immiscible liquids to form which increase the risk of poor chemical durability.

To efficiently dispose of the wide range of HLW compositions in a cost effective manner, it is likely that a small number of other glasses, which are capable of immobilizing those specialized wastes that are incompatible with borosilicate glass, will be required. One potential candidate is certain phosphate glasses. Phosphate glasses can contain large amounts of phosphorus, fluoride, and heavy metals. In addition, phosphate glasses that contain a large amount of Fe_2O_3 (~ 40 wt%) have a melting temperature (1200°C) and dissolution rate in distilled water (10^{-8} to 10^{-9} g/cm²/min) comparable to the borosilicate glasses.⁶⁻⁹

The objective of this work was to determine the feasibility of immobilizing four Hanford tank sludges in a glassy iron phosphate wasteform. The sludges selected for study had a composition that was expected to make them poorly suited or incompatible with borosilicate glasses. The melting temperature, time, and waste loading for the iron phosphate glassy wasteforms were measured for comparison with the borosilicate glass wasteforms currently being considered. In addition,

physical properties such as density, thermal expansion coefficient, dilatometric softening temperature, and crystallization temperature of the sludge containing iron phosphate glass wasteforms were also measured.

The bulk dissolution rate of the glassy and crystallized iron phosphate wasteforms were measured as a function of pH in HCl (pH 2), distilled water (pH 7) and NH₄OH (pH 12) at 90°C for up to 16 days. The chemical dissolution of selected glasses was also measured using the Product Consistency Test (PCT). A mechanism for the dissolution of the sludge-containing iron phosphate glass wasteforms is proposed based on Scanning Electron Microscopy (SEM) and Energy Dispersive Spectroscopy (EDS) analysis of the corroded surfaces and the composition of the leachate solution from the PCT.

Finally, a small amount of CaF₂ (7 wt%) was added to selected batches used to prepare the sludge-containing glass wasteforms for the purpose of determining the effect of CaF₂ on the melting temperature, glass formation tendency, and physical properties of the resulting glassy wasteform.

Experimental

(1) Glass Formation

Four Hanford sludges (C-106, B-110, C-112, and T-111)¹⁰ were selected because they were estimated to be unsuitable for vitrification in a borosilicate glass and were representative of the wide variety of waste compositions at Hanford. The sludge compositions were simplified by using only the components that exceeded 1 wt% (Table I). The C-106 sludge is from the Purex process and has a high concentration of Al_2O_3 (18 wt%) and SiO_2 (35 wt%). The B-110 and T-111 sludges come from different steps in the bismuth phosphate process so they have a high concentration of Bi_2O_3 (30 wt%) and Fe_2O_3 (31 wt%). The C-112 sludge is also from the bismuth phosphate process, but has large concentrations of P_2O_5 (14 wt%) and UO_2 (30 wt%) since this waste is from the first cycle of this process. All four sludges contain substantial amounts of Fe_2O_3 (from 17 to 31 wt%) and three of the four sludges contain substantial SiO_2 , up to 35 wt% in C-106.

To determine how much of each sludge could be vitrified in an iron phosphate wasteform, fifty gram batches were melted which contained 20, 30, 35, and 40 wt% of each sludge, a fixed percentage (30 wt%) of Fe_2O_3 , and the balance being P_2O_5 . To obtain higher waste loadings (40, 50 and 60 wt% sludge), the Fe_2O_3 content was decreased to 10 wt%. The batch composition of each wasteform prepared in the present work is given in Tables II through V.

A previous study¹¹ on sludge-containing iron phosphate glassy wasteforms

showed that adding 7 wt% CaF_2 to the batch reduced the melting temperature by up to 50°C and reduced the tendency for devitrification which allowed more waste to be in the glass wasteform. For this reason, 7 wt% CaF_2 was added to the batches containing 20 and 30 wt% sludge, see Tables VI and VII.

Fifty gram batches of each composition in Tables II to VII were prepared using reagent grade materials.^{**} All components except the P_2O_5 were weighed and mixed thoroughly in a glass container. Once thoroughly mixed, and just prior to melting, the P_2O_5 was mixed with the batch because of its extremely hygroscopic nature. Batches were charged 3 to 4 times into a high purity alumina crucible at 800 to 1000°C and then melted for approximately 1 hour at 1050 to 1300°C. The melts were stirred 2 to 3 times with an alumina rod^{***} to aid in homogenization. Each melt was cast into a steel mold to produce a bar 1 x 1 x 4-6 cm which was annealed between 500 and 600°C for 2 to 6 hours and slowly cooled to room temperature.

The batches containing CaF_2 were better glass formers than the corresponding batches without CaF_2 . The batches containing CaF_2 melted at lower temperatures (50°C lower) and the melts were more fluid. The wasteforms made with CaF_2 were annealed at lower temperatures as well (525 to 550°C).

*Johnson Mathey Alfa, Ward Hill, MA

**Fisher Scientific Corp., Fair Lawn, NJ

***Coors Ceramic Company, Golden, CO

The majority of the resulting glasses were black and opaque. Some of the glasses developed a thin (microns) metallic-looking blue, green, or gold layer on the surface after being cast. This thin layer could be removed by grinding with 240 grit SiC paper.

(2) Microstructure

In addition to visual inspection, the microstructure of selected glassy wasteforms was investigated using X-Ray Diffraction* (XRD) and Transmission Electron Microscopy (TEM). Both XRD and TEM were used to determine if the resulting material was amorphous and homogeneous.

(3) Properties

The density, ρ , of one sample of each of the glassy wasteforms was determined by the Archimedes' technique using distilled water as the suspending medium, see Tables VIII and IX. The average linear thermal expansion coefficient, α , and dilatometric softening temperature, T_s , were measured using an auto-recording dilatometer**. T_s was determined as the peak of the expansion curve and α was calculated from the average slope of the expansion curve between 250 and 450°C (Tables VIII and IX).

The tendency for selected glassy wasteforms to devitrify upon heating was

*XRD-5 Diffractometer, General Electric Company Schenectady, NY

**The Edward Orton Jr. Ceramic Foundation, Westerville, OH

studied using Differential Thermal Analysis (DTA). DTA curves were recorded for samples heated at 5°C/min in flowing nitrogen (50 cm³/min). The crystallization temperature, T_c , was taken as the temperature of the first exothermic DTA peak (Tables VIII and IX).

XRD was used to determine what compounds crystallized from the glass wasteforms after re-heating above their respective crystallization temperature. Approximately 2 gram samples of bulk glass were reheated at 5°C/min to a chosen temperature between 650 to 750°C and held for 24 hours. The crystallized samples were then ground to a -200 mesh powder and the diffraction measured from $2\theta = 10$ to 80° with CuK α radiation. The diffraction patterns for selected glassy wasteforms are shown in Figure 1.

(4) Chemical Durability

(a) Bulk Dissolution Rate: The bulk dissolution rate of the glassy and crystallized wasteforms were measured using a technique similar to the Materials Characterization Center static leach test (MCC-1)¹². Specimens were diamond sawed from the annealed bars then ground with 240 grit SiC paper. The dimensions of each specimen were measured and were approximately 1 x 1 x 1 cm. Some of the samples were crystallized by heating at 5°C/min to a temperature between 650 and 750°C for 24 hours. It should be noted that the dimensions of crystallized specimens often changed slightly after crystallization due to softening of the glass. For this reason, the dimensions measured before crystallization were used to calculate the

surface area of the crystallized specimens. The glass and crystallized specimens were then rinsed with distilled water, dried at 120°C, cooled to room temperature, and then weighed. Each glass specimen was suspended by a thin rayon thread in a glass flask containing 100mL of HCl (pH 2), distilled water (pH 7), or NH₄OH (pH 12) (Figure 2). The crystallized samples were only tested in distilled water. The solutions were not renewed during this corrosion test. The glass flasks containing the wasteform were placed in a 90°C oven. Specimens were removed after 2, 4, 8, and 16 days, rinsed with distilled water, dried at 120°C, cooled, and weighed (± 0.01 mg).

The dissolution rate (D_R) was calculated from the measured weight loss (ΔW) using the equation:

$$D_R = \frac{\Delta W}{A \cdot t} \quad (1)$$

where A is the surface area (cm^2) of the sample and t is the time (min) that the specimen was immersed in the test solution at 90°C. The weight loss, ΔW , is $W_i - W_t$ where W_i is the initial weight of the sample and W_t is the weight of the same sample after time, t . Two samples of each glass were tested and the average D_R value is given herein. The estimated error for D_R is $\pm 1 \times 10^{-8} \text{ g/cm}^2/\text{min}$.

(b) Surface Analysis: A Scanning Electron Microscope (SEM)^{*} was used to observe the outer surface of the immersed glass samples. Energy Dispersive Spectroscopy (EDS) was used to measure the change in composition of the surface of

^{*}JEOL JCM-35CF Tokyo, Japan

selected wasteforms upon completion of the bulk dissolution rate test. Each specimen was cut in half and the composition of the surface exposed to the test solution was compared to the interior, or unexposed composition. This was done to determine if non-uniform dissolution occurred, indicating selective leaching or the formation of a surface layer.

(c) **Product Consistency Test (PCT):** The PCT also measures the dissolution rate of a glass sample, but uses a higher surface area of glass to volume of solution than an MCC-1 type test. Approximately 1 gram of glass powder (-100 to +200 mesh) is mixed with 15mL of distilled water in a stainless steel vessel held at 90°C for seven days. After completion of the PCT, the leachate is filtered and the concentration of elements in solution is measured. A thorough description of the PCT can be found in ASTM C 1285-94 and was used when testing the glasses in this study. Ion Coupled Plasma-Energy Spectroscopy (ICP-ES) was used to analyze the leachate solutions. The iron phosphate wasteforms were compared to the Approved Reference Material (ARM-1)¹³ which is standard reference borosilicate glass developed at Savannah River Laboratory.

Results

(1) Glass Formation

(a) **Waste Loading:** To determine the maximum waste loading in the iron phosphate glass wasteform, compositions were prepared with a sludge content of 20, 30, 35 and 40 wt%, and a base iron phosphate composition such that the final wasteform would contain 30 wt% Fe_2O_3 and the remainder P_2O_5 . An Fe_2O_3 content of 30 wt% was selected since measurements^{11,14,15} of the dissolution rate for numerous other iron phosphate glasses indicated such a wasteform should form a glass with a good chemical durability.

After the bars were cast and annealed, they were inspected visually to determine if they were glassy or crystallized (Tables II to V). Those compositions that formed a glass ranged in appearance from opaque black to samples with a thin (microns) metallic-looking blue, green, or gold-colored surface that was removed by grinding. This thin metallic-looking surface has been observed in other sludge containing iron phosphate¹¹ and borosilicate glasses¹⁶, although the cause of this layer is still unknown. When the metallic-looking surface was removed, the interior was opaque black and looked identical to the interior of those glasses without the metallic-looking surface.

All of the compositions containing up to 35 wt% sludge formed a glass except for the wasteforms containing more than 20 wt% of the C-106 sludge, see Tables II to V. At a wasteloading of 40 wt%, all the wasteforms crystallized upon cooling.

To achieve higher waste loadings, the Fe_2O_3 content was lowered to 10 wt%

although wasteforms with only 10 wt% Fe_2O_3 were anticipated to have a somewhat lower chemical durability. Batches were prepared with a sludge content of 40, 50, and 60 wt% and an iron phosphate base composition such that the final wasteform would contain 10 wt% Fe_2O_3 and the remainder being P_2O_5 . Ten wt% Fe_2O_3 was exceeded for sludges B-110 and T-111 due to the high Fe_2O_3 content in these sludges (30.6 and 26.3 wt% for B-110 and T-111, respectively) which made it impossible to maintain the Fe_2O_3 content at 10 wt%. For the batches containing 40 wt% or more of the B-110 and T-111 sludges, no additional Fe_2O_3 was added to the batch and the final Fe_2O_3 content is a result of that present in the sludge only.

All of the batches containing 40 and 50 wt% sludge formed a glass when melted, except for the batches containing the C-106 (high Al_2O_3/SiO_2) sludge. When the waste content in the batch was increased to 60 wt%, only the melt containing the C-112 sludge formed a glass, see Tables II to V.

In summary, by lowering the Fe_2O_3 content in the wasteform from 30 to 10 wt% it was possible to produce glassy wasteforms that contained up to 50 wt% of all the sludges except for the C-106 sludge. A glassy wasteform was even made with 60 wt% of the C-112 sludge. All of these glasses were melted at 1150 to 1200°C, for as little as one hour, in high purity, dense alumina crucibles with no noticeable corrosion of the crucible.

(b) Adding CaF_2 to the Batch: The batches containing 20 and 30 wt% sludge plus 7 wt% CaF_2 melted at 1150°C which was approximately 50°C lower than the

corresponding batches made without CaF_2 . The melts made with CaF_2 also appeared noticeably more fluid. All of the annealed bars appeared glassy except for that containing 30 wt% of the C-106 sludge, which also did not form a glass without CaF_2 . The resulting glasses made with CaF_2 ranged in appearance from black opaque to having a thin metallic-looking surface which was essentially the same as those made without using CaF_2 .

(2) Microstructure

The wasteforms containing 30 wt% of the B-110, C-112, and T-111 sludges and those made with CaF_2 were examined by XRD and TEM to determine if the wasteforms were amorphous and homogeneous. XRD analysis of the wasteform containing 30 wt% of the B-110 sludge showed a very small amount of crystalline material present (Figure 3b). TEM identified the crystalline material to be Si-rich. In addition, TEM identified a small amount of phase separation, in the form of droplets 50 to 75 nm in diameter (Figure 3a).

Similarly, when CaF_2 was added to the batches containing 30 wt% of the B-110 sludge, the resulting wasteform had crystalline material present. This material was identified by XRD as being AlPO_4 and cristobalite (Figure 3d). In addition, TEM showed phase separation present in the wasteform containing CaF_2 . The phase separation was in the form of Si-rich droplets 50 to 200 nm in diameter (Figure 3b).

The wasteform containing 30 wt% of the C-112 sludge was completely glassy according to XRD (Figure 4b). TEM analysis also showed a completely glassy

material free of any crystallization or phase separation (Figure 4a).

When CaF_2 was added to the wasteform containing 30 wt% of the C-112 sludge, XRD and TEM analysis showed the presence of crystalline material (Figures 4c and 4d). This material was identified by XRD to be FePO_4 .

Finally, the wasteform containing 30 wt% of the T-111 sludge had a very small amount of crystalline material which was barely detectable by XRD (Figure 5b). When analyzed by TEM, no crystals or phase separation were observed (Figure 5a).

When CaF_2 was added to the batch containing 20 wt% of the T-111 sludge, no crystalline material or phase separation were detected by XRD or TEM (Figures 5c and 5d).

(3) Physical Properties

(a) **Density:** The density of the sludge-containing glass wasteforms ranged from 2.92 to 3.48, see Table VIII. The density increased with increasing waste loading and Fe_2O_3 content. The increase in density is expected because of the large percentage of heavy elements such as UO_2 in the sludge. In addition, Fe_2O_3 and many of the elements present in the waste probably act as modifiers and produce a more densely packed glass structure by occupying interstitial positions in the glass network.

The density of the wasteforms made with 20 and 30 wt% sludge and 7 wt% CaF_2 ranged from 3.18 to 3.36 g/cm^3 (Table IX). The addition of CaF_2 to the glassy wasteforms only increased the density by $\leq 5\%$.

(b) Thermal Properties: The thermal expansion coefficient of the iron phosphate glass wasteforms ranged from 83.8 to $113.2 \times 10^{-7}/^{\circ}\text{C}$ and increased with waste content, see Table VIII. The increase in the thermal expansion coefficient is probably due to an increase in the number of non-bridging oxygen in the glass structure (depolymerization of the PO_4 network) due to the R_2O and RO oxides in the waste which may act like modifiers in the glass.

The dilatometric softening temperature, T_s , ranged from 488 to 569°C and typically decreased with waste loading, see Table VIII. The decrease in softening temperature is also attributed to the presence of modifiers in the glass which cause a weakening of the glass structure.

Glassy wasteforms containing 20 and 30 wt% sludge plus CaF_2 had a significantly higher thermal expansion coefficient and a higher softening temperature, up to 50°C (Table IX). These increases were more significant in the wasteforms containing 30 wt% sludge than in those containing 20 wt% sludge. The thermal expansion coefficient was expected to increase and the softening temperature to decrease with the addition of CaF_2 to the batch because halides are known to break up the phosphate glass network.¹⁷

Differential Thermal Analysis (DTA) curves of the glassy wasteforms containing 20 and 30 wt% sludge were recorded at a heating rate of $5^{\circ}\text{C}/\text{min}$ in a flowing nitrogen atmosphere (Figures 6 to 9). The crystallization temperature, T_c , of the glassy wasteforms was taken as the first exothermic peak and ranged from 590 to

622°C for the glassy wasteforms. The T_c changed very little (only 10 to 20°C) as the sludge content increased from 20 to 30 wt% (Table VIII).

Adding CaF_2 to the glassy wasteforms made the exothermic crystallization peaks sharper and more intense (Figures 6 to 9). This may be due to the presence of crystalline compounds and phase separation acting as nucleation sites. In addition, the crystallization temperature increased from about 7 to 61°C when the sludge containing wasteforms were made with CaF_2 (Table IX). This increase in crystallization temperature may be beneficial if the sludge containing wasteform remains at an elevated temperature during storage due to the decay of radioactive species.

(4) Chemical Durability

(a) **Dissolution Rate-Glassy Wasteform:** The dissolution rate of the glassy wasteforms containing 30 wt% Fe_2O_3 ranged from 3.1×10^{-8} to 1.8×10^{-9} g/cm²/min (in distilled water at 90°C for 16 days), see Table X. This dissolution rate is lower than or equal to the dissolution rate of three borosilicate HLW glasses, the CVS-IS, R7T7, and DWPF-EA glasses¹⁸, measured in a similar manner.

When the Fe_2O_3 content in the glassy wasteform was decreased to 10 wt%, the wasteforms containing 40 and 50 wt% of the B-110 sludge were heavily corroded after 16 days at 90°C in distilled water (Figure 11). After 16 days in distilled water, these glasses formed a flaky white layer on the surface that crumbled easily and made weighing difficult. Glasses containing 40 and 50 wt% of the T-111 sludge were

more durable than those containing the B-110 sludge, but were still less durable than the borosilicate HLW glasses ($D_R \sim 10^{-6} \text{ g/cm}^2/\text{min}$), see Figure 13.

On the other hand, the dissolution rate of the glassy wasteforms containing 40, 50, and 60 wt% of the C-112 sludge ranged from 3.5×10^{-8} to $8.1 \times 10^{-9} \text{ g/cm}^2/\text{min}$ (Figure 12) which is approximately equal to the dissolution rate of the borosilicate HLW glasses. It should be stressed that the C-112 wasteforms have dissolution rates as good as, or better than that of borosilicate glasses at waste loadings (up to 60 wt%) that are much higher than can be used in borosilicate glasses (~15 wt%).

(b) **Dissolution Rate-Crystallized Wasteform:** Selected wasteforms were crystallized by heating at $5^\circ\text{C}/\text{min}$ to temperatures between 600 and 750°C and holding for 24 hours. The dissolution rate of the crystallized wasteform was measured and compared to the dissolution rate of its corresponding glassy wasteform.

No general trend in dissolution rates for the glassy and crystallized wasteforms at low (20 and 30 wt%) waste loadings is obvious in Table X. In three of the seven wasteforms there was either a slight decrease or no change in dissolution rate after crystallization. The crystallized wasteforms containing 30 wt% of the C-112 and T-111 sludge showed a slight weight gain after 16 days which may be due to the reprecipitation of dissolved material onto the surface of the sample or the formation of a hydrated layer on the surface.

The dissolution rate of the crystallized wasteform containing 20 wt% of the B-110 sludge was the same as that of the glassy wasteform after 16 days in solution.

The remaining four crystallized wasteforms (containing 20 wt% C-106, C-112, T-111 and 30 wt% B-110 sludges) had a higher dissolution rate (up to 100 times) than their corresponding glassy wasteform.

The wasteforms containing larger sludge concentrations (35 to 50 wt%) all showed a significant decrease in the dissolution rate after crystallization (Figure 14). In fact, two of the crystallized wasteforms showed a small increase in weight after exposure to distilled water for 16 days at 90°C due to the reprecipitation of materials on the surface of the glass or the formation of a hydrated surface layer.

(c) **Dissolution Rate-Wasteforms made with CaF_2 :** The generally beneficial effect which CaF_2 has on the dissolution rate of the glassy and crystalline wasteforms is apparent from the values in parentheses in Table X. The improvement in the durability with CaF_2 addition is most evident in those glasses containing 30 wt% sludge. When CaF_2 was used in the batch, the dissolution rate of the wasteforms containing 20 wt% sludge was higher than those wasteforms made with no CaF_2 , while the dissolution rate of the wasteforms containing 30 wt% sludge was lower than those wasteforms made with no CaF_2 .

In addition, adding CaF_2 to the batch tended to decrease the dissolution rate of the glassy wasteforms in NH_4OH (pH 12) solutions (Figures 15-17). Many of the glasses containing 30 wt% sludge immersed in pH 12 NH_4OH were totally dissolved in less than 16 days, but when 7 wt% CaF_2 was added, all the glasses were still intact after 16 days.

The wasteforms made with CaF_2 were crystallized by heating at $5^\circ\text{C}/\text{min}$ to between 650 and 750°C and holding for 24 hours. The dissolution rate of all of the crystallized wasteforms made with CaF_2 was $\sim 10^{-9} \text{ g/cm}^2/\text{min}$ at 90°C in distilled water for up to 16 days. In one case, the sample gained a small amount of weight after immersion in distilled water. In only one case (C-112 sludge 30 wt% waste) did the dissolution rate increase slightly (from 2.8 to $7.9 \times 10^{-9} \text{ g/cm}^2/\text{min}$) after the sample was crystallized. The improvement in the durability with CaF_2 addition was most evident in the crystallized wasteform containing 30 wt% of the various sludges. Adding CaF_2 to all of the wasteforms (except the wasteform containing 30 wt% of the C-112 sludge), decreased the dissolution rate of the crystallized wasteforms (Table X).

In summary, adding CaF_2 to the batch improved the chemical durability of all of the crystallized wasteforms and glassy wasteforms containing 30 wt% sludge. Since adding CaF_2 to the batch lowers the melting temperature by up to 50°C , lowers the melt viscosity, and improves the chemical durability, small batch additions (up to 10 wt%) of CaF_2 is considered beneficial.

(d) Compositional Analysis of Glass Surface: Although the dissolution rate of many of the wasteforms was very small ($10^{-9} \text{ g/cm}^2/\text{min}$), it was essential to determine what reactions were occurring at the surface of the glass when exposed to different solutions. For this reason, the average chemical composition of the glass surface exposed to solution and the interior glass composition were measured by

EDS, see Tables XI to XV. In addition, SEM was used to observe the corroded surface of the glassy wasteforms.

In HCl (pH 2) and NH_4OH (pH 12) solutions, the glassy wasteform containing the 20 wt% of the C-106 sludge had an exposed surface composition that was almost identical to the original, unexposed glass composition, Table XI. This indicates that the small amount of dissolution occurring in this glass is occurring uniformly. Uniform dissolution was assumed since there is no evidence of selective leaching or the formation of a surface layer.

On the other hand, when the wasteform containing 20 wt% of the C-106 sludge was exposed to distilled water, the surface was found to be higher in iron and lower in P_2O_5 and Na_2O than the original glass. This suggests that an iron rich surface layer is forming on the exposed glass surface. This iron rich surface layer may be due to the reprecipitation of iron compounds since many iron compounds have a very low solubility in distilled water¹⁷.

The glassy wasteform containing 20 wt% of the B-110 sludge, Table XII, was totally dissolved in less than 16 days in the NH_4OH (pH 12) solution. EDS measurement of the external surface of the glasses immersed in HCl (pH 2) and distilled water indicate that the small amount of dissolution is occurring uniformly since the composition of the exposed surface is similar to the original, unexposed surface.

The glassy wasteform containing 20 wt% of the C-112 sludge, which was high

in UO_2 , Table XIII, was completely dissolved in less than 16 days in NH_4OH (pH 12) solution. EDS measurements of the surface of the glasses immersed in both HCl (pH 2) and distilled water suggests the formation of an iron rich surface layer due to the slightly higher iron content of the surface of the glass compared to the interior.

The glassy wasteform containing 20 wt% of the T-111 sludge, XIV, appeared to dissolve uniformly in distilled water and NH_4OH , but possibly formed an iron rich surface layer when immersed in HCl.

In addition to the wasteforms containing 20 wt% sludge, the surface of wasteforms made with 35 wt% of the B-110 and T-111 sludges and 50 wt% of the C-112 sludge, corroded in distilled water, was analyzed by EDS (Table XV). Like the wasteforms containing 20 wt% sludge, these wasteforms also corroded uniformly or had a surface high in Fe_2O_3 .

The exposed surface of the wasteforms was observed using SEM to determine if evidence of a surface layer could be found. The majority of the samples that had an exposed surface high in Fe_2O_3 were found to have either particles deposited on the exposed surface of the glass or what appeared to be a cracked surface layer (Figure 18).

In summary, the sludge containing iron phosphate glasses typically exhibit a poor chemical durability in basic solutions, but in neutral to acidic solutions, the durability is much higher, as good as borosilicate HLW glasses. In this pH range, corrosion is either uniform or leads to the formation of an iron rich surface layer

which may act to slow dissolution over time.

(e) PCT: At the completion of the PCT test (seven days in distilled water at 90°C), the leachate was filtered, then analyzed by ICP-ES to determine what species were present in solution. Figure 19 shows the concentration of various elements found in solution. The major components leached from the sludge-containing wasteforms are P, Na, Si, Ca, and Al. This is expected because these elements are present in large concentrations in all of the wasteforms. Note, that although Fe_2O_3 is present in large concentrations as well, very little was detected in the leachate solutions.

While there are measurable concentrations of P, Na, Si, Ca, Al, and Fe in the leachate, it should be stressed that the dissolution rate of the iron phosphate wasteforms is exceptionally low. Table 20 compares the iron phosphate wasteforms to a reference borosilicate glass (ARM-1) used at Savannah River Laboratory. The iron phosphate glasses have a total release into distilled water of only approximately 10 to 20 mg/L which is about one tenth that of the ARM-1 reference glass (200 mg/L).

The dissolution rate of the wasteforms made with CaF_2 were compared to the wasteforms made with no CaF_2 to determine the effect CaF_2 has on the durability of the wasteforms. As Figure 19 shows, adding CaF_2 to a the wasteform decreases the concentrations of P, Na, and Si released into solution, although the total amount of Ca released into solution was increased due to a larger amount of Ca present in the

glass.

Finally, at the conclusion of the PCT test, the pH of the leachate solutions were measured and compared to the pH of a blank (a vessel containing only distilled water). Figure 21 shows that the pH of the iron phosphate glasses stays relative constant while the ARM-1 reference glass has a much higher final pH (~ 10). This is due to a buffering effect that occurs during the dissolution of the iron phosphate glass which is partly responsible for their low dissolution rate.

Discussion

(1) Glass Formation

(a) **Wasteloading:** The four sludges listed in Table I were chosen because their composition indicated that they may be poorly suited for vitrification in a borosilicate glass. The high concentrations of Fe_2O_3 , Bi_2O_3 , UO_2 , and P_2O_5 are likely to limit the solubility of these sludges in a borosilicate glass.⁵

Figure 22 demonstrates the importance of waste solubility on the volume and mass of the final wasteform. Assuming the concentration of P_2O_5 in borosilicate glass must not exceed 2.5 wt%, then only 17.7 wt% of the C-112 sludge could be incorporated into a borosilicate wasteform. On the other hand, four times as much of the C-112 sludge (60 wt%) can be vitrified in an iron phosphate wasteform.

When the densities of the borosilicate (2.75 g/cm^3) and iron phosphate glasses (3.29 g/cm^3) are taken into account, the total volume of each wasteform that would contain one metric ton of the C-112 sludge can be calculated (Figure 22). The total volume of a borosilicate wasteform containing one ton of sludge would be four times larger than the volume of an iron phosphate wasteform. This means that the amount of space needed to store the wasteform is four times less if an iron phosphate glass is used instead of a borosilicate glass.

In addition to a larger wasteform volume, a considerably larger mass of other materials (SiO_2 , B_2O_3 , Na_2O , and others) must be added to form a borosilicate glassy wasteform compared to the iron phosphate wasteform. To vitrify one ton of the C-

112 sludge in a borosilicate glass, 4.6 tons of other glass forming material must be added, while only less than one ton (700kg) of Fe_2O_3 and P_2O_5 must be added to vitrify this waste in an iron phosphate wasteform.

Wasteforms in this study were made containing up to 60 wt% sludge which is approximately 3 times more than expected to be vitrified in a borosilicate glass (~20 wt%). Up to 60 wt% of the C-112 sludge, which is rich in UO_2 (30 wt%), was easily vitrified in the iron phosphate wasteform. Uranium, due to its large size, is probably a modifier in the iron phosphate glasses. While up to 18 wt% UO_2 was present in the glass containing 60 wt% of the C-112 sludge, this corresponds to only 8 mol% UO_2 .

The wasteforms made with the C-106 sludge were expected to be the most difficult to form a glass based on their high SiO_2 and Al_2O_3 content. This expectation was based on the low solubility of alumina and silica that has been reported for lead iron phosphate glasses.²⁰ Silica present in phosphate glass tends to cause phase separation due to the competing structural role of $(\text{PO}_4)^{3-}$ and $(\text{SiO}_4)^{4-}$. In fact, although a glass could be formed with 20 wt% C-106 sludge, the wasteform was found to have a small amount of Si-rich phase separation. When large amounts of alumina are present in a phosphate glass, tetrahedally coordinated phosphorus tends to form AlPO_4 clusters.

The B-110 and T-111 sludges were similar in composition except the B-110 sludge contained almost twice as much SiO_2 (23 wt%) as the T-111 sludge (11 wt%).

Both sludges contained large amounts of Bi_2O_3 (30 wt%) and Fe_2O_3 (30 wt%).

Glasses were formed which contained up to 50 wt% of both sludges. Similar to the glass containing the C-106 sludge which contained a large amount of SiO_2 , the glasses containing the B-110 sludge (23 wt% SiO_2) were found to contain a small amount of Si-rich phase separation.

The base iron phosphate compositions used in this study were selected so that the final wasteform had a constant Fe_2O_3 content of 30 wt% at wasteloadings of 20 to 35 wt%. Thirty weight percent Fe_2O_3 was used because past studies showed that this produced a glass with a good chemical durability.^{11,14,15} At this high iron content, glasses could not be formed containing more than 35 wt% sludge possibly due to the low P_2O_5 (glass former) content (37.2 to 42.9 wt%). Lowering the Fe_2O_3 content to 10 wt% allowed glasses to be formed containing up to 60 wt% sludge.

A study by Day et al.¹¹ discussed the dependence of glass formation of iron phosphate wasteforms on the overall O/P ratio. Glass formation was observed when the O/P ratio of the wasteform was <4.1 . Above an O/P ratio of 4.1 glass formation was no longer observed. The compositions in the current study followed the same trend in glass formation (Table XVI). When the O/P ratio was less than ~ 4.0 , glasses were formed, but compositions whose O/P ratio was ≥ 4.0 crystallized during cooling.

The O/P ratio of the glass is an indication of the structure of the glass forming network. As the O/P ratio is increased, by adding modifiers for instance, the PO_4

network becomes depolymerized and glass formation becomes more unlikely. For example, pyrophosphate compositions ($O/P = 3.5$) whose structure is made up of P_2O_7 groups, typically form a glass. Increasing the modifier content increases the O/P ratio. At an O/P ratio of 4.0, individual PO_4 groups are ideally present and glass formation becomes difficult.

It should be noted that the O/P ratio in the present study is based on the batch composition of the glass and during melting, this ratio could change. Many studies^{14,15,21} on ferric phosphate glasses have reported a small amount of reduction of Fe^{3+} to Fe^{2+} (~15%) occurs during melting. This means that the final glass would have a slightly smaller O/P ratio than calculated from the batch. When 15% reduction is taken into account for the ferric pyrophosphate composition, the calculated O/P ratio of the glass is 3.45 which is slightly smaller than the O/P ratio calculated from the batch (3.50).

On the other hand, compositions that contain halides could have a slightly higher O/P ratio due to the halide being volatilized and replaced with oxygen. A ferric pyrophosphate glass made with 37.5 wt% SrF_2 has an O/P ratio of 3.32 based on the batch composition but the O/P of the glass becomes 3.86 if it is assumed that all the fluorine is volatilized and replaced by oxygen during melting.

(b) CaF_2 Additions: Although a previous study¹¹ showed adding 7 wt% CaF_2 to an iron phosphate glass wasteform extended the glass forming region, adding CaF_2 to the wasteforms in the present study did not appear to affect glass formation

to a noticeable degree. The wasteform containing 30 wt% of the C-106 sludge did not form a glass with or without the 7 wt% CaF_2 addition. There was, however, a decrease in the melting temperature (50°C) and a noticeable decrease in the melt viscosity with CaF_2 addition as reported by Day et al.¹¹

A decrease in melt temperature and viscosity would be consistent with adding a halide to a phosphate glass. The halide produces non-bridging oxygen which weaken the glass network. This decrease in melt temperature and melt viscosity may be beneficial in terms of processing these glasses. The lowered melt temperature has the obvious cost advantages, but in addition helps reduce volatilization of certain species like Cs. The decreased melt viscosity also has the advantage of lower residence time in a furnace (1-2 hours) compared with borosilicate glasses (>24 hours) and enables the melt to drain more quickly.

Another potential advantage of adding CaF_2 to the batch is that the crystallization behavior of sludges containing CaF_2 is different from glasses not containing CaF_2 . As Figures 6 to 9 show, the 20 and 30 wt% sludge-containing glass wasteforms usually exhibit more than one exothermic crystallization peak, and sometimes as many as 4 or 5. The number of exothermic peaks present may be an indication of the number of species crystallizing from the sample during heat treatment. For nuclear waste disposal applications, a small number of compounds crystallizing from a glass wasteform would be more desirable than many. This is because there is a risk that if many compounds crystallize from the wasteform, one

of the compounds might have a poor chemical durability and reduce the corrosion resistance of the wasteform. If one compound is more soluble than the others, this compound might dissolve and leave a glass with a higher surface area. This would in turn lead to an increase in the dissolution rate of the wasteform. In this study, crystallization of the wasteform did not appear to lower the chemical durability and, in fact, crystallized wasteforms actually had a lower dissolution rate than the glassy wasteforms in many cases. Clearly, there is no reason to assume that the chemical durability of a crystallized iron phosphate wasteform will be inherently inferior to that of a glass wasteform.

(2) Chemical Durability

(a) Dissolution of Iron Phosphate Wasteforms: The chemical durability of a phosphate glass increases dramatically with additions of iron oxide to the batch. This increase in chemical durability has been well documented^{5-8,14,15} and is attributed to the formation of Fe-O-P bonds which are more hydration resistant than P-O-P bonds. In addition to the stronger Fe-O-P bonds, there are two mechanisms that take place during dissolution that help to decrease the dissolution of these glasses in acidic to neutral solutions. These two effects are the self-buffering of the leachate solution and the formation of a chemically protective surface layer. These effects are shown schematically in Figure 24 and are described below.

At the conclusion of the PCT (seven days in distilled water at 90°C), the pH of the leachate solutions were measured. The pH of the iron phosphate leachate solution remained relatively constant (± 1 or 2) compared to the pH of the

borosilicate ARM-1 reference material (pH = 10), see Figure 21. This self-buffering effect exhibited by the iron phosphate glasses is due to two competing reactions that occur as the glass is dissolved. When iron phosphate glass is exposed to neutral or acidic solutions, the P-O-P groups go into solution and form phosphoric acid (H_3PO_4) which results in a decreased pH. At the same time, alkalies, like Na^+ and K^+ , and alkaline earths, like Ca^{2+} and Mg^{2+} , are also released into solution. This occurs through an ion exchange process (i.e. Na^+ is replaced with H_3O^+). This leads to an increase in pH. These competing reactions keep the pH of the solution relatively constant.

This is in contrast to silicate glasses where the solution increases in pH as the glass corrodes due to the release of the alkali ions and the weaker silicic acid. The increased pH leads to an increase in dissolution rate. Silicate glasses exposed to distilled water over time will have an increasing dissolution rate, which is in contrast to the iron phosphate glasses whose dissolution rate decreases with time, as shown in Figure 23.

In addition to the self-buffering effect, the high chemical durability of the iron phosphate glasses may also be attributed to the formation of a chemically protective surface layer. As poorly soluble iron is released into solution, the solution becomes quickly saturated with Fe compounds. The Fe compounds precipitate on the surface of the glass forming a chemically protective layer. The formation of this protective layer acts to slow and eventually stop further dissolution of the glass.

The formation of a chemically protective layer is evident from several results

in the current study. The surface of several of the glassy wasteforms exposed to neutral and acidic solutions had a composition that was higher in iron than the unexposed surface, Tables XI to XV. In addition, the leachate solutions from the PCT on wasteforms containing 20 wt% sludge all had very low concentrations of iron (Figure 19) although there were large concentrations (30 wt%) of Fe_2O_3 in the glass. Finally, Figure 18 shows that SEM analysis of several wasteforms exposed to distilled water or HCl (pH 2) appeared to have a cracked layer on the exposed surface, and/or particles deposited on the surface.

The formation of a chemically protective iron rich layer would be beneficial if these glasses were stored in an environment where water was not quickly replenished. Any water coming in contact with the glass would quickly become saturated with iron causing the formation of an iron rich surface layer that would slow, and could eventually stop the dissolution of the remaining glass wasteform.

(b) O/P ratio: The study by Day et al.¹¹ which proposed the dependence of glass formation on the O/P ratio of sludge containing wasteforms, also correlated chemical durability with O/P ratio. The shaded region in Figure 25, taken from the study by Day, shows that $\log D_R$ decreases with increasing O/P ratio until a O/P ratio of ~3.7 is reached. This minimum is close to the O/P ratio of 3.5 which corresponds to pyrophosphate compositions. At higher O/P ratios, the dissolution rate begins to increase and glass formation is no longer observed for O/P > 4.0.

The $\log D_R$ vs. O/P ratio for the glasses in the present study are plotted in

Figure 25, and did not follow the trend observed previously.¹¹ For example, the glass made with 20 wt% of the T-111 sludge (30 wt% Fe_2O_3) had an O/P ratio of 3.46 and a low $\log D_R$ of -8.74. A glass with a similar O/P ratio (3.54) made with 50 wt% T-111 sludge (13.2 wt% Fe_2O_3) was too corroded to measure after 16 days in distilled water at 90°C.

The majority of the glasses that fell outside of the area determined in the previous study¹¹ were the wasteforms which typically contained less than 10 wt% Fe_2O_3 . Because these glasses had a low Fe content, it was thought there may be a relationship between D_R and O/(P+Fe) or O/(P+Fe+Al). When these values were plotted, no relationship was evident.

Based on the current research and past studies on iron phosphate glasses, chemical durability cannot be predicted based solely on the O/P ratio of the glass. In general it can be said that the chemical durability tends to decrease with increasing sludge content and decreasing Fe_2O_3 content. To maximize the chemical durability of the iron phosphate wasteform, the Fe_2O_3 content of the final composition should be ~ 30 wt%.

(3) Processing Iron Phosphate Wasteforms

The lack of information related to the processing of iron phosphate glasses is one reason they are not considered a primary form for the disposal of nuclear materials. Borosilicate glasses have been melted commercially for >50 years and there is much knowledge about their processing. While many questions still

remain about the iron phosphate glasses, they deserve further attention due to their superior properties, many of which are related to their processing.

Iron phosphate glasses melt at lower temperatures (1100 to 1200°C) than borosilicate glasses (1300°C) and are more fluid at the melting temperature (<5 Poise). In addition, the iron phosphate glasses can be melted in a shorter period of time (1 to 2 hours) compared to borosilicate glasses (>24 hours).

Adding a small amount of CaF_2 to iron phosphate glass may further improve their processability by decreasing the melting temperature (by up to 50°C) and melt viscosity. Although adding CaF_2 to the sludge-containing batches was found, in some cases, to produce a small amount of crystallization, the properties of the final wasteforms were not adversely affected which leads to the conclusion that adding CaF_2 to the batch has an overall beneficial effect.

The iron phosphate glasses in this study were melted in high purity alumina crucibles with no noticeable corrosion of the crucible. Sludge-containing iron phosphate glasses have also been melted in high purity alumina, platinum, fireclay, and kyanite crucibles for up to 3 days with no detectable corrosion of the crucibles. In other work,^{4,20} iron phosphate glasses have been melted in alumina, platinum, zirconia, and Monofrax K-3 with minimal corrosion. A strong argument against the use of iron phosphate glasses has been the corrosiveness of the melt²⁰, which has not been seen in this work.

Iron phosphate glassy wasteforms require that only two components, Fe_2O_3

and P_2O_5 , be added to vitrify the wastestream. For wastestreams high in iron, P_2O_5 would be the only component added. This is compared to the complex borosilicate compositions which may contain up to 15 other components. Additionally, the borosilicate glass forming components are typically added as a previously melted glass powder, or frit. The glass forming components in the iron phosphate wasteform may be added as any convenient source of iron oxide and phosphorus oxide such as Fe_2O_3 , Fe_3O_4 , FeO , P_2O_5 , and $NH_4H_2PO_4$ which eliminates an extra, costly processing step.

Although iron phosphate glasses have not been processed on a large scale for nuclear waste disposal purposes, their processing would be similar to that of the borosilicate glasses. The sludge material would be pretreated in the same way as for a borosilicate wasteform. The proper proportions of iron and phosphorus would be added to the wastestream so the O/P ratio would be ~3.5 which would ensure the formation of a glass. The chemical durability of the wasteform would be optimized if the Fe_2O_3 content in the final wasteform was ~30 wt%. A few percent CaF_2 could be added to decrease melt temperature and viscosity.

The waste and glass forming materials would then be mixed and fed into a melter. The melter used for iron phosphate glass could be a relatively small box furnace made of fireclay, kyanite, or Monofrax K-3. The size of the furnace would be much smaller than that used for borosilicate glasses for the following reasons. Iron phosphate glasses have a:

- (1) shorter melt time requiring less residence time in the furnace

- (2) higher density, leading to a smaller volume of material traveling through the furnace
- (3) lower melt viscosity which leads to faster draining of the melt

The melt would travel through the furnace in ~1 to 2 hours which is at least 12 times faster than the borosilicate glasses. The melt could be continuously drained into a metal canister similar to the borosilicate glasses. If desired, the pour rate could be much faster than with the borosilicate glasses due to the lower melt viscosity.

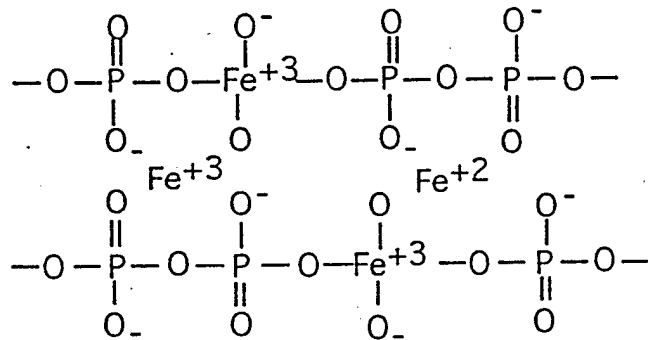
In short, processing of iron phosphate glass would follow the same general steps as processing of borosilicate glasses but with several advantages. More waste could be processed in a shorter amount of time due to shorter melt times, less raw materials are required, and more waste would be immobilized per volume due to higher density and higher wasteloading.

(4) Structure

The structure of iron phosphate glass is not completely understood at this time although considerable research^{6-9,11,14,15} over the past 10 years has contributed much to our understanding. It is well documented that the chemical durability of a phosphate glass increases as Fe_2O_3 is added to the glass, up to four orders of magnitude¹⁴. The structural role of iron in phosphate glass is still being studied. Mossbauer spectroscopic studies^{14,15,21} of ferric pyrophosphate glass ($2Fe_2O_3 \cdot 3P_2O_5$) shows that while iron is added in the form of Fe^{3+} , approximately 10 to 20% is

reduced to Fe^{2+} during melting in air. The Fe^{2+} is present in octahedral coordination while the Fe^{3+} may be found in either octahedral or tetrahedral coordination. Iron (Fe^{2+} or Fe^{3+}) in octahedral coordination is a modifier and improves the chemical durability of the glass by breaking down long P-O-P chains and providing strong crosslinks between non-bridging oxygen. Iron (Fe^{3+}) in tetrahedral coordination (approximately 69% of the total iron in iron pyrophosphate glass) acts as a glass former replacing weak P-O-P bonds with stronger P-O-Fe bonds.

Based on past studies of iron phosphate glass and Mossbauer measurements, a proposed structure of the iron pyrophosphate glass would be as follows.



The sludges which contain large amounts of RO and R_2O compounds are thought to play the role of network modifier in the iron phosphate glasses. This is supported by the increase in thermal expansion coefficient, increase in dissolution rate, and decrease in softening temperature as the sludge content is increased. The RO and R_2O in the sludge are thought to primarily provide weak crosslinks between the iron phosphate groups.

Conclusion

Glassy iron phosphate wasteforms have been made which contain up to 60 wt% of the C-112 sludge, 50 wt% of the B-110 and T-111 sludges, and 20 wt% of the C-106 sludge. All of the glassy wasteforms were melted below 1200°C in 1 hour in high purity alumina crucibles with no noticeable corrosion. Of primary importance, the dissolution rate in distilled water at 90°C of the glassy wasteform containing 60 wt% of the C-112 sludge was equivalent to that of other borosilicate waste glasses. The wasteforms containing up to 35 wt% of the B-110 or T-111 sludge, and 20 wt% of the C-106 sludge also had similar dissolution rates in distilled water at 90°C.

Corroded wasteforms containing 20 wt% sludge were analyzed by EDS and found to either corrode either uniformly or, in several cases, to form a chemically protective surface layer high in Fe_2O_3 . This iron rich surface is suspected to form by the precipitation of iron compounds after the solution becomes saturated. This iron rich surface layer could be highly beneficial in decreasing and eventually stopping the dissolution of the glassy wasteform in closed systems, where the water is not replenished.

When the sludge-containing wasteforms are heat-treated, the dissolution rate of the crystallized wasteform is usually the same as or lower than that of the corresponding glassy wasteform. Exceptions are the wasteforms containing 20 wt% of the C-106, C-112, and T-111 sludges and 30 wt% of the B-110 sludge which had a slightly higher dissolution rate after crystallization.

Wasteforms made from batches containing 7 wt% CaF_2 had a lower melting

temperature (by 50°C) and a higher crystallization temperature, T_c . In addition, the dissolution rate of glassy and crystallized sludge wasteforms is typically decreased 5 to 10 times when CaF_2 is added to the batch (except for the 20 wt% waste loaded glasses and the C-112 30 wt% crystallized wasteform). The crystallization behavior changed with CaF_2 addition (as indicated from the DTA patterns), but the dissolution rate of the crystallized waste form was lower. In addition, the number of compounds crystallizing from the glass is reduced which is considered beneficial for radioactive waste disposal glasses. Overall, we conclude that using CaF_2 in the batch to produce a glassy waste form is beneficial.

References

¹D. L. Illman, "Researchers Take Up Environmental Challenge at Hanford," Chem&Eng., June 21 9-21 (1993).

²H. Matzke and E. Vernaz, "Thermal and Physicochemical Properties Important for the Long Term Behavior of Nuclear Waste Glasses," J. Nuc. Mat., 201 295-309 (1993).

³J. C. Cunnane, J. K. Bates, W. L. Ebert, X. Feng, J. J. Mazer, D. J. Wronkiewicz, J. Sproull, W. L. Bourcier, and B. P. McGrail, "High Level Nuclear-Waste Borosilicate Glass: A Compendium of Characteristics," Mat. Res. Soc. Proc., 294 225-232 (1993).

⁴B. C. Sales and L. A. Boatner, "Physical and Chemical Characteristics of Lead-Iron Phosphate Nuclear Waste Glasses," J. Non-Cryst. Solids, 79 83-116 (1986).

⁵D. R Uhlmann and N. J. Kreidl, Glass Science and Technology, Academic Press, Inc., New York, NY (1983).

⁶B. C. Sales and L. A. Boatner, "Lead-Iron Phosphate Glass: A Stable Storage Medium for High-Level Nuclear Waste," Science, 226 [4607] 45-48 (1984).

⁷B. C. Sales and L. A. Boatner, "Lead Phosphate Glass as a Stable Medium for the Immobilization and Disposal of High-Level Nuclear Waste," Mat. Letters, 2 [4B] 301-304 (1984).

⁸L. Yunfei, Z. Yan, H. Weiwei, L. Kunquan, and Z. Yaqin, "Structural Study of Iron in Phosphate Glasses," J. Non-Cryst. Solids, 112 136-141 (1989).

⁹A. Musinu, G. Piccaluga, and G. Pinna, "Structural Properties of Lead-Iron Phosphate Glasses by X-Ray Diffraction," *J. Non-Cryst. Solids*, **122** 52-58 (1990).

¹⁰Sludge compositions provided by B. Bunker, Pacific Northwest National Laboratory

¹¹D. E. Day, Z. Wu, and C. Ray, "Chemically Durable Glasses for Vitrifying Phosphate Containing Simulated Nuclear Wastes," Final Technical Report for Contract No. 276822-A-F1, Pacific Northwest National Laboratories (1995).

¹²Materials Characterization Center, Nuclear Materials Handbook, DOE/TIC-11400, Pacific Northwest Laboratory, Richland, Washington (1982).

¹³ARM reference material, Savannah River Technology Center

¹⁴X. Yu, D. E. Day, and G. J. Long, "Properties and Structure of Sodium-Iron Phosphate Glasses," submitted to *J. Non-Cryst. Solids*.

¹⁵D. E. Day and A. L. McIntrye, "Study of Phosphate Glasses (Calcium Iron Phosphate)," Final Technical Report for Contract No. AF-0923, Sandia National Laboratories (1994).

¹⁶W. G. Ramsey, personal communications.

¹⁷R. K. Brow, D. R. Tallant, Z. A. Osborne, Y. Yang, and D. E. Day, "The Effect of Fluorine on the Structure of Phosphate Glass," *Phys. Chem. Glasses*, **32** [5] 188-195 (1991).

¹⁸CVS-IS borosilicate HLW glass, Battelle Pacific Northwest Laboratories, R7T7 French LWR borosilicate reference glass, and DWPF-EA Savannah River Laboratory borosilicate HLW reference glass.

¹⁹CRC- Handbook of Chemistry and Physics, ed. D. R. Lide, 75th ed., CRC Press, Inc., Boca Raton, Florida (1995).

²⁰C. M. Jantzen, "Investigation of Lead-Iron-Phosphate Glass for SRP Waste," Advances in Ceramics: Nuclear Waste Management, 20 157-165 (1986).

²¹ K. Tanaka, N. Soga, R. Ota, and K. Hirao, "ESR and Mossbauer Studies of Crystallization Process of Iron Phosphate Glass," Bull. Chem. Soc. Jpn., 59 1079-1085 (1986).

Table I: Simplified Hanford sludge compositions (wt%).

	C-106	B-110	C-112	T-111
Al_2O_3	17.7	2.7	4.2	1.1
BaO	1.2	---	---	---
Bi_2O_3	---	25.8	---	29.8
CaO	---	1.5	16.1	3.4
CuO	3.8	---	---	---
Fe_2O_3	16.8	30.6	15.0	26.3
La_2O_3	---	---	---	5.1
Mn_2O_3	---	---	---	10.4
MgO	2.5	---	---	---
NiO	---	---	9.5	---
PbO	---	---	1.1	---
P_2O_5	1.3	1.7	14.1	3.6
SiO_2	34.7	23.4	2.5	11.3
Na_2O	22.1	14.4	7.1	5.6
UO_2	---	---	30.5	3.3

Table II: Batch composition (wt%) of wasteforms containing the C-106 sludge.

	30 wt% Fe ₂ O ₃						10 wt% Fe ₂ O ₃	
	20%	30%	35%	40%	40%	50%	60%	
Al ₂ O ₃	3.5	5.3	6.2	7.1	7.0	8.8	-----	
BaO	0.2	0.4	0.4	0.5	0.5	0.6	-----	
Bi ₂ O ₃	-----	-----	-----	-----	-----	-----	-----	
CaO	-----	-----	-----	-----	-----	-----	-----	
CuO	0.8	1.1	1.3	1.5	1.5	1.9	-----	
Fe ₂ O ₃	30.0	30.0	30.0	30.0	10.0	10.0	-----	
La ₂ O ₃	-----	-----	-----	-----	-----	-----	-----	
Mn ₂ O ₃	-----	-----	-----	-----	-----	-----	-----	
MgO	0.5	0.7	0.9	1.0	1.0	1.2	-----	
NiO	-----	-----	-----	-----	-----	-----	-----	
PbO	-----	-----	-----	-----	-----	-----	-----	
P ₂ O ₅	53.6	45.4	41.3	37.2	57.2	49.0	-----	
SiO ₂	6.9	10.4	12.1	13.9	13.9	17.3	-----	
Na ₂ O	4.4	6.6	7.7	8.8	8.8	11.0	-----	
UO ₂	-----	-----	-----	-----	-----	-----	-----	
T _m	1200	1200	1300	1250	1150	1200	-----	
results	glass	crystallized	crystallized	crystallized	Phase separated	crystallized	not melted	

Table III: Batch composition (wt%) of wasteforms containing the B-110 sludge.

	30 wt% Fe ₂ O ₃						10 wt% Fe ₂ O ₃		
	20%	30%	35%	40%	40%	50%	60%		
Al ₂ O ₃	0.5	0.8	0.9	1.1	1.1	1.4	1.6		
BaO	----	----	----	----	----	----	----		
Bi ₂ O ₃	5.2	7.7	9.0	10.3	10.3	12.9	15.5		
CaO	0.3	0.4	0.5	0.6	0.6	0.8	0.9		
CuO	----	----	----	----	----	----	----		
Fe ₂ O ₃	30.0	30.0	30.0	30.0	12.2	15.3	18.4		
La ₂ O ₃	----	----	----	----	----	----	----		
Mn ₂ O ₃	----	----	----	----	----	----	----		
MgO	----	----	----	----	----	----	----		
NiO	----	----	----	----	----	----	----		
PbO	----	----	----	----	----	----	----		
P ₂ O ₅	56.5	49.7	46.3	42.9	60.7	50.8	41.0		
SiO ₂	4.5	7.0	8.2	9.4	9.4	11.7	14.0		
Na ₂ O	2.9	4.3	5.0	5.8	5.8	7.2	8.6		
UO ₂	----	----	----	----	----	----	----		
T _m	1100	1200	1200	1250	1050	1150	1250		
results	glass	glass	glass	crystallized	glass	glass	crystallized		

Table IV: Batch composition (wt%) of wasteforms containing the C-112 sludge.

	30 wt% Fe_2O_3			10 wt% Fe_2O_3		
	20%	30%	35%	40%	40%	50%
Al_2O_3	0.8	1.2	1.5	1.7	1.7	2.1
BaO	----	----	----	----	----	----
Bi_2O_3	----	----	----	----	----	----
CaO	3.2	4.8	5.6	6.4	6.4	8.0
CuO	----	----	----	----	----	----
Fe_2O_3	30.0	30.0	30.0	30.0	10.0	10.0
La_2O_3	----	----	----	----	----	----
Mn_2O_3	----	----	----	----	----	----
MgO	----	----	----	----	----	----
NiO	1.9	2.8	3.3	3.8	3.8	4.8
PbO	0.2	0.3	0.4	0.4	0.4	0.6
P_2O_5	55.8	48.7	45.2	41.6	61.6	54.5
SiO_2	0.5	0.8	0.9	1.0	1.0	1.2
Na_2O	1.4	2.1	2.5	2.8	2.8	3.6
UO_2	6.1	9.2	10.7	12.2	12.2	15.2
T_m	1200	1200	1200	1150	1150	1150
results	glass	glass	glass	crystallized	glass	glass

Table V: Batch composition (wt%) of glass wasteforms containing the T-111 sludge.

	30 wt% Fe_2O_3			10 wt% Fe_2O_3		
	20%	30%	35%	40%	40%	50%
Al_2O_3	0.2	0.3	0.4	0.4	0.4	0.6
BaO	----	----	----	----	----	----
Bi_2O_3	6.0	8.9	10.4	11.9	11.9	14.9
CaO	0.7	1.0	1.2	1.4	1.4	1.7
CuO	----	----	----	----	----	----
Fe_2O_3	30.0	30.0	30.0	30.0	10.5	13.2
La_2O_3	1.0	1.5	1.8	2.0	2.0	3.1
Mn_2O_3	2.1	3.1	3.6	4.2	4.2	6.2
MgO	----	----	----	----	----	----
NiO	----	----	----	----	----	----
PbO	----	----	----	----	----	----
P_2O_5	56.0	49.0	45.5	42.1	61.5	51.8
SiO_2	2.3	3.4	4.0	4.5	4.5	5.6
Na_2O	1.1	1.7	2.0	2.2	2.2	2.8
UO_2	0.7	1.0	1.2	1.3	1.3	1.7
T_m	1100	1100	1200	1150	1150	1200
results	glass	glass	glass	crystallized	glass	crystallized

Table VII: Batch composition (wt%) of glass wasteforms made with 30 wt% Hanford sludge and 7 wt% CaF_2 .

	C-106	B-110	C-112	T-111
Al_2O_3	4.9	0.7	1.3	0.3
BaO	0.4	----	----	----
Bi_2O_3	----	7.2	----	8.3
CaO	----	0.4	4.5	1.0
CuO	1.1	----	----	----
Fe_2O_3	27.9	27.9	27.9	27.9
La_2O_3	----	----	----	1.4
Mn_2O_3	----	----	----	2.9
MgO	0.7	----	----	----
NiO	----	----	0.3	----
PbO	----	----	2.6	----
P_2O_5	42.2	46.2	45.3	45.6
SiO_2	9.7	6.5	0.7	3.2
Na_2O	6.2	4.0	2.0	1.6
UO_2	----	----	8.5	0.9
CaF_2	7.0	7.0	7.0	7.0
T_m	1250	1150	1150	1150
results	crystallized	glass	glass	glass

Table VII: Batch composition (wt%) of glass wasteforms made with 30 wt% Hanford sludge and 7 wt% CaF_2 .

	C-106	B-110	C-112	T-111
Al_2O_3	4.9	0.7	1.3	0.3
BaO	0.4	----	----	----
Bi_2O_3	----	7.2	----	8.3
CaO	----	0.4	4.5	1.0
CuO	1.1	----	----	----
Fe_2O_3	27.9	27.9	27.9	27.9
La_2O_3	----	----	----	1.4
Mn_2O_3	----	----	----	2.9
MgO	0.7	----	----	----
NiO	----	----	0.3	----
PbO	----	----	2.6	----
P_2O_5	42.2	46.2	45.3	45.6
SiO_2	9.7	6.5	0.7	3.2
Na_2O	6.2	4.0	2.0	1.6
UO_2	----	----	8.5	0.9
CaF_2	7.0	7.0	7.0	7.0
T_m	1250	1150	1150	1150
results	crystal-lized	glass	glass	glass

Table VIII: Physical properties of iron phosphate glass wasteforms containing up to 60 wt% sludge.

	ρ (g/cm ³) ⁺	T_s (°C) ⁺⁺	α ($\times 10^{-7}$ / °C) ⁺⁺⁺	T_c (°C) ⁺⁺⁺⁺
C-106 sludge				
30% Fe ₂ O ₃				
20% sludge	2.92	488	90.2	618
30% sludge		-----	crystallized	-----
35% sludge		-----	crystallized	-----
10% Fe ₂ O ₃				
40% sludge		-----	phase separated	-----
50% sludge		-----	crystallized	-----
60% sludge	n m	n m	n m	n m
B-110 sludge				
30% Fe ₂ O ₃				
20% sludge	3.05	510	95.4	609
30% sludge	3.19	494	93.0	590
35% sludge	3.19	512	97.6	n m
10% Fe ₂ O ₃				
40% sludge	2.93	512	93.5	n m
50% sludge	3.01	292	101	n m
60% sludge		-----	crystallized	-----
C-112 sludge				
30% Fe ₂ O ₃				
20% sludge	3.10	528	95.4	597
30% sludge	3.35	526	94.0	602
35% sludge	3.48			
10% Fe ₂ O ₃				
40% sludge	3.14	569	86.8	n m
50% sludge	3.16	556	88.9	n m
60% sludge	3.29	558	101.9	n m
T-111 sludge				
30% Fe ₂ O ₃				
20% sludge	3.18	508	85.4	598
30% sludge	3.35	512	99.8	622
35% sludge	3.43	531	113.2	n m
10% Fe ₂ O ₃				
40% sludge	3.12	522	83.8	n m
50% sludge	3.22	510	84.6	n m
60% sludge		-----	crystallized	-----

⁺ = ± 0.05 g/cm³

⁺⁺ = ± 5 °C

⁺⁺⁺ = $\pm 5 \times 10^{-7}$ / °C

⁺⁺⁺⁺ = ± 5 °C

Table IX: Physical properties of iron phosphate glass wasteforms containing 20 or 30 wt% sludge. Data in parenthesis are for wasteforms made with 7 wt% CaF_2 .

	ρ (g/cm ³)	T_s (°C)	$\alpha \times 10^{-7}$ / °C	T_c (°C)
20 wt%				
C-106	2.92 (nm*)	488 (nm)	90.2 (nm)	619 (nm)
B-110	3.05 (3.18)	510 (516)	95.4 (108.2)	608 (624)
C-112	3.10 (3.26)	528 (554)	95.4 (100.2)	598 (659)
T-111	3.18 (3.32)	508 (522)	85.4 (101.0)	598 (638)
30 wt%				
B-110	3.19 (3.18)	494 (542)	93.0 (136.4)	590 (612)
C-112	3.35 (3.36)	526 (571)	94.0 (132.5)	602 (642)
T-111	3.35 (3.31)	512 (547)	99.8 (94.3)	622 (629)

*nm = not made

Table X: Dissolution Rate (D_R) of glassy and crystallized iron phosphate wasteforms containing 20 or 30 wt% of Hanford sludges. D_R measured in distilled water at 90°C for 16 days. Data in parenthesis are for wasteforms made with 7 wt% CaF_2 .

Log D_R (g/cm²/min)
Distilled Water at 90°C for 16 days

	Glass	Crystallized at 800°C for 24 hours
20 wt%		
C-106	-8.12 (nm*)	-7.71 (nm)
B-110	-7.58 (-7.50)	-7.53 (-8.34)
C-112	-8.46 (-8.04)	-6.93 (-8.68)
T-111	-8.74 (-7.38)	-6.74 (-8.68)
30 wt%		
B-110	-7.52 (-8.35)	-6.01 (-8.43)
C-112	-7.75 (-8.56)	(+0.05%) (-8.10)
T-111	-7.88 (-8.97)	(+0.11%) (+ 0.76%)

*nm = not made

Table XI: Batch and EDS analyzed compositions (wt%) of an iron phosphate glass wasteform containing 20 wt% of simulated C-106 sludge after immersion in various solutions at 90°C for 16 days.

	batch**	as-made	HCl (pH2)	H ₂ O (pH7)	NH ₄ OH(pH12)	Composition of External Surface (wt%)*
Al ₂ O ₃	3.5	3.8	3.9	6.0	3.8	
BaO	0.2	n/a	n/a	n/a	n/a	
CuO	0.8	n/a	n/a	n/a	n/a	
Fe ₂ O ₃	30.0	29.4	30.3	43.1	28.0	
MgO	0.5	n/a	n/a	n/a	n/a	
P ₂ O ₅	53.6	54.2	54.6	44.0	56.3	
SiO ₂	6.9	8.0	6.7	5.3	6.8	
Na ₂ O	4.4	4.7	4.6	1.5	5.0	
total	99.9	100.1	100.1	99.9	99.9	

* \pm 3 wt%

** calculated assuming no volatiles in the batch

n/a not analyzed

Table XII: Batch and EDS analyzed compositions (wt%) of an iron phosphate glass wasteform containing 20 wt% of simulated B-110 sludge after immersion in various solutions at 90°C for 16 days.

		Composition of External Surface (wt%)*		
	batch**	as-made	HCl (pH2)	H ₂ O (pH7)
Al ₂ O ₃	0.8	1.3	0.9	1.1
Bi ₂ O ₃	7.7	5.3	6.8	5.9
CaO	0.4	0.2	0.3	0.4
Fe ₂ O ₃	30.0	28.5	27.8	27.7
P ₂ O ₅	49.7	54.9	55.9	56.0
SiO ₂	7.0	6.1	5.5	5.3
Na ₂ O	4.3	3.6	2.7	3.5
total	99.9	99.9	99.9	99.9

* ± 3 wt%

** calculated assuming no volatiles in the batch

---- no sample available for analysis, glass totally corroded

Table XIII: Batch and EDS analyzed compositions (wt%) of an iron phosphate glass wasteform containing 20 wt% of simulated C-112 sludge after immersion in various solutions at 90°C for 16 days.

element	batch**	as-made	HCl (pH2)	H ₂ O (pH7)	NH ₄ OH(pH12)
Al ₂ O ₃	1.2	1.7	2.2	2.4	----
CaO	4.8	2.4	2.4	2.4	----
Fe ₂ O ₃	30.0	29.4	33.4	33.8	----
NiO	2.8	2.1	1.9	1.5	----
PbO	0.3	n/a	n/a	n/a	----
P ₂ O ₅	48.7	56.2	51.9	51.2	----
SiO ₂	0.8	1.0	1.0	1.0	----
Na ₂ O	2.1	2.0	1.4	1.7	----
UO ₂	9.2	5.3	5.8	6.1	----
total	99.9	100.1	100.0	100.1	----

* ± 3 wt%

** calculated assuming no volatiles in the batch

---- no sample available for analysis, glass totally corroded

n/a not analyzed

Table XIV: Batch and EDS analyzed compositions (wt%) of an iron phosphate glass wasteform containing 20 wt% of simulated T-111 sludge after immersion in various solutions at 90°C for 16 days.

element	batch**	as-made	HCl (pH2)	H ₂ O (pH7)	NH ₄ OH(pH12)
Al ₂ O ₃	0.3	1.3	1.7	1.7	0.9
Bi ₂ O ₃	8.9	6.4	9.1	7.5	6.8
CaO	1.0	0.4	0.9	0.5	0.4
Fe ₂ O ₃	30.0	29.2	35.8	31.6	27.7
La ₂ O ₃	1.5	1.0	1.4	1.2	1.0
Mn ₂ O ₃	3.1	2.0	2.1	1.9	1.6
P ₂ O ₅	49.0	53.7	44.4	50.6	57.3
SiO ₂	3.4	3.6	2.4	2.6	2.0
Na ₂ O	1.7	1.6	1.1	1.8	1.8
UO ₂	1.0	0.5	0.9	0.5	0.5
total	99.9	99.7	99.8	99.9	100.0

* ± 3 wt%

** calculated assuming no volatiles in the batch

Table XV: Batch and EDS analyzed compositions (wt%) of an iron phosphate glass wasteform containing 35 wt% of simulated B-110 and T-111 sludges and 50 wt% of the C-112 sludge after immersion in distilled water at 90°C for 16 days.

element	35 wt% B-110			50 wt% C-112			35 wt% T-111		
	batch**	analyzed	H ₂ O (pH 7)	batch**	analyzed	H ₂ O (pH 7)	batch**	analyzed	H ₂ O (pH 7)
Al ₂ O ₃	0.9	0.6	1.2	2.1	2.2	1.6	0.4	0.2	0.8
Bi ₂ O ₃	9.0	8.8	14.1	----	----	----	10.4	8.8	13.1
CaO	0.5	0.6	0.9	8.0	7.2	7.6	1.2	1.6	1.5
Fe ₂ O ₃	30.0	31.2	57.1	10.0	12.1	17.2	30.0	33.9	48.7
La ₂ O ₃	----	----	----	----	----	----	1.8	1.6	2.0
Mn ₂ O ₃	----	----	----	----	----	----	3.6	3.6	3.8
NiO	----	----	----	4.8	6.8	7.1	----	----	----
P ₂ O ₅	46.3	46.5	17.0	54.5	55.9	52.7	45.5	43.7	26.7
PbO	----	----	----	0.4	0.5	0.2	----	----	----
SiO ₂	8.2	7.8	7.7	1.2	0.8	0.3	4.0	2.9	1.4
Na ₂ O	5.0	4.4	1.8	3.6	3.4	3.3	2.0	3.0	2.4
UO ₂	----	----	----	15.2	10.9	9.9	1.2	0.4	1.0
total	99.9	99.9	99.8	99.8	99.8	99.9	100.1	99.7	101.4

* ± 3 wt%

** calculated assuming no volatiles in the batch

Table XVI: O/P ratio of sludge containing wasteforms based on batch composition.

	Waste Loading (wt%)	Fe ₂ O ₃ Content (wt%)	O/P	result
C-106	20	30	3.82	glass
	30	30	4.39	X-tal
	35	30	4.76	X-tal
	40	30	5.21	X-tal
	20	22	3.47	glass
	20	10	3.10	glass
	35	10	3.59	glass
	40	10	3.80	X-tal
	50	10	4.33	X-tal
	20	0	2.94	glass
	30	0	3.25	glass
	35	0	3.44	glass
B-110	40	0	3.66	X-tal
	50	0	4.23	X-tal
	20	30	3.53	glass
	30	30	3.85	glass
	35	30	4.05	glass
	40	30	4.28	X-tal
	40	10	3.37	glass
C-112	50	10	3.80	glass
	60	10	4.43	X-tal
	20	30	3.46	glass
	30	30	3.74	glass
	35	30		glass
	40	30	4.12	X-tal
	40	10	3.16	glass
T-111	50	10	3.37	glass
	60	10	3.66	glass
	20	30	3.47	glass
	30	30	3.76	glass
	35	30	3.94	glass
	40	30	4.14	X-tal
	40	10	3.20	glass

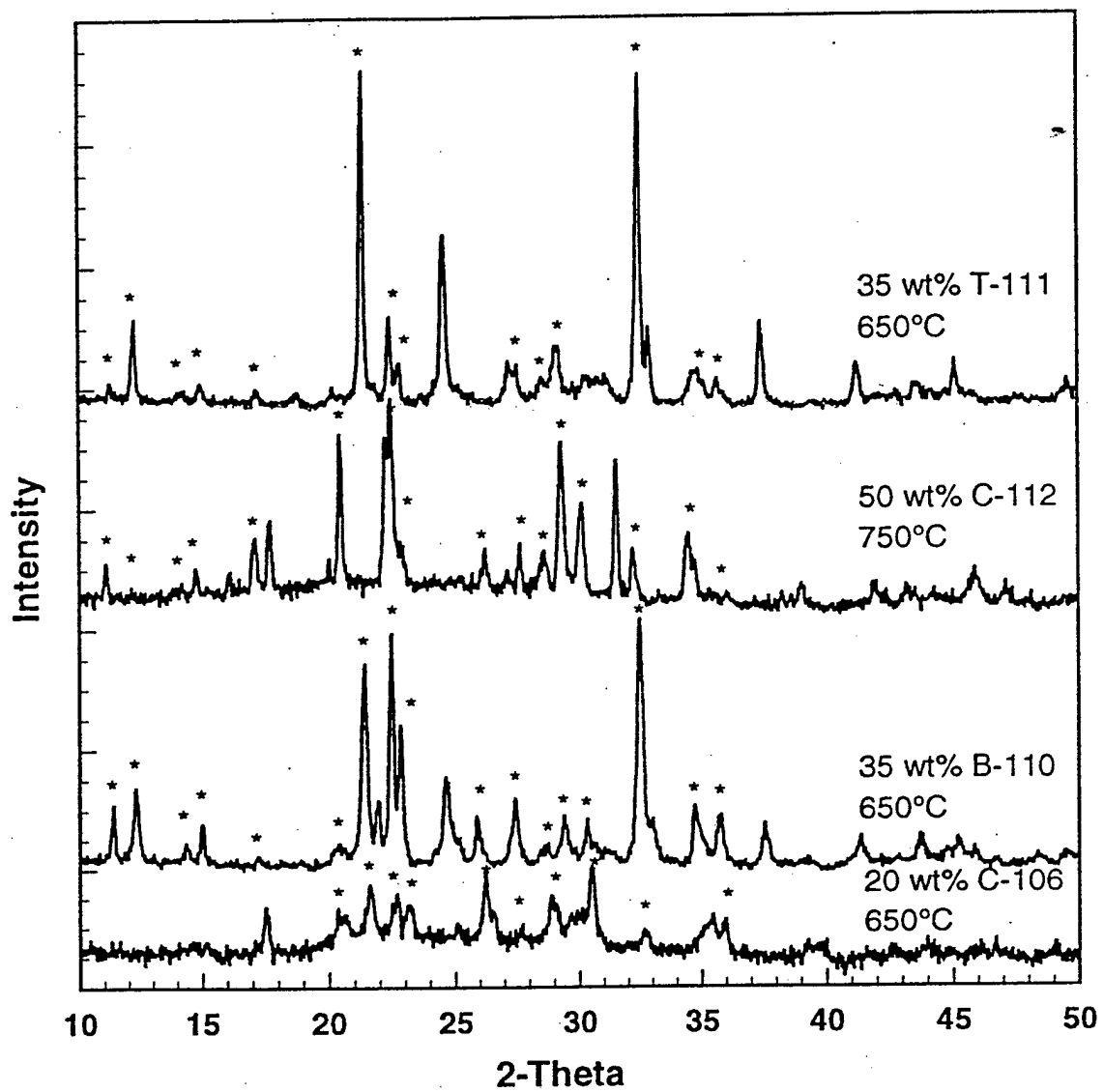


Figure 1: XRD patterns for wasteforms containing 20 wt% of the C-106 sludge, 35 wt% of the B-110 and T-111 sludges, and 50 wt% of the C-112 sludge crystallized at 650 or 750°C. Peaks labeled with a * are common to at least three of the patterns and are assumed to be iron phosphate compounds not listed in the JCPDS card files.

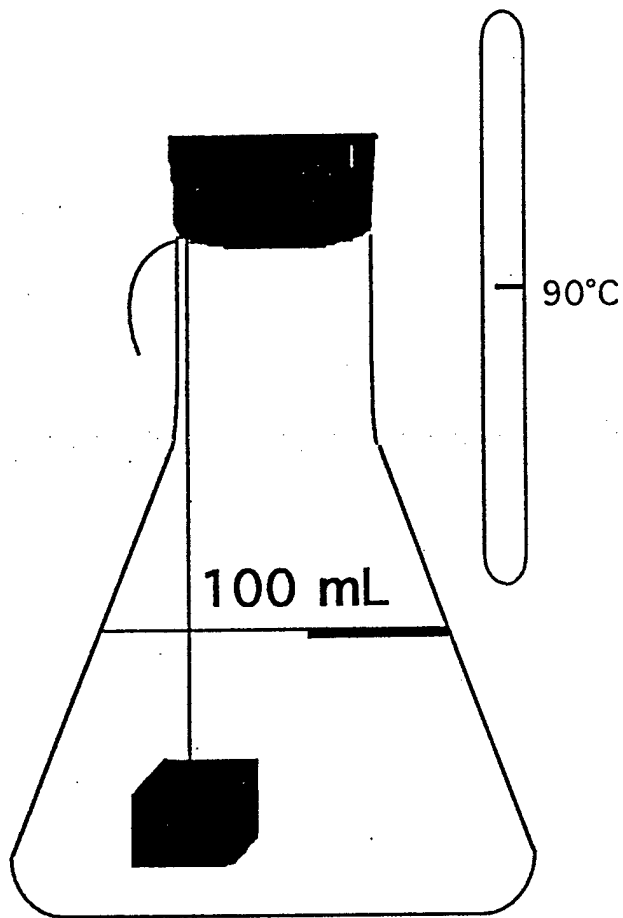


Figure 2: Set-up for measuring the bulk dissolution rate. Sample (~1x1x1 cm) is suspended in 100 mL of distilled water (pH 7), HCl (pH 2), or NH₄OH (pH 12) and placed in an oven at 90°C for up to 16 days.

30 Wt% B-110

30 Wt% B-110 + 7 Wt% CaF₂

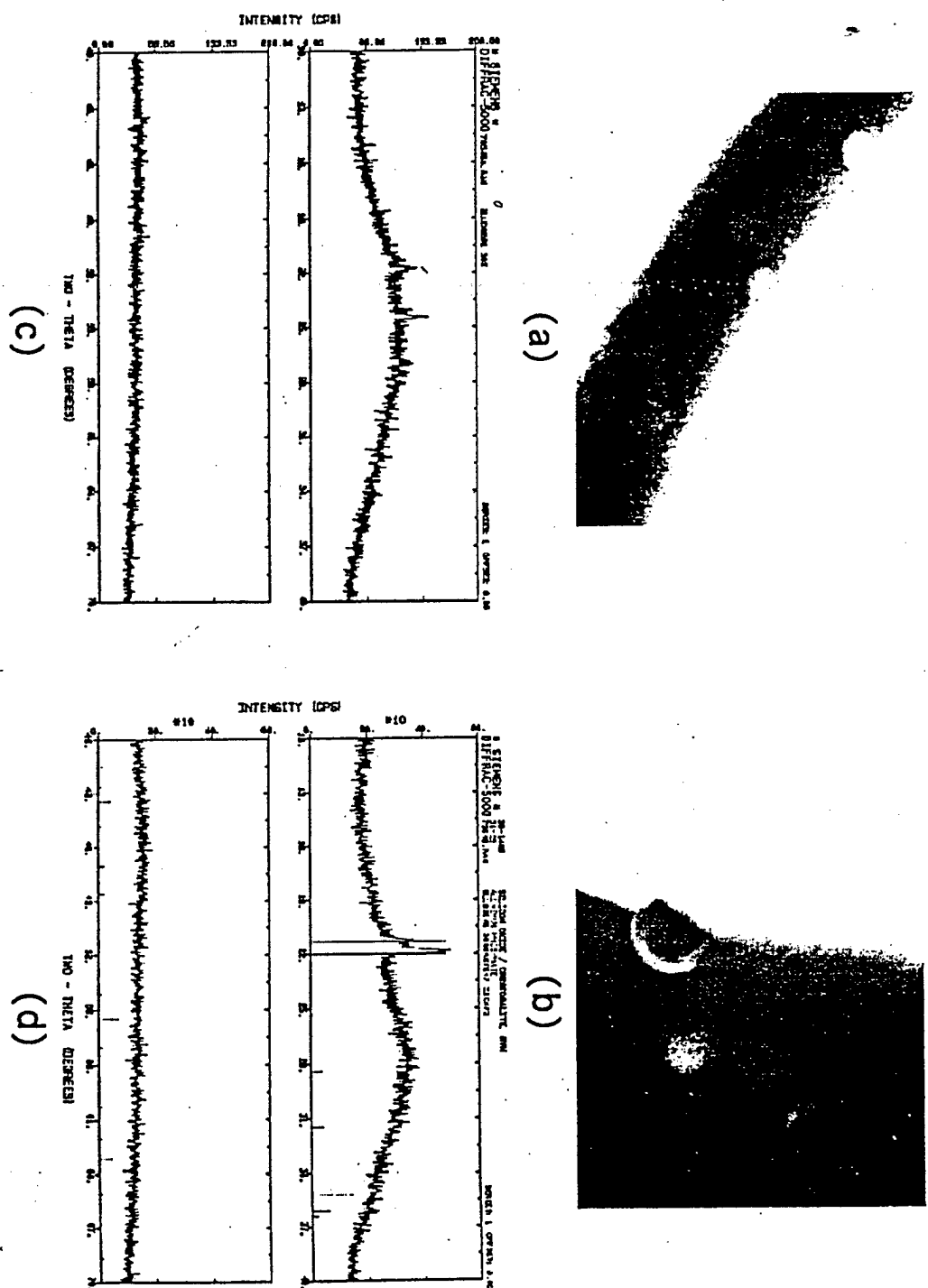


Figure 3: TEM and XRD patterns of wasteforms made with 30 wt% B-110 sludge, and those made with an additional 7 wt% CaF₂.

30 wt% C-112

30 wt% C-112 + 7 wt% CaF₂

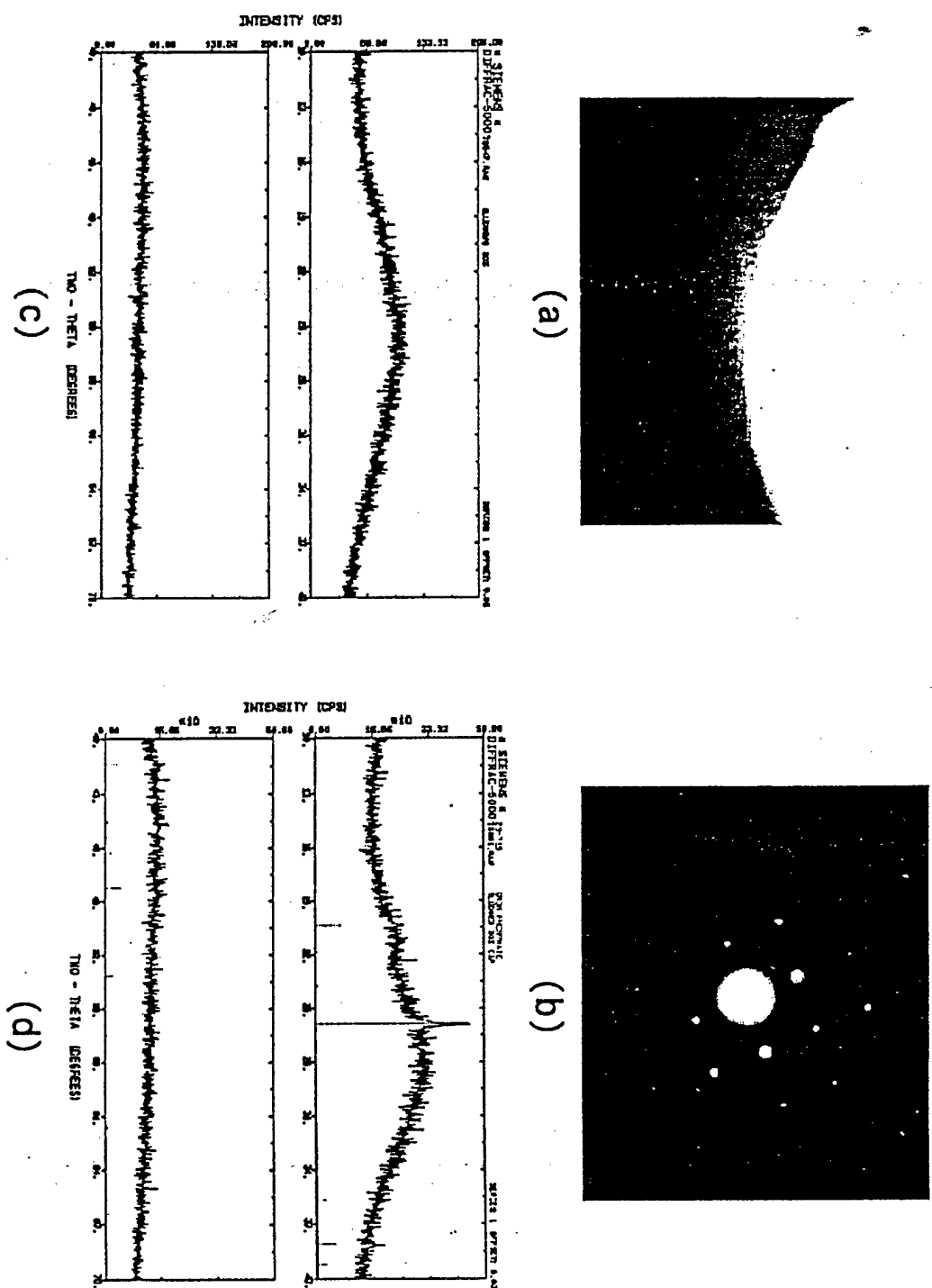


Figure 4: TEM and XRD of wasteforms made with 30 wt% C-112 sludge, and those made with an additional 7 wt% CaF₂.

30 wt% T-111

30 wt% T-111 + 7 wt% CaF₂

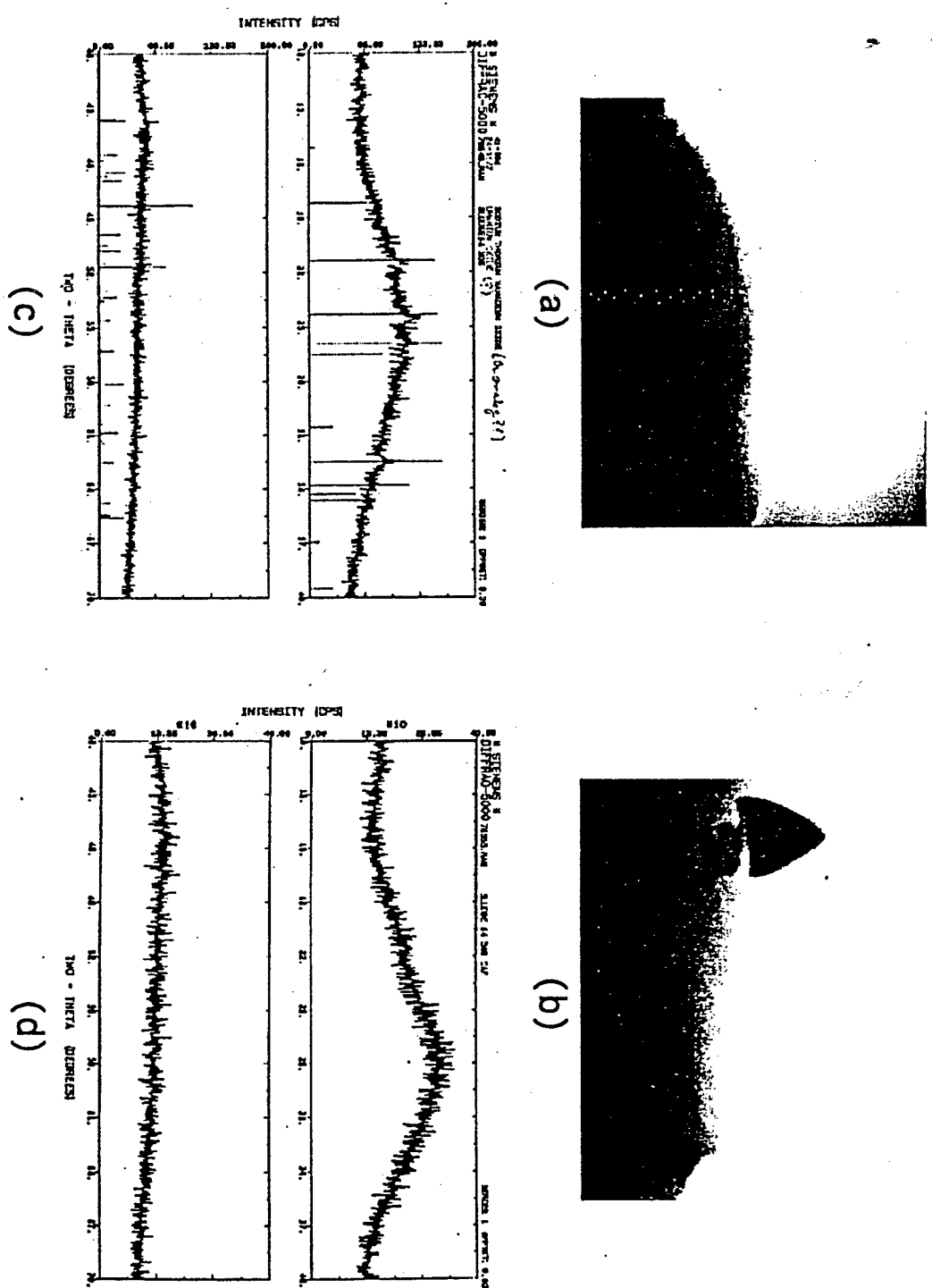


Figure 5: TEM and XRD of wasteforms made with 30 wt% T-111 sludge, and those made with an additional 7 wt% CaF₂.

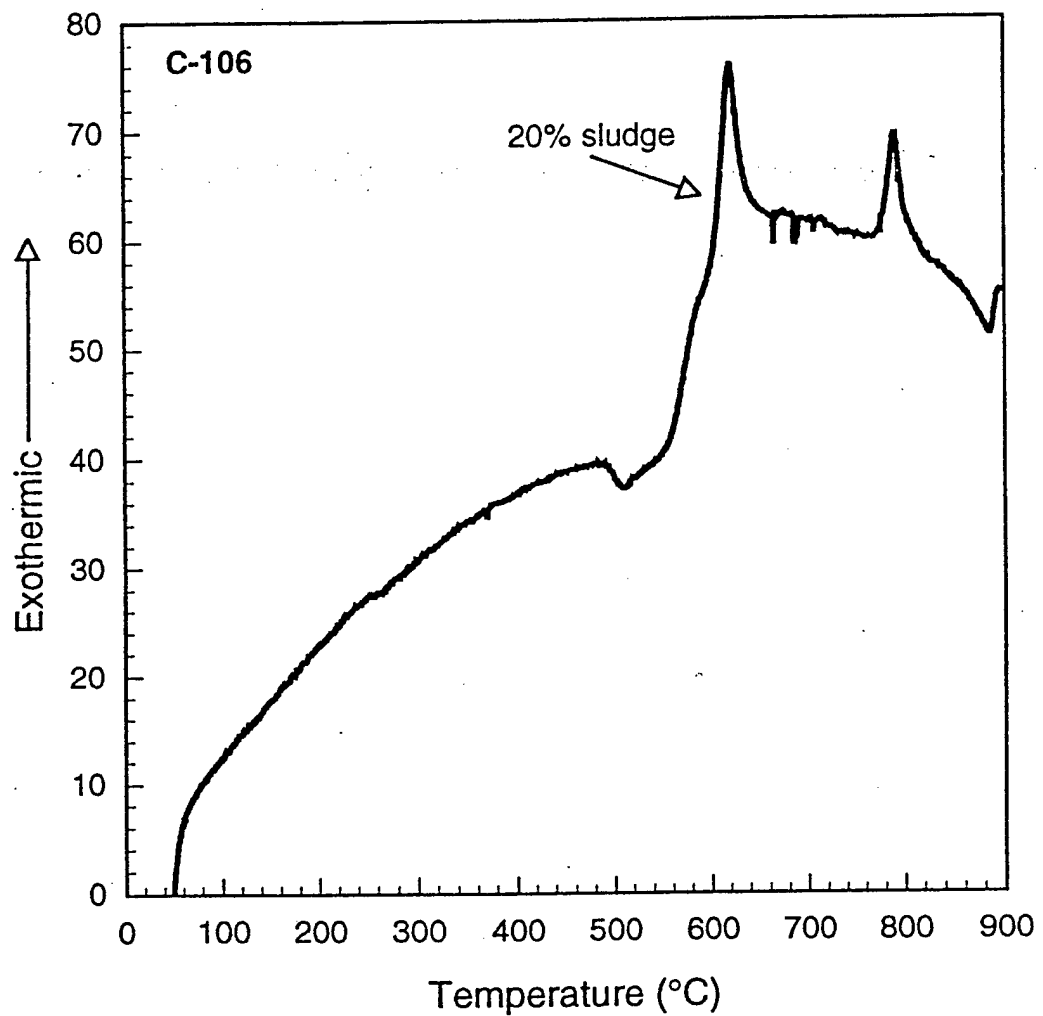


Figure 6: Differential Thermal Analysis curve of an iron phosphate glass wasteform containing 20 wt% of C-106 sludge. This curve and those in Figures 7 thru 9 measured at a heating rate of 5°C/min in a nitrogen atmosphere.

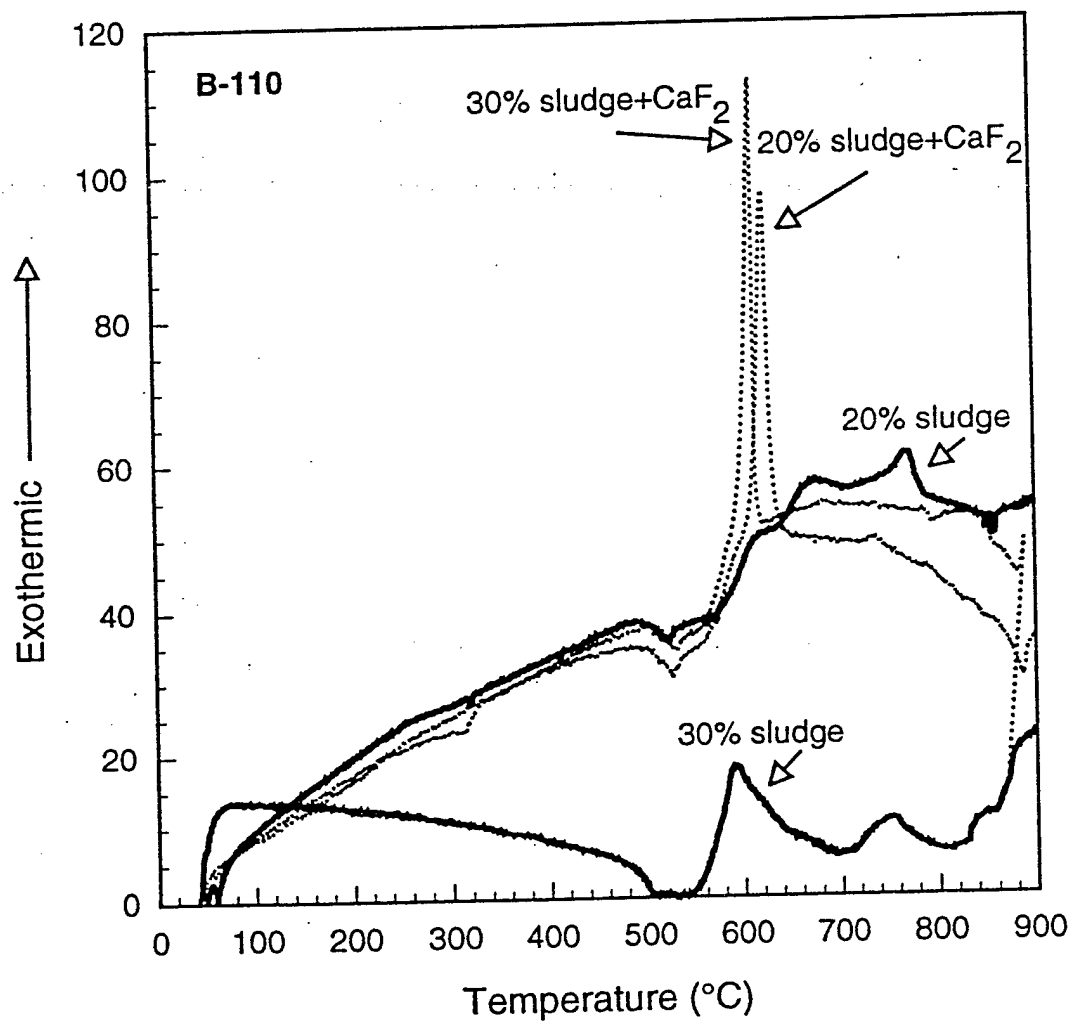


Figure 7: Differential Thermal Analysis curve of an iron phosphate glass wasteform containing 20 and 30 wt% of B-110 sludge. Dotted lines are for glassy wasteforms made with 7 wt% CaF₂.

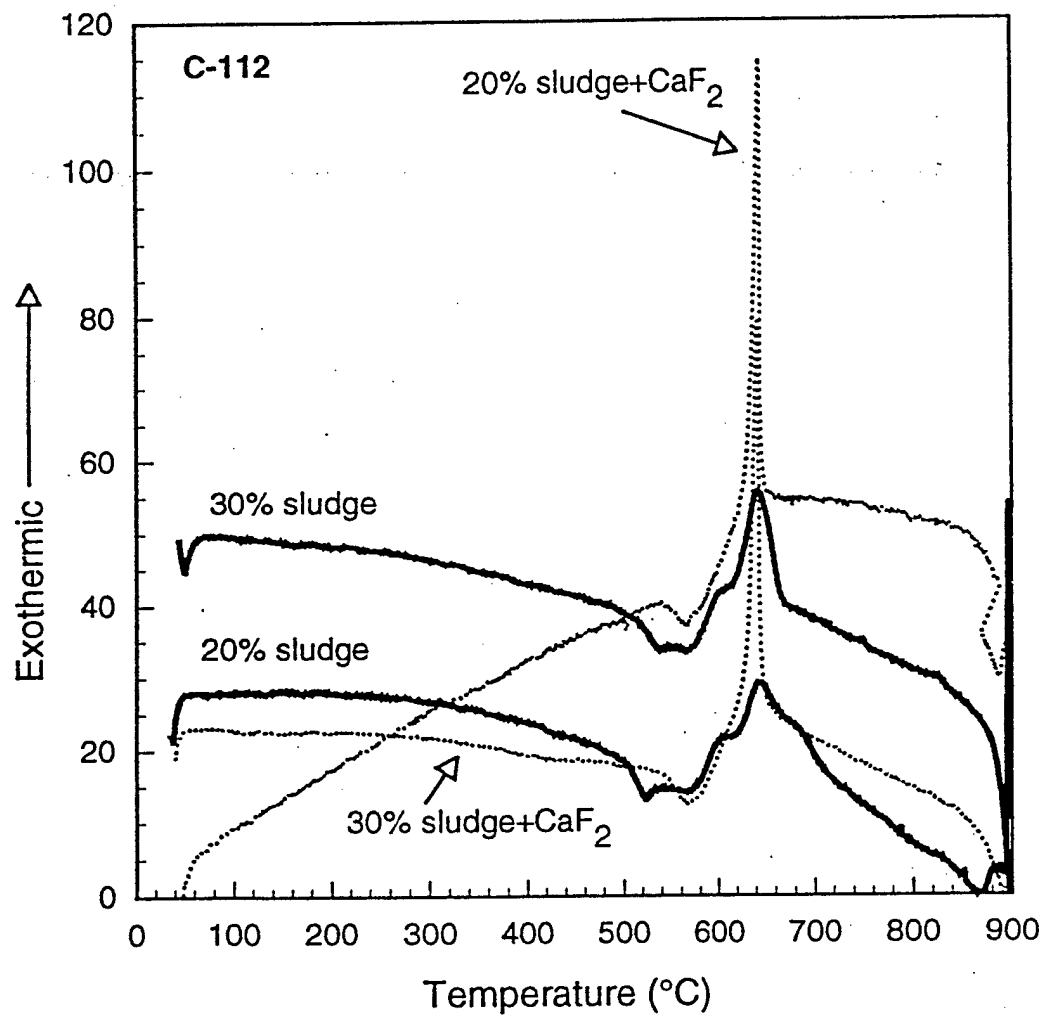


Figure 8: Differential Thermal Analysis curves of an iron phosphate glass wasteform containing 20 and 30 wt% of C-112 sludge. Dotted lines are for glassy wasteforms made with 7 wt% CaF_2 .

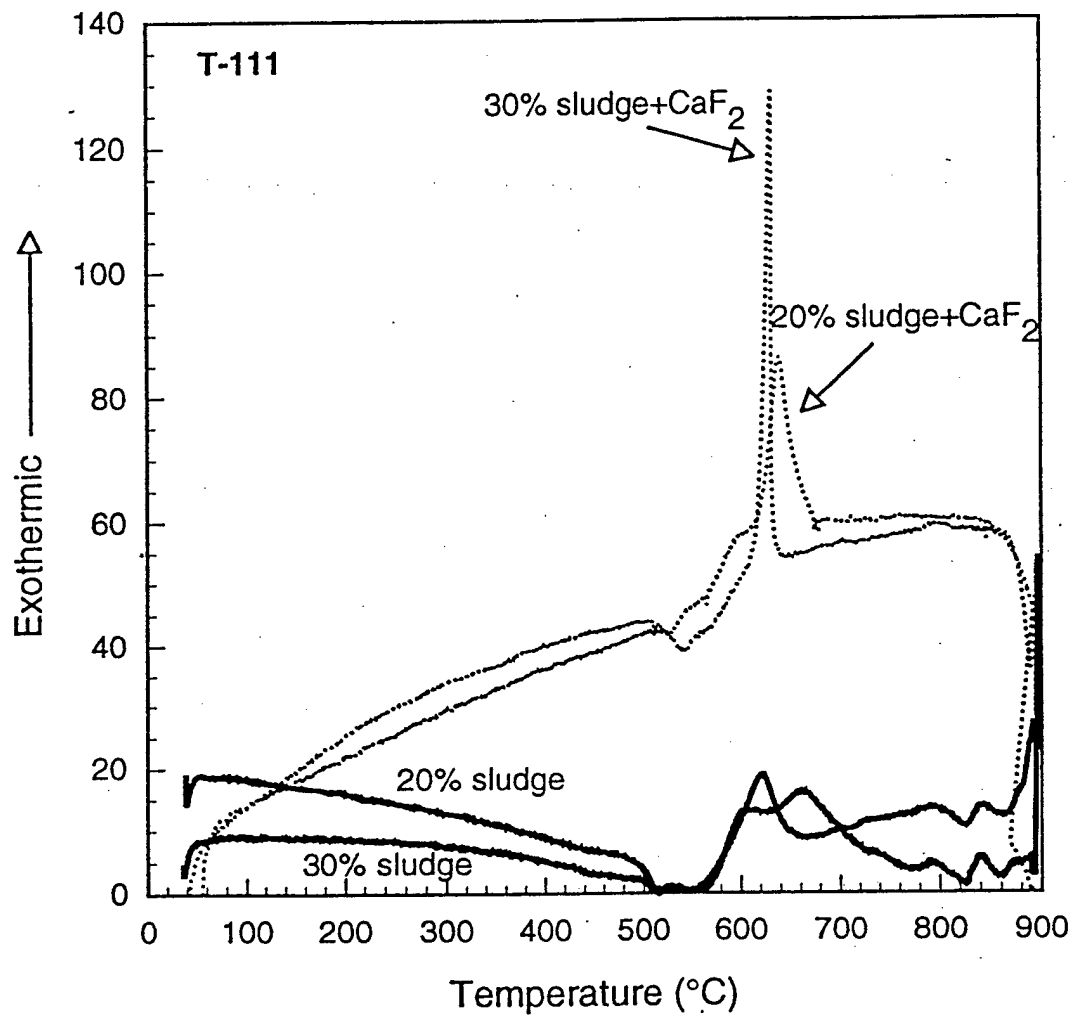


Figure 9: Differential Thermal Analysis curves of an iron phosphate glass wasteform containing 20 and 30 wt% of T-111 sludge. Dotted lines are for glassy wasteforms made with 7 wt% CaF_2 .

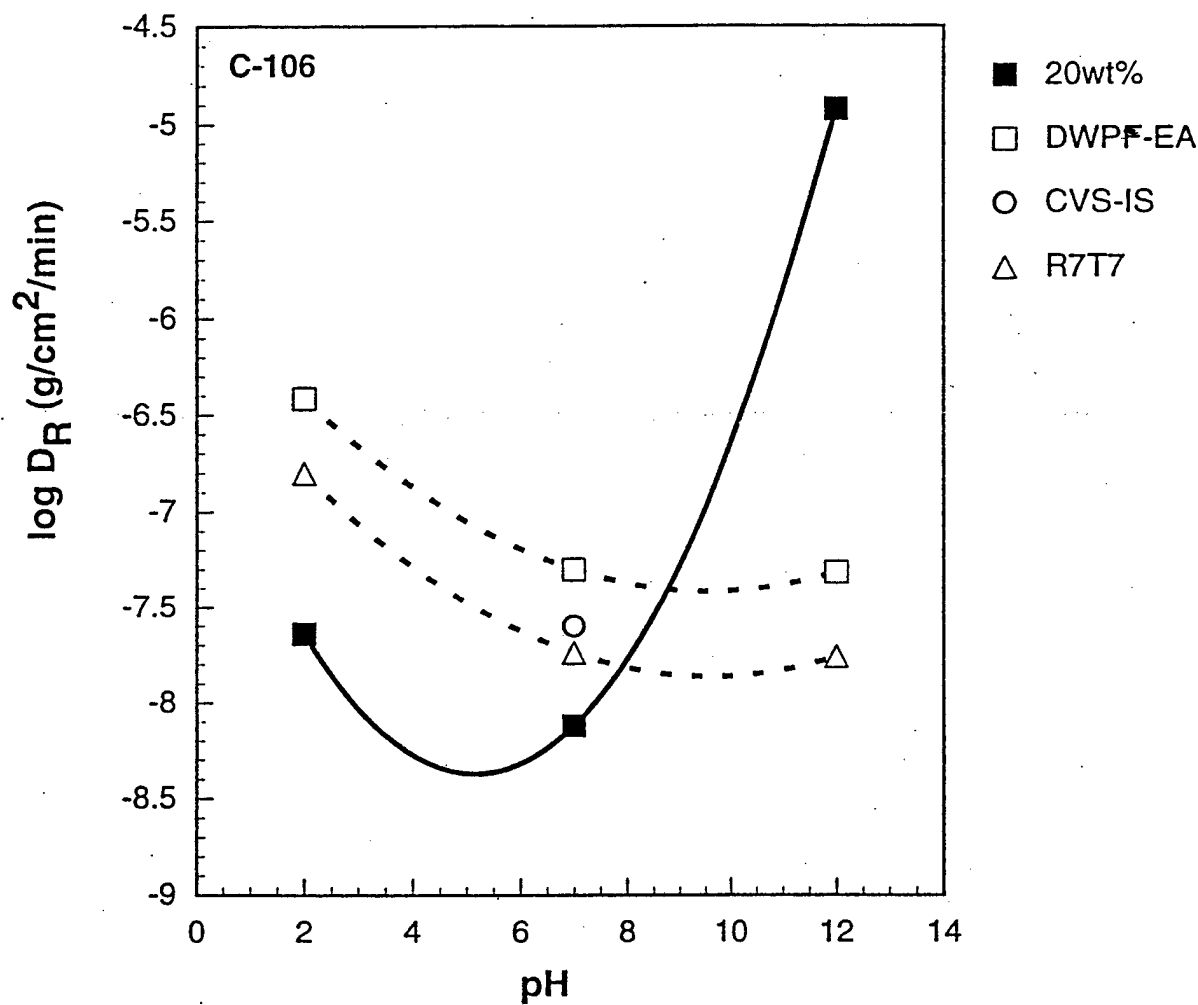


Figure 10: $\log D_R$ ($\text{g}/\text{cm}^2/\text{min}$) of iron phosphate wasteform containing 20 wt% C-106 sludge (solid line, solid symbol) compared to DWPF-EA (SRRL), CVS-IS (PNNL), and R7T7 (France) borosilicate glasses (dashed lines, open symbols). D_R measured in solutions of HCl, distilled water, and NH_4OH for 16 days at 90°C.

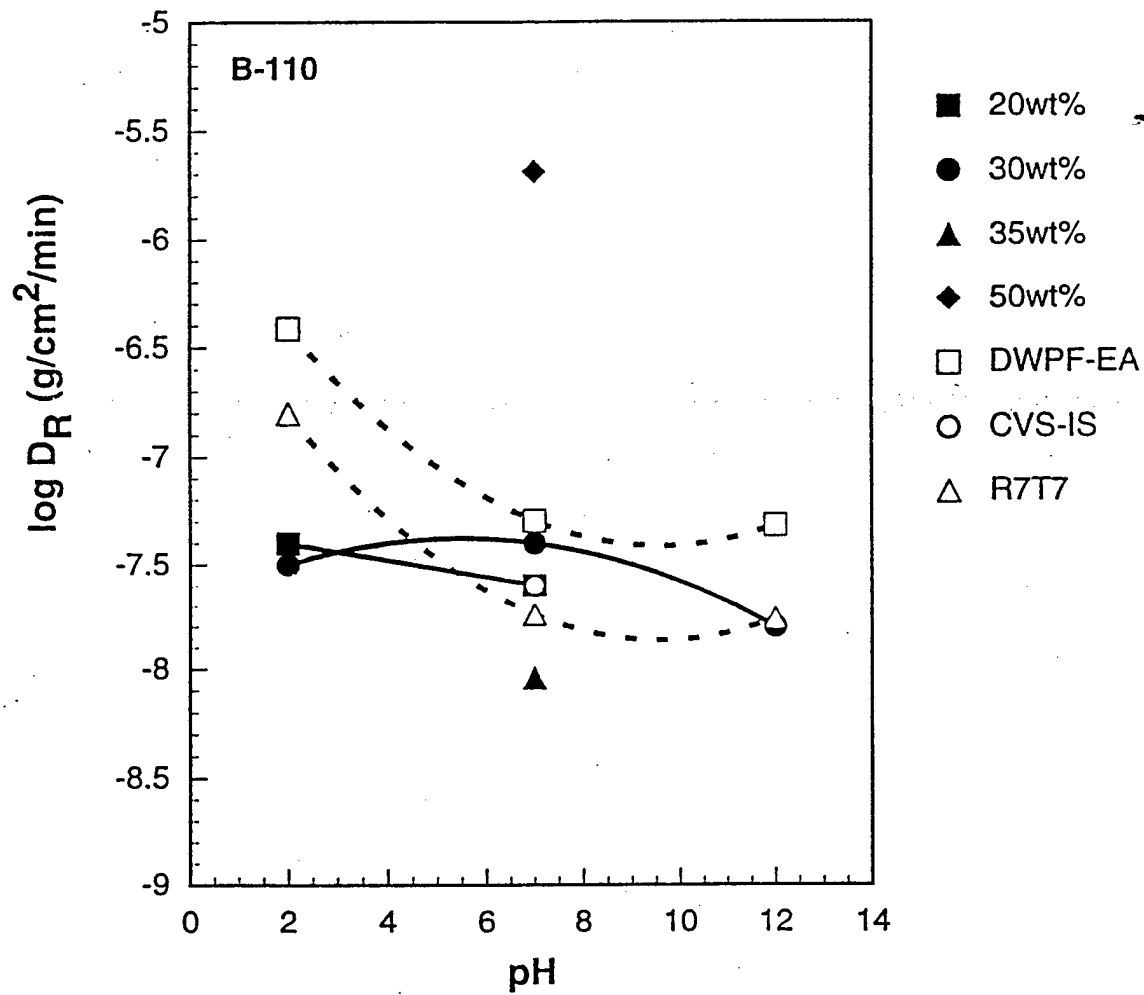


Figure 11: $\log D_R$ ($\text{g}/\text{cm}^2/\text{min}$) of iron phosphate wasteform containing B-110 sludge (solid lines, solid symbols) compared to DWPF-EA (SRL), CVS-IS (PNNL), and R7T7 (France) borosilicate glasses (dashed lines, open symbols). D_R measured in solutions of HCl, distilled water, and NH_4OH for 16 days at 90°C.

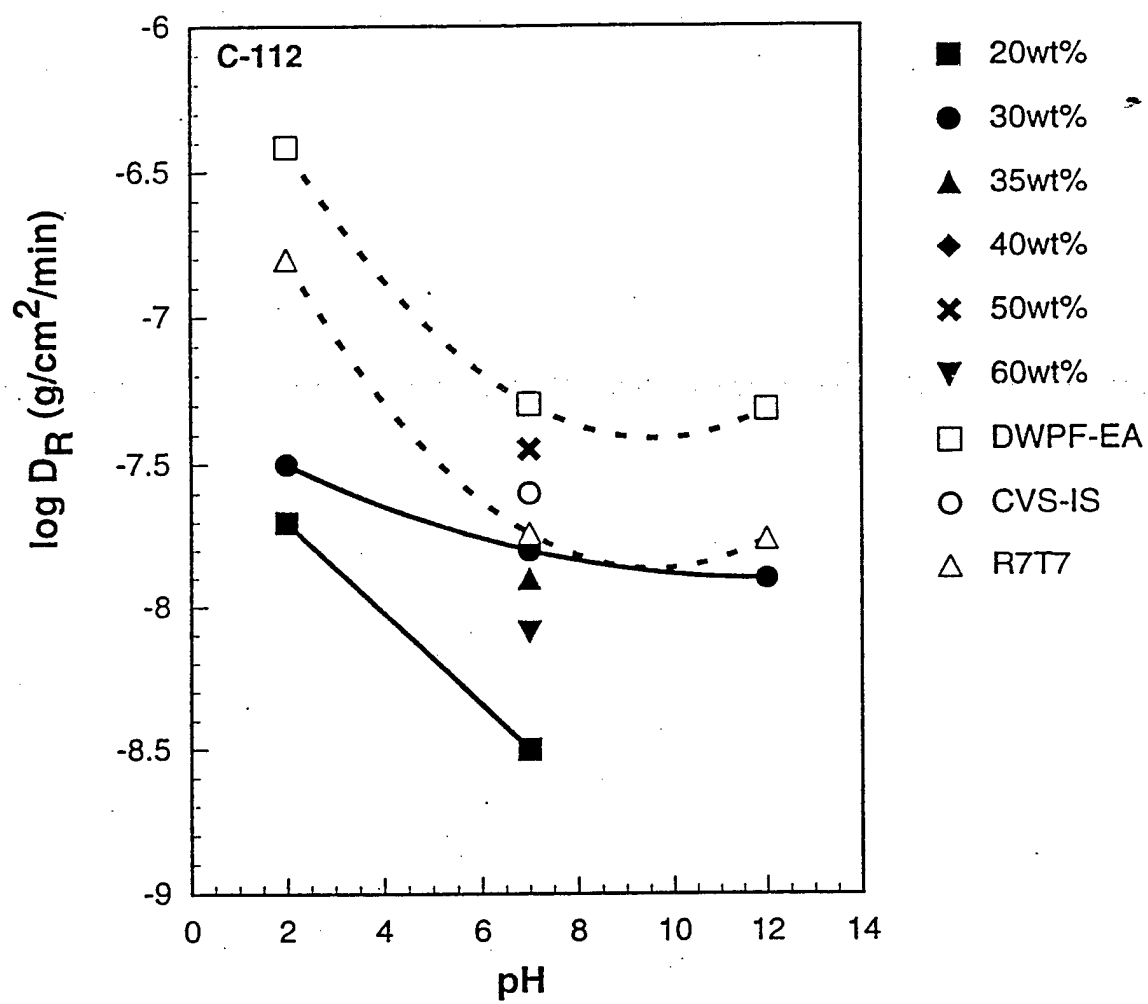


Figure 12: $\log D_R$ ($\text{g}/\text{cm}^2/\text{min}$) of iron phosphate wasteform containing C-112 sludge (solid line, solid symbols) compared to DWPF-EA (SRL), CVS-IS (PNNL), and R7T7 (France) borosilicate glasses (dashed lines, open symbols). D_R measured in solutions of HCl, distilled water, and NH_4OH for 16 days at 90°C.

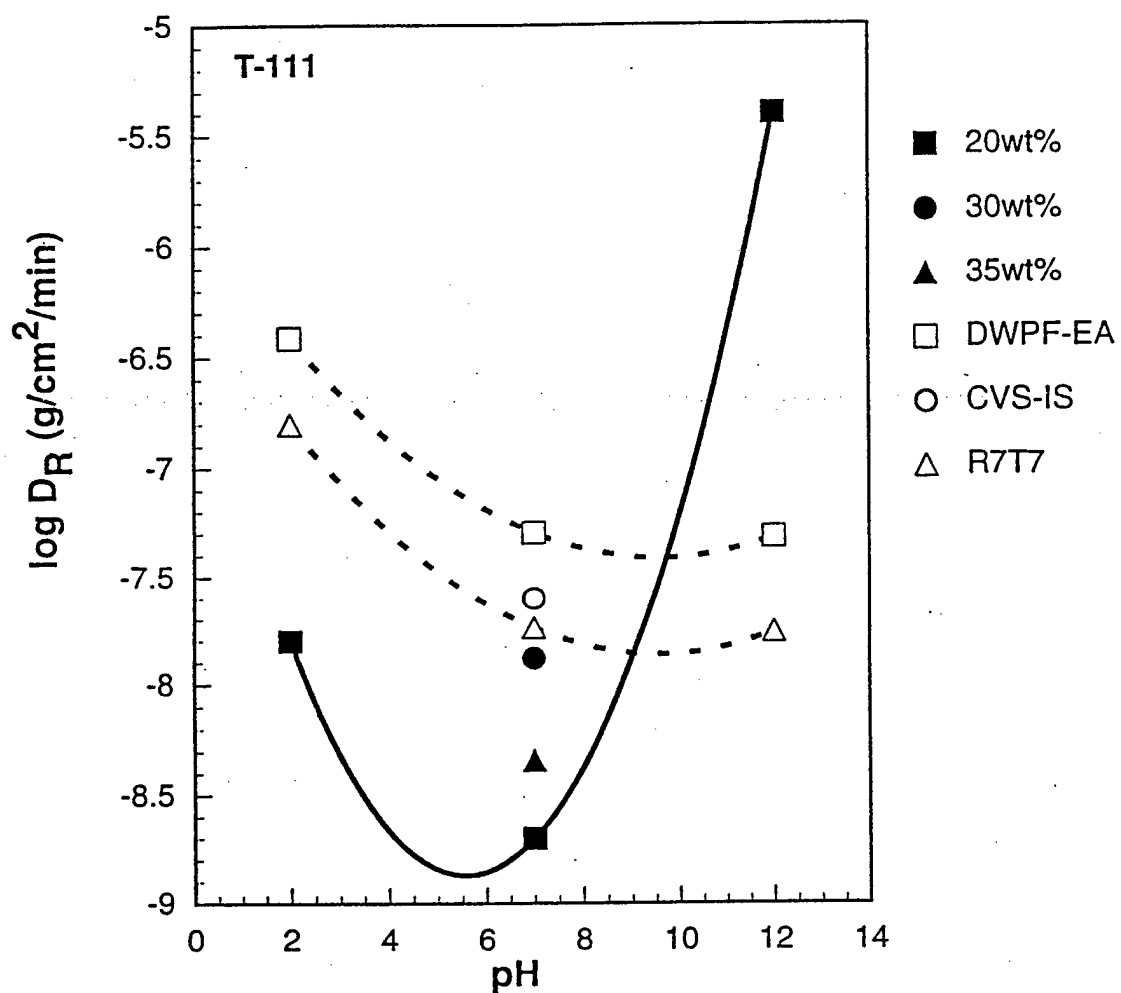


Figure 13: $\log D_R$ ($\text{g}/\text{cm}^2/\text{min}$) of iron phosphate wasteform containing T-111 sludge (solid line, solid symbols) compared to DWPF-EA (SRL), CVS-IS (PNNL), and R7T7 (France) borosilicate glasses (dashed lines, open symbols). D_R measured in solutions of HCl, distilled water, and NH_4OH for 16 days at 90°C.

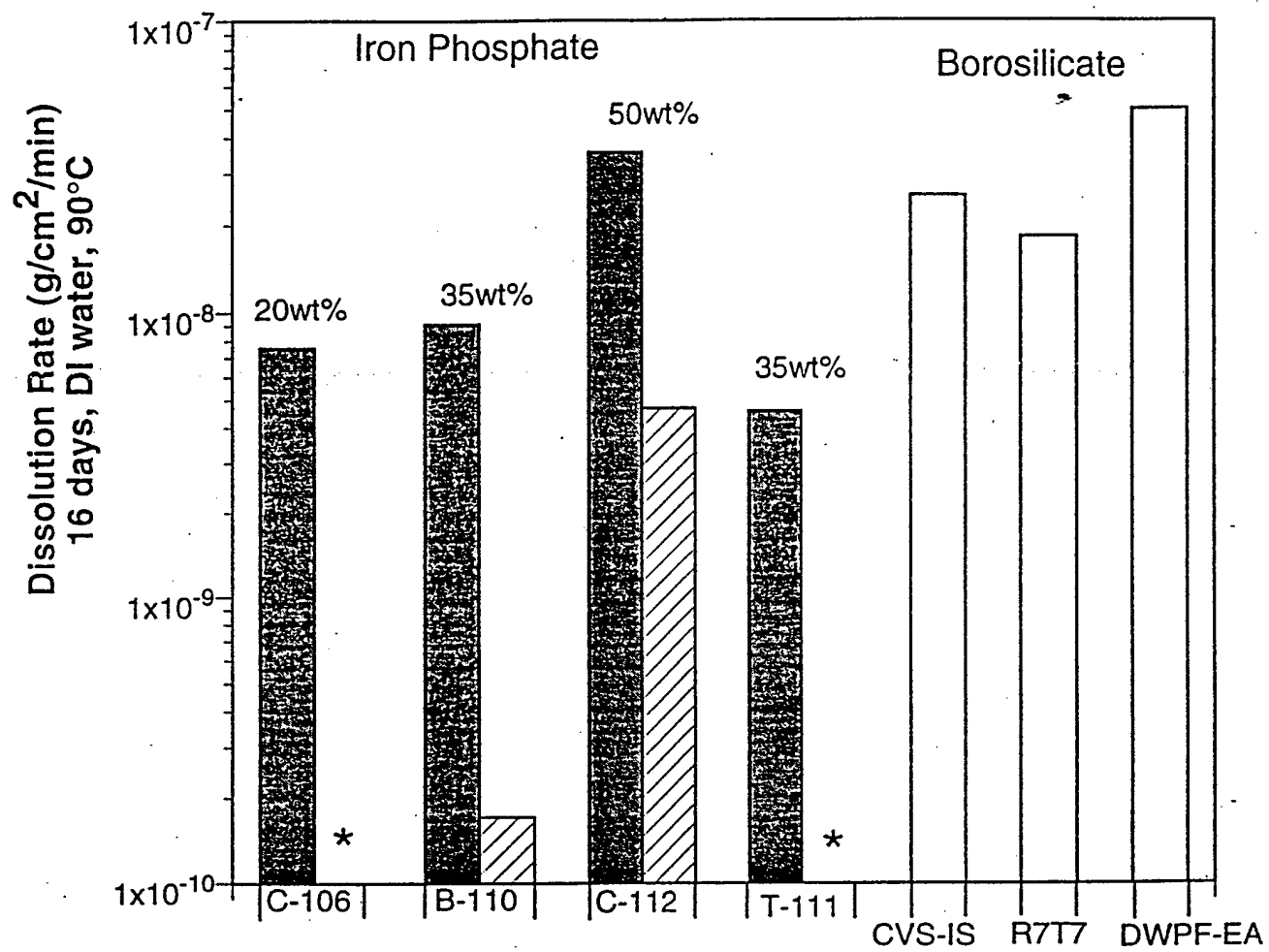


Figure 14: Dissolution Rate of glassy (solid bars) and crystallized (hashed bars) iron phosphate wasteforms and selected borosilicate glasses given for comparison. The asterisks denote wasteforms that gained a small (up to 0.36%) amount of weight after immersion. The numbers at the top of the solid bars denote the weight percent sludge in the wasteform.

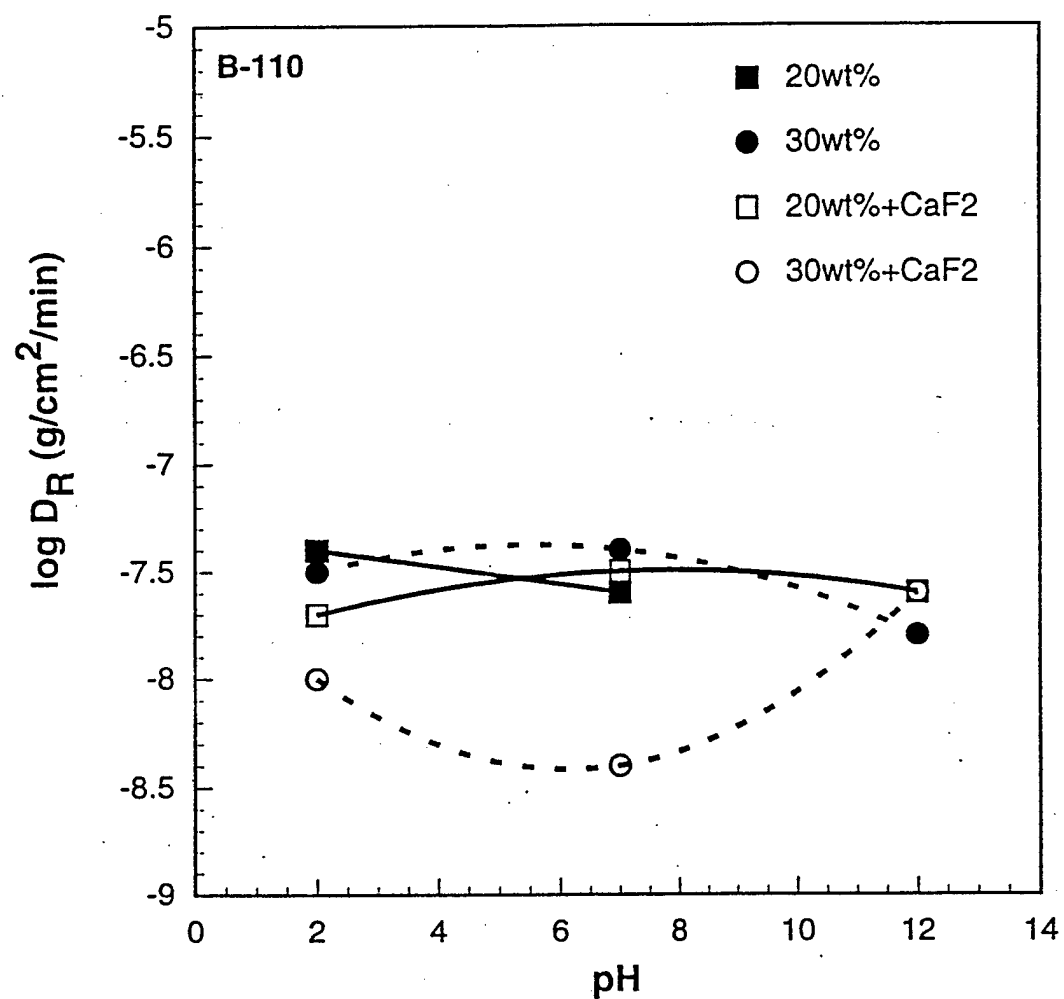


Figure 15: $\log D_R$ of iron phosphate wasteform containing 20 and 30 wt% B-110 sludge (solid lines) and glasses melted containing 7 wt% CaF₂ (dashed lines).

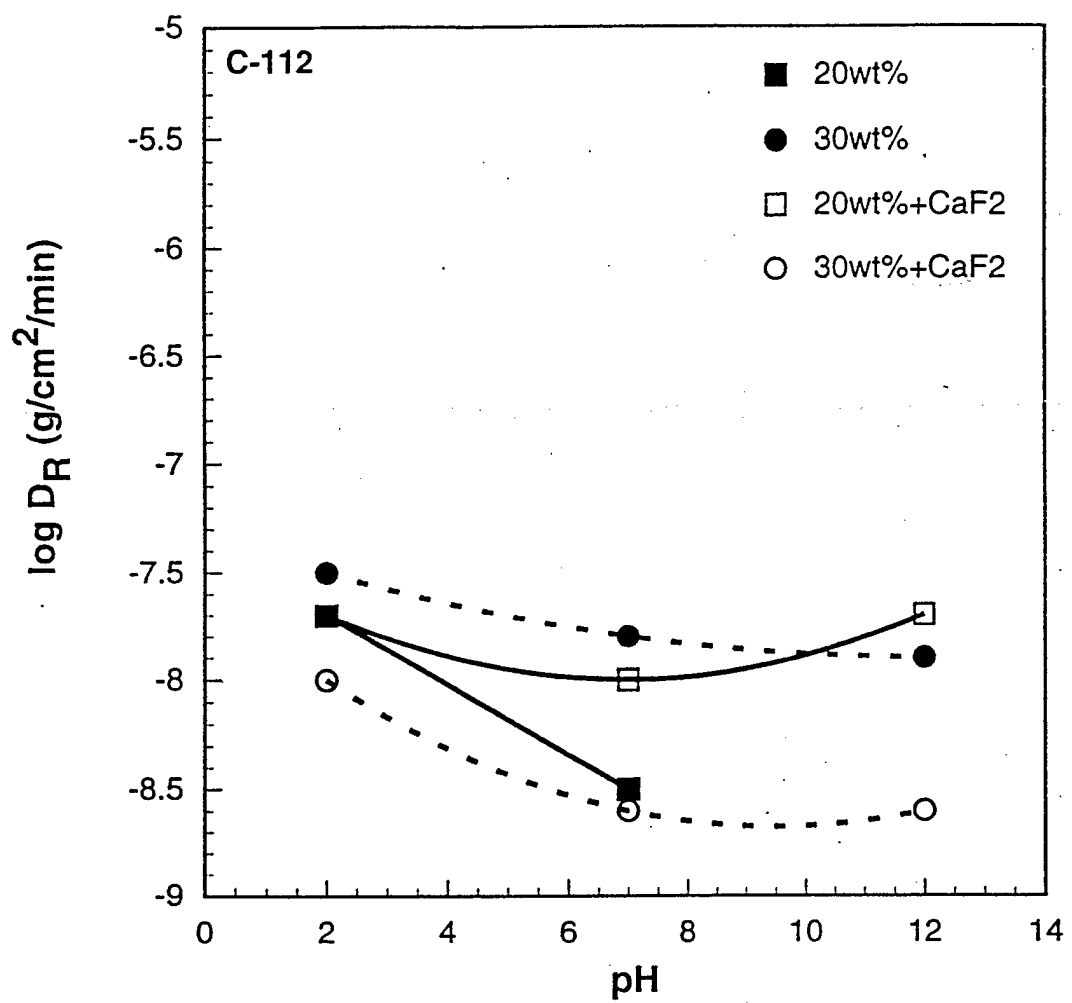


Figure 16: $\log D_R$ of iron phosphate wasteform containing 20 and 30 wt% C-112 sludge (solid lines) and glasses melted containing 7 wt% CaF_2 (dashed lines).

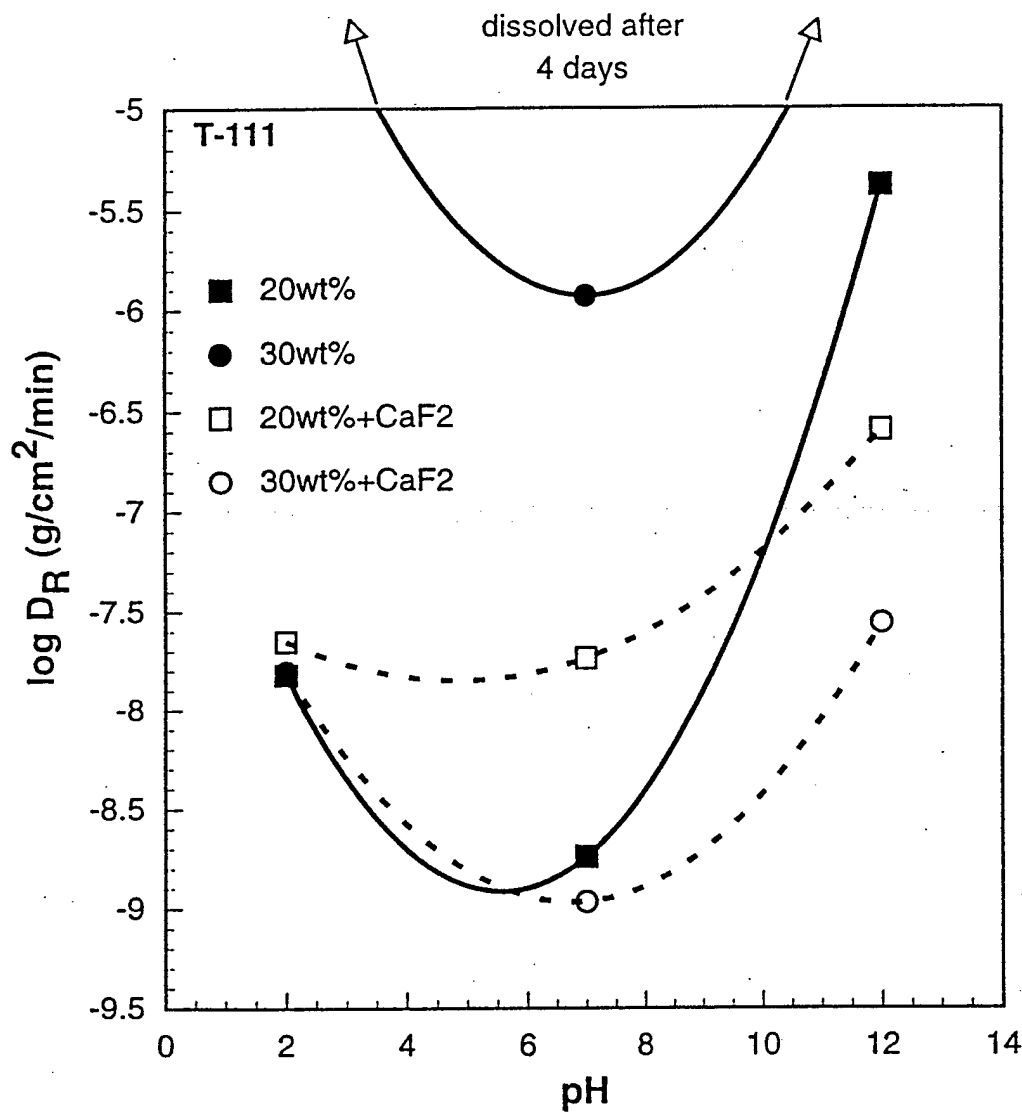
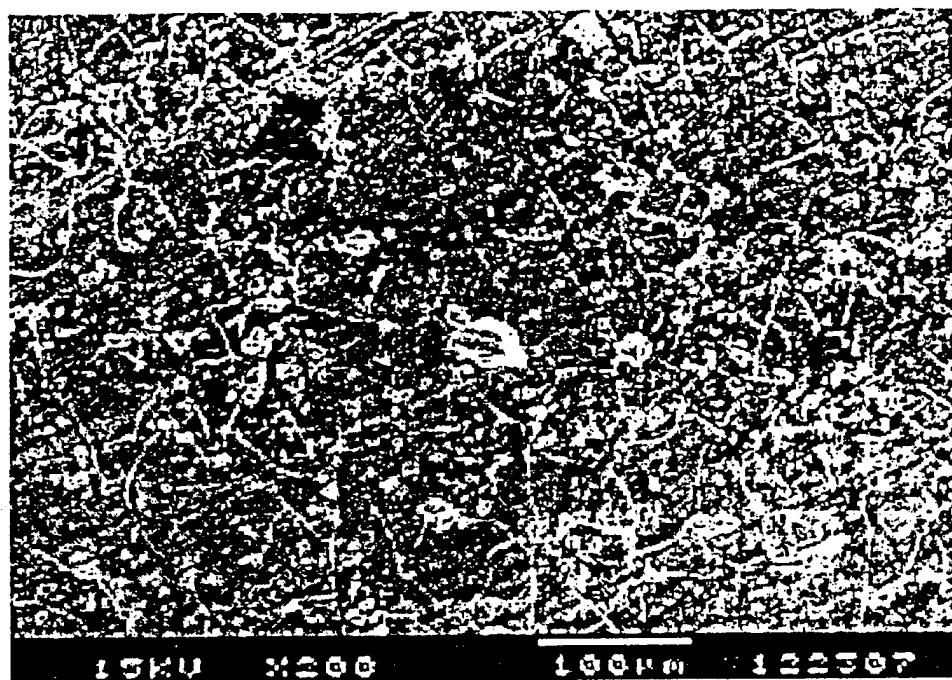
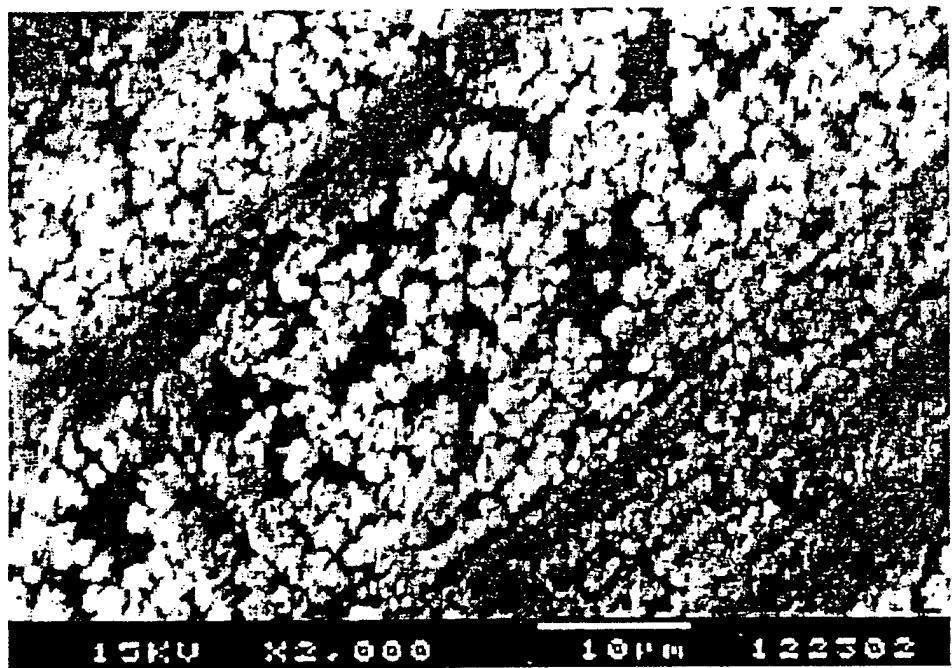


Figure 17: $\log D_R$ of iron phosphate wasteform containing 20 and 30 wt% T-111 sludge (solid lines) and glasses melted containing 7 wt% CaF_2 (dashed lines).



(a)



(b)

Figure 18: SEM micrographs of exterior surface of sludge containing wasteforms exposed to distilled water for 16 days at 90°C. (a) shows a cracked surface layer on the surface of the wasteform containing 35 wt% T-111 sludge and (b) shows particles deposited on the surface of the wasteform containing 50 wt% C-112 sludge.

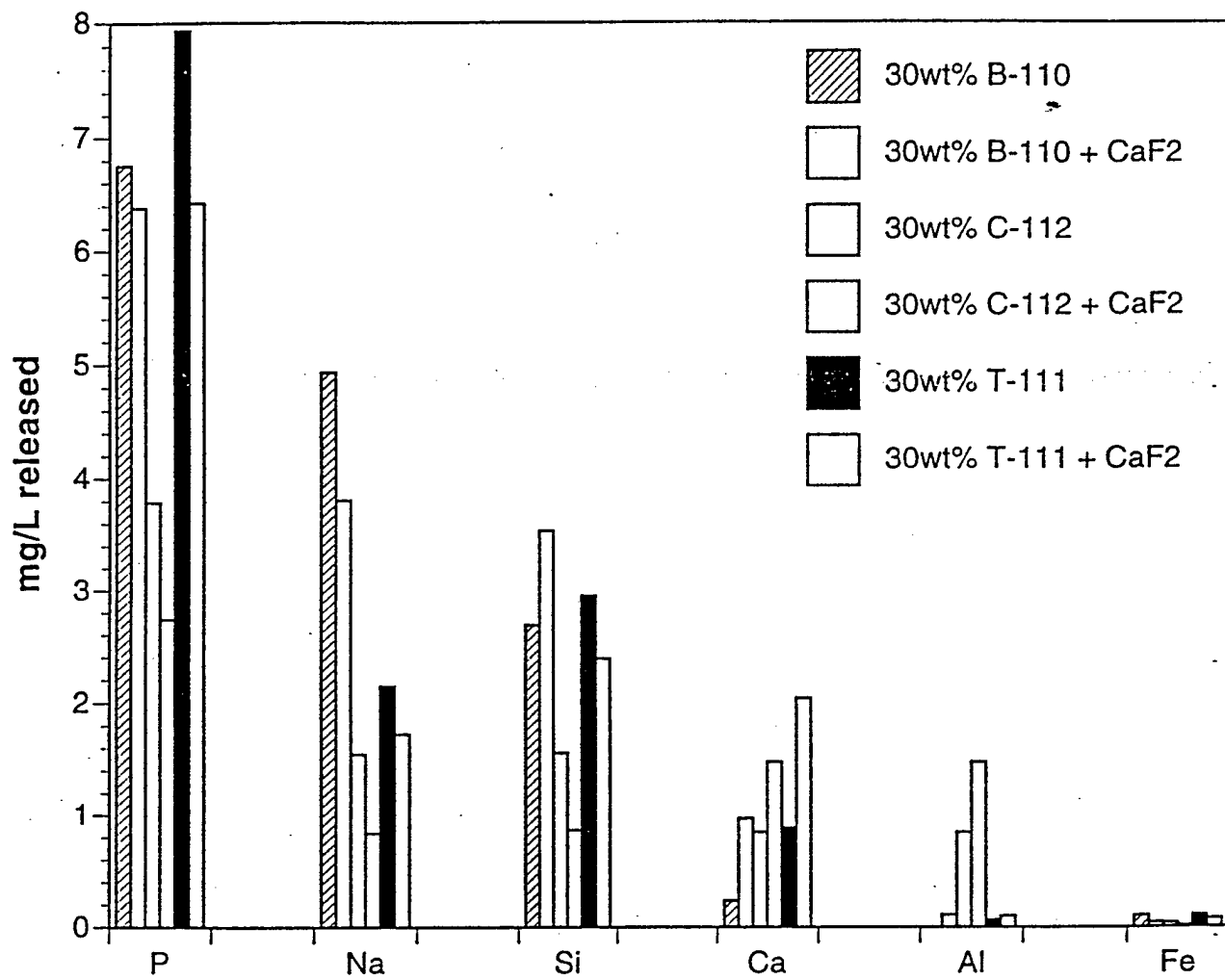


Figure 19: ICP-ES analysis of leachate solution after PCT testing of the sludge containing iron phosphate wasteforms with and without CaF_2 (open bars).

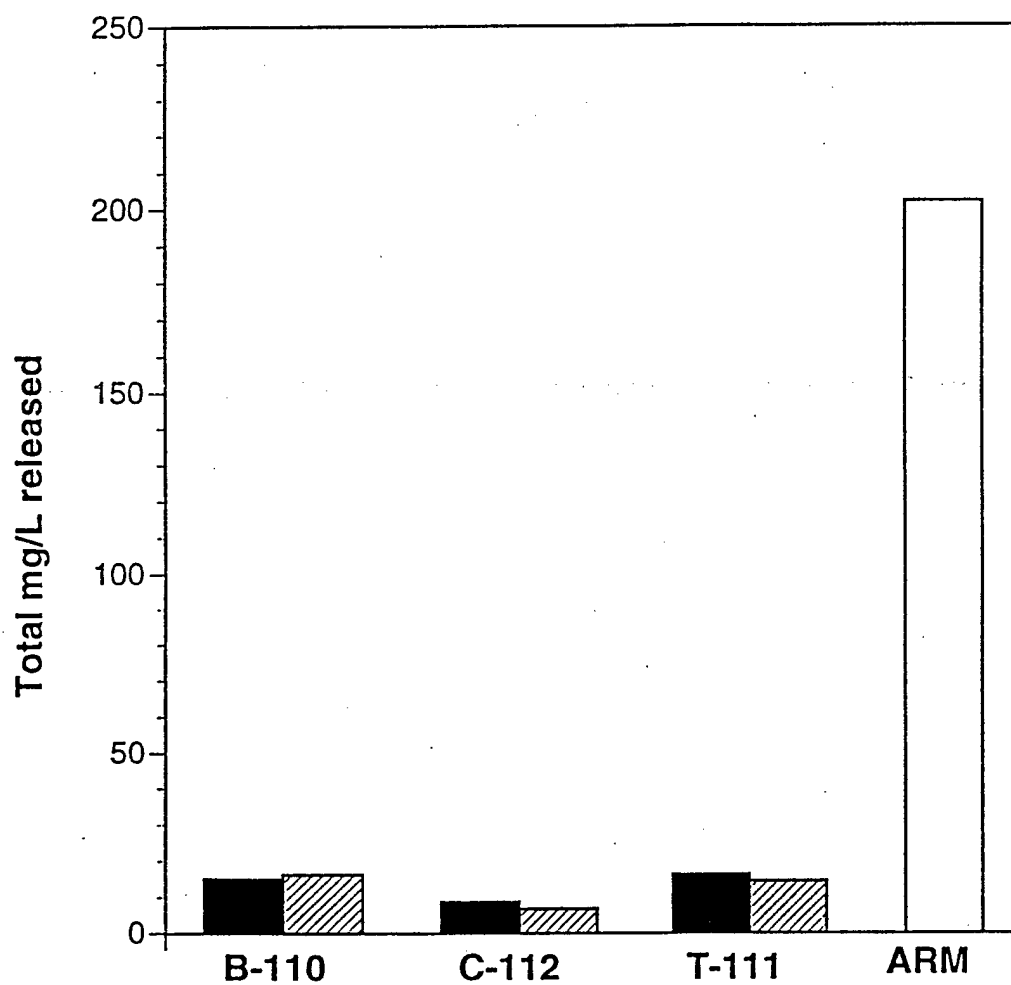


Figure 20: Total amount of material found in distilled water after PCT test of iron phosphate glass wasteform made with 30 wt% sludge (solid bars) and those with an additional 7 wt% CaF₂ (hatched bars). The ARM reference glass is shown for comparison (dotted bar).

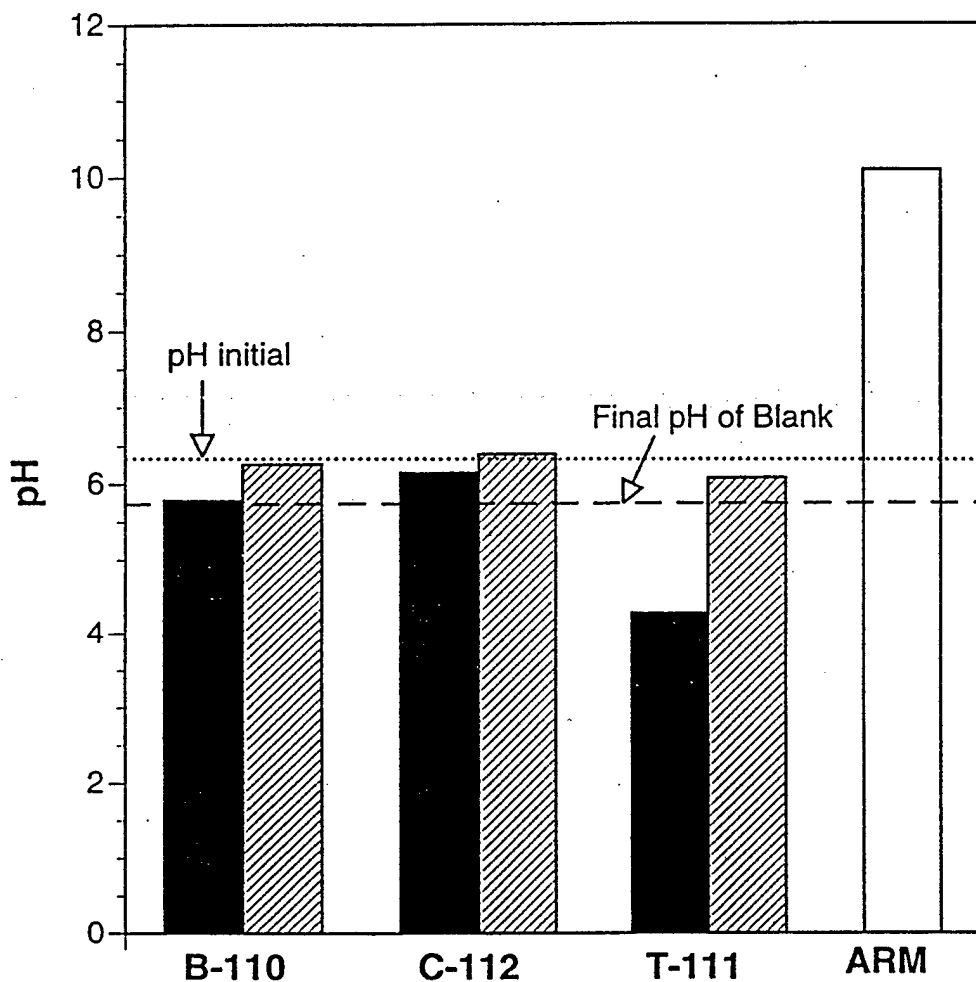
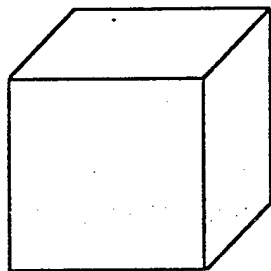
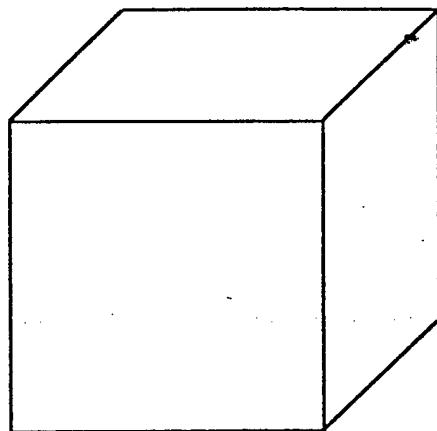


Figure 21: Final pH of solutions after PCT testing (at 90°C in distilled water for 7 days) of glasses made with 30 wt% sludge (solid bars) and those containing an additional 7 wt% CaF_2 (hatched bars). The ARM reference glass is shown for comparison (dotted bar). The initial pH and final pH of a blank is also given for reference.

Iron Phosphate Glass



Borosilicate Glass



Volume:

0.5 m^3

2.0 m^3

Total Weight:

1.67 tons

5.65 tons

Waste Loading:

60wt%

17.7wt%

Other Material

700 kg

4600kg

Required to

Produce the

($\text{Fe}_2\text{O}_3, \text{P}_2\text{O}_5$)

($\text{SiO}_2, \text{B}_2\text{O}_3, \text{Na}_2\text{O}$,

Wasteform:

$\text{Al}_2\text{O}_3, \text{CaO}, \text{Li}_2\text{O}$,

Fe_2O_3 , and others)

Figure 22: Comparison of the wasteform volume and mass for vitrifying one ton of solid C-112 waste. The borosilicate wasteform is assumed to have a maximum P_2O_5 content of 2.5 wt% and a density of 2.75 g/cm^3 .

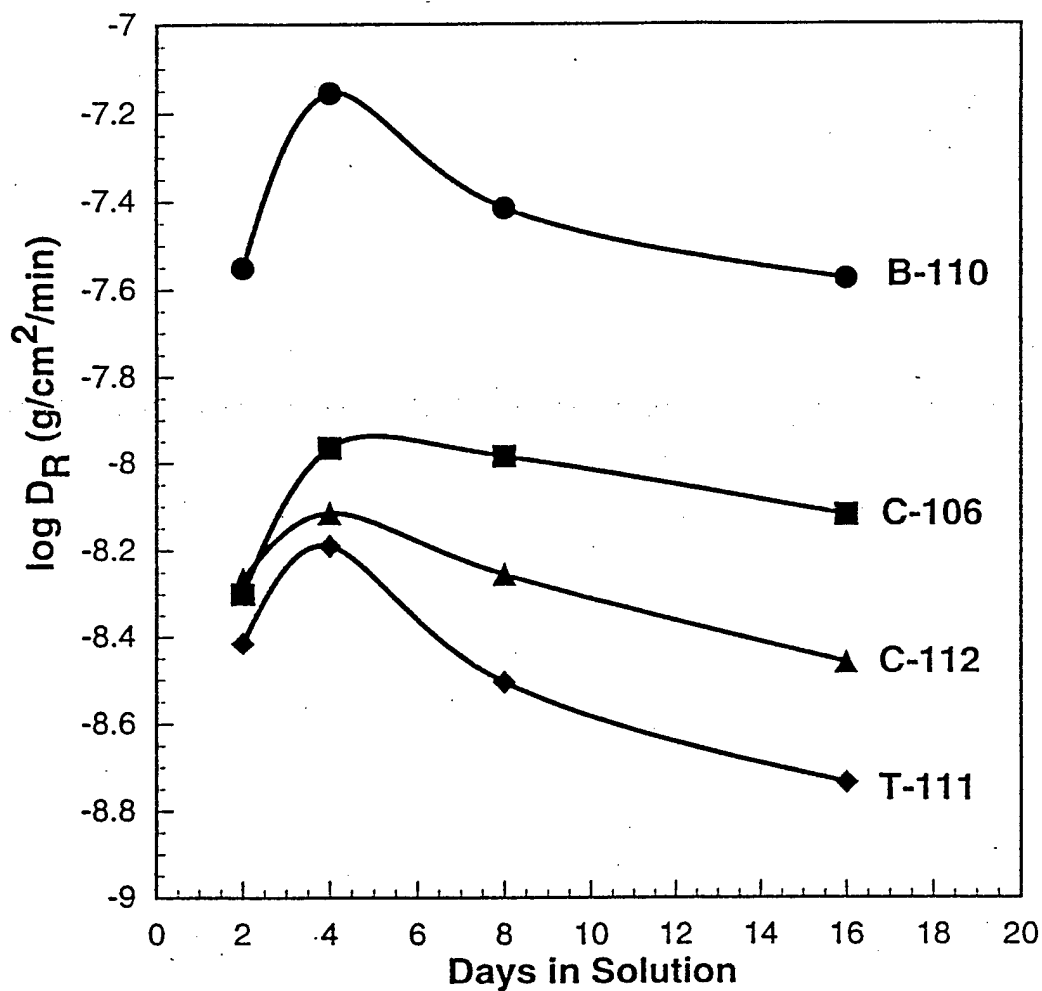


Figure 23: $\log D_R$ ($\text{g}/\text{cm}^2/\text{min}$) of iron phosphate wasteform containing 20 wt% of the C-106, B-110, C-112, or T-111 sludge. D_R measured in distilled water for up to 16 days at 90°C.

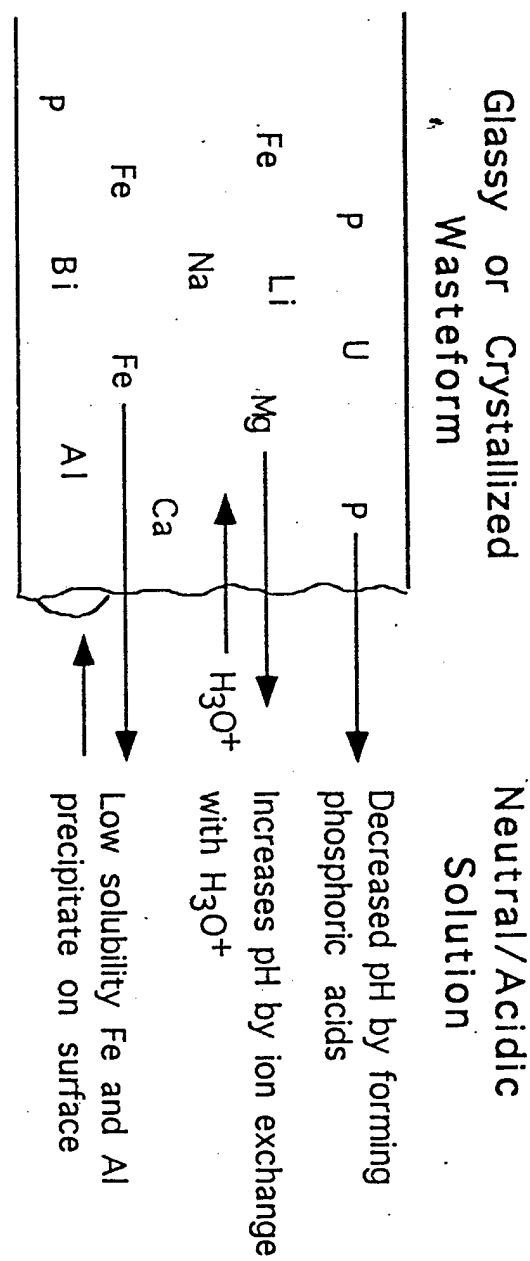


Figure 24: Schematic of corrosion of iron phosphate glassy wasteforms in neutral and acidic solutions.

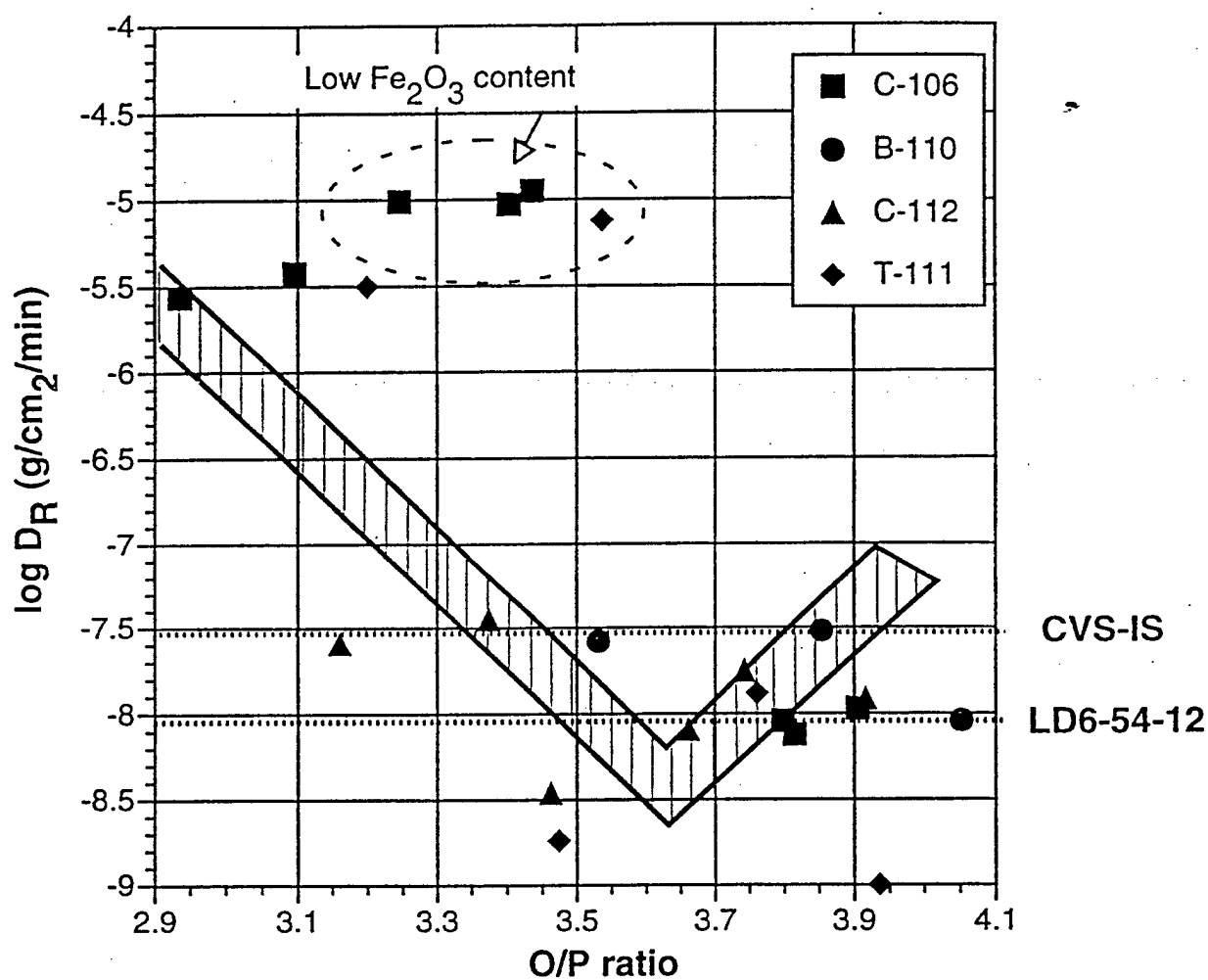


Figure 25: $\log D_R$ of sludge containing iron phosphate wasteforms measured in distilled water at 90°C. Hashed region is taken from reference 11. Dotted lines indicate the dissolution rate of the CVS-IS and LD6-54-12 glasses.